Motions in the Oceans: Potential and Kinetic Energy and Turbulent Dissipation

by

Conrad Luecke

A dissertation submitted in partial fulfillment
of the requirements for the degree of
Doctor of Philosophy
(Earth and Environmental Sciences)
in The University of Michigan
2018

Doctoral Committee:

Associate Professor Brian Arbic, Chair
Associate Professor Jeremy Bassis
Professor John Boyd
Professor Chris Poulsen
Research Scientist James Richman, Florida State University

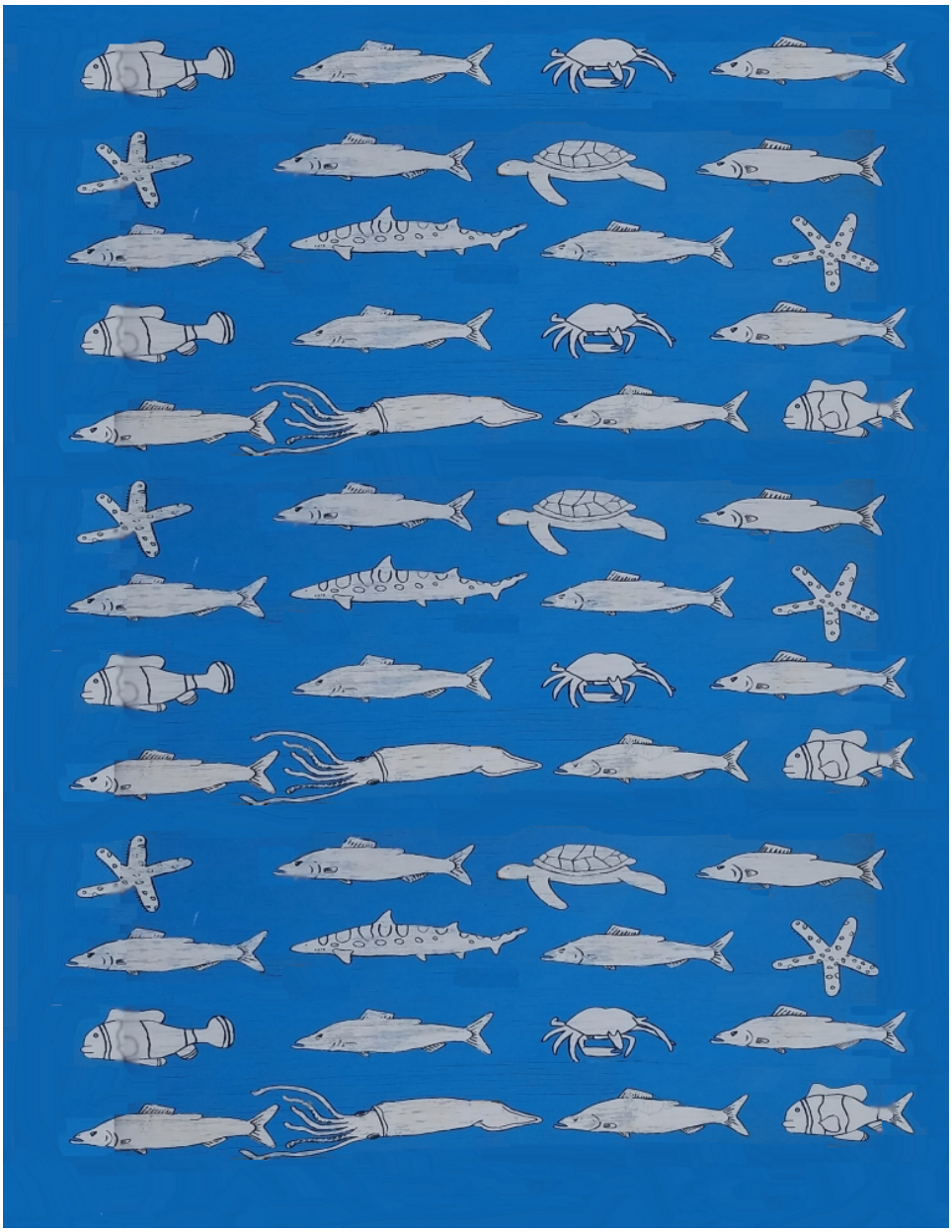

Conrad A. Luecke

cluecke@umich.edu

ORCID ID 0000-0001-6706-0188

To all the people who have inspired me to study the ocean

ACKNOWLEDGEMENTS

There are many people that have helped and supported me immensely on this journey, far too many to list here. However I would like to thank Brian Arbic, for his mentor-ship and guidance on my path to becoming an oceanographer. Many thanks to my thesis committee for their help throughout the PhD process. I thank the numerous coauthors that I have worked with in developing this thesis: Joseph Ansong, Matthew Alford, Steve Bassette, Maarten Buijsman, Jennifer MacKinnon, Dimitris Menemenlis, Jonathan Nash, Jim Richman, Robert Scott, Jay Shriver, Ole Martin Smedstad, David Trossman, Gunnar Voet, Alan Wallcraft, and Luis Zamudio. I also thank Matthew Alford and the entire Scripps Institution of Oceanography crew for their mentorship in my time there as a visiting scholar. A big shout out to Mika Siegelman and Kristin Fitzmorris for being great friends, sounding boards and colleagues. Thanks to all of the lab group members who have been in the University of Michigan Ocean Modeling Lab during my time there. Thanks to all of my friends, from all the different times in my life for their support throughout the years. Lastly I would like to thank my parents Greg and Jennifer, sister Mirelle, and grandparents Beverly and Richard for the insane amount of support and love that they have given me.

I would also like to acknowledge funding through which this work was made possible. The Office of Naval Research (ONR) grants N00014-15-1-2288 and N00014-11-1-0487, N00014-17-1-2958, and by the University of Michigan Associate Professor

Support Fund supported by the Margaret and Herman Sokol Faculty Awards.

TABLE OF CONTENTS

LIST OF FIGURES

Figure

LIST OF TABLES

Table

ABSTRACT

Kinetic energy (KE) and available potential energy (APE) in the ocean are fundamental to processes such as mesoscale eddies, tides, internal gravity waves, dissipation, and the mixing fields that drive circulation in the ocean. This dissertation examines three different sub-topics in the general realm of oceanic energetics. We examine the KE and APE in state-of-the-art global numerical ocean models and in observations, across a wide range of time scales. Lastly, we use a novel dataset to quantify the temporal, geographical, and spatial variations of turbulent dissipation.

Global maps of the mesoscale eddy available potential Energy (EAPE) field are made from a high-resolution 1/12.5 degree global ocean model. Maps made from both a free-running simulation and a data-assimilative reanalysis of the HYbrid Coordinate Ocean Model (HYCOM) are compared with maps made using Argo profiles. All maps display similar features, especially in the dominance of western boundary currents. The reanalysis maps match the Argo maps more closely, demonstrating the importance of data assimilation. Global averages of the simulation, reanalysis, and Argo EAPE all agree to within about 10 percent. The model and Argo EAPE fields are compared with EAPE computed from a dataset of "Moored Historical Observations" (MHO) in conjunction with a global climatology. At MHO locations, 15-32 percent of the EAPE in the Argo estimates is due to aliased motions having periods of 10 days or less. Spatial-averages of EAPE in HYCOM, Argo, and MHO data,

agree to within 50 percent at MHO locations, with both model estimates lying within error bars of observations. Analysis of the EAPE field in an idealized model suggests that much of the scatter seen in comparisons of different EAPE estimates is expected given the chaotic nature of mesoscale eddies.

Temperature variance and KE from two simulations of HYCOM (1/12, 1/25 degree) and three simulations of the Massachusetts Institute of Technology general circulation model (MITgcm; 1/12, 1/24, and 1/48 degree) are compared with the MHO dataset. The variances are computed across frequencies ranging from the supertidal to the subtidal. Improvement of temperature variance and KE with resolution varies greatly between the models, and within each frequency band. Results suggest that model resolution is most important for the supertidal band. HYCOM generally is more correlated with the MHO, and handles supertidal, semidiurnal, and diurnal velocities in a number of specific near-shelf high-velocity locations better than MITgcm does, possibly due to wave-drag. Additionally, we compare both HYCOM 1/25 degree and MITgcm 1/48 degree geostrophic eddy kinetic energy (EKE) with EKE computed from AVISO, and find that in bulk, both models compare well.

Estimates of the turbulent kinetic energy dissipation rate are made from analysis of thermistor chains at five moored locations near Palau. Moorings are located near steep topographical features, and in the far field. Long durations, fast sampling intervals, high vertical resolution, and the horizontal spread of the five moorings provide both a spatial and temporal picture of turbulent processes. Signals in turbulent dissipation have strong associations with a wide range of dynamic processes, such as mesoscale eddies, submesoscale fronts, near-inertial oscillations, spring-neap cycles, and tidal motions. We find the time-mean turbulent kinetic energy dissipation rate to decay from $10^{-7}(W/kg)$ close to topography, to $10^{-10}(W/kg)$ at a distance of about 35 km. Time-mean vertical profiles show bottom-enhanced dissipation, and elevated dissipation in the upper water-column.

CHAPTER I

Introduction

1.1 Reservoirs of Energy in the Ocean

The Earth's ocean is an active thermodynamic system that stores and releases a vast amount of energy. The energy that drives the dynamics of our ocean comes primarily from the Sun, winds, and tides. Fundamentally, this energy determines the movement of water, and the transfer of heat between Earth's equatorial and polar regions. The poleward transport of heat in the ocean is crucially important to the climate, and the exchange of energy between the ocean and atmosphere moderates and influences global weather patterns. The mixing of water masses within the ocean controls the large-scale overturning circulation. Ocean currents not only distribute heat, they also play a crucial role in the global ecosystem by storing and releasing carbon dioxide, as well as recycling nutrients critical to marine biology.

The work presented here focuses on energy reservoirs and energy dissipation, in both models and observations. Reservoirs of dynamic energy content in the ocean fall into two forms: Kinetic energy (KE), the result of water motions, and available potential energy (APE), stored as displacements of density interfaces. APE is defined as the amount of potential energy in a stratified fluid that is available for mixing and conversion into kinetic energy. The understanding of KE and APE reservoirs in the ocean is key to the understanding ocean mixing and the physics that drive circulation

in the ocean. Processes that influence APE and KE in the ocean exists across a broad spectrum of time and length scales, and in the form of a wide range of features, from global circulation patterns varying over centuries to turbulent dissipation on scales of minutes. Of interest to this study are mesoscale eddies, tides, and internal gravity waves, and their effects on turbulent dissipation.

Low-frequency energy in the ocean is dominated by mesoscale eddies (*Kuragano and Kamachi*, 2000; *Jacobs et al.*, 2001; *Chelton et al.*, 2007). These eddies have time scales on the order of 30-200 days, and have length scales on the order of 50-200 km. Mesoscale eddies are primarily geostrophic in balance, meaning that in steady state, they are the result of a balance between pressure gradients and the Coriolis force. Mesoscale eddy flows over topographic features can result in the generation of internal lee waves (*Trossman et al.*, 2016).

At higher frequencies than the mesoscale, submesoscale flows emerge as a pattern of fronts with horizontal scales between 10 kilometers and 100 meters (*Hecht and Hasumi*, 2008), that separate waters of different salinities and temperatures. Submesoscale fronts have increasingly come into focus as a key component of the dynamics of mixing in the ocean. Within Chapter IV, variance that falls into the frequency range likely to contain submesoscale motions is referred to as subtidal.

At high frequencies, ocean energetics are dominated by internal gravity waves (IGWs). An IGW is a wave propagating within the layers of a stratified fluid, restored by the force of gravity. The maximum vertical perturbations of density in IGWs occur within the interior of the ocean, well below the ocean surface.

IGWs with frequencies near the Coriolis frequency are called near-inertial waves. Near-inertial waves are primarily forced by fluctuations in surface winds (*D'Asaro*, 1984; *Simmons and Alford*, 2012). Near-inertial waves appear to be a major source of wave breaking and mixing in the ocean interior (*Ferrari and Wunsch*, 2009).

IGWs with tidal frequencies are known as internal, or baroclinic tides, and they

are generated by large-scale barotropic tidal flow over topographic features (*Bell*, 1975). As with barotropic tides, baroclinic tides can be either semidiurnal (twice per day), or diurnal (once per day).

At frequencies greater than that of the tides, there is a continuum of IGW energy, separate from the near-inertial and tidal peaks. This IGW continuum is described by the classical Garrett-Munk spectrum (*Garrett and Munk*, 1975). Nonlinear wave-wave interactions between the near-inertial and tidal frequencies are thought to fill out the oceanic IGW continuum (*Müller et al.*, 2015).

As IGWs break in the interior of the ocean, they facilitate the dipycnal mixing of water across stratified layers and contribute to the turbulent dissipation of energy within the ocean (*Munk and Wunsch*, 1998). The mixing due to these breaking IGWs plays a fundamental role in the oceanic meridional overturning circulation, as they mix the dense waters at the ocean bottom with the lighter waters above. Furthermore, levels of energy within the APE and KE reservoirs are set in part by the energy dissipation, which also serves to exchange energy between many physical processes. Thus, mixing due to the breaking of internal waves is directly related to turbulent dissipation and the small-scale redistribution of energy in the ocean.

1.2 Use and Validation of General Circulation Models to Study Processes in the Ocean

Physical observations provide an essential tool for studying processes in the ocean. However, due to the wide spatial and temporal scales of processes discussed above, obtaining such observations presents challenges. In-situ moored instrumentation including moored current meters and thermistors (e.g., *Richman et al.*, 1977; *Schmitz*, 1988) can provide records with long time series. However, these types of measurements suffer from spatial limitations; they only take measurements at a limited number of

geographical locations. Ship-based measurements such as conductivity, temperature and depth (CTD) profiles, and velocity profiles from Acoustic Doppler current profilers (ADCPs) offer high vertical resolution, but with limited temporal or spatial coverage. Autonomous profiling devices, such as Argo floats (*Roemmich and Owens*, 2000), have vastly increased the spatial coverage of global in-situ data, but the relativity coarse spacing between individual float profiles ($\sim$ 3 degrees) and slow repeat time ($\sim$ 10 days) present issues in the study of both small scale and high-frequency dynamic processes in the ocean, including the IGW continuum. Satellite altimetry, which provides near-global coverage of sea surface height (e.g., *Chelton et al.*, 2007), suffers from poor temporal resolution, with repeat times of 10 days or longer, in addition to providing access only to surface fields with no information from the subsurface ocean. Both satellite altimetry and Argo suffer from the potential for aliasing of high-frequency motions into their signals due to their relatively slow sampling rates.

Output from numerical models, known as ocean general circulation models (OGCMs), have been used to study energetic processes in the ocean. In recent years, OGCMs have been run at higher spatial and temporal resolutions. Increases in computer power have led to high-resolution, three-dimensional OGCMs that are able to simulate mesoscale eddies on a global scale (e.g., *Hecht and Hasumi*, 2008; *Chassignet et al.*, 2009). Furthermore, some OGCMs such as The HYbrid Coordinate Ocean Model (HYCOM) and Massachusetts Institute of Technology general circulation model (MITgcm) now include both astronomical tidal forcing in addition to realistic atmospheric forcing (*Arbic et al.*, 2018). High-frequency atmospheric forcing results in the generation of near-inertial waves (*Silverthorne and Toole*, 2009; *Simmons and Alford*, 2012), and barotropic tidal flow over topographic features creates internal tides (e.g., *Garrett and Kunze*, 2007). As the models increase in horizontal and vertical resolution, nonlinear wave-wave interactions fill out the oceanic IGW spectrum (*Müller et al.*, 2015; *Savage et al.*, 2017a,b; *Rocha et al.*, 2016a,b).

OGCMs offer their own unique set of strengths and weaknesses. For instance, unlike observational data, high-frequency model output is available on a fine spatial grid at any location, both at the surface and within the interior of the ocean. While models can cover a wide range of space and time scales, their inclusions of key physical processes such as damping and mixing is often poor. The question arises; How can high-resolution OGCMs be validated to aid in the study of the above dynamic processes? Resolving a spectrum of internal waves represents a new paradigm for OGCMs. Because internal waves contribute to mixing and the redistribution of large amounts of energy over long distances, comparing the modeled internal wave spectrum with observations is essential for our understanding and simulation of the three-dimensional patterns of mixing. This is in turn important for accurate modeling of large-scale ocean dynamics (*Munk and Wunsch*, 1998).

Improving the realism of OGCMs is becoming increasing important as high-resolution ocean models have increasingly been employed for predictive work. HYCOM is used as an operational model by the US Navy. Search and rescue efforts in recent years have employed models to predict the drift of vessels and individuals lost at sea. Models including HYCOM have even been used to aid in the effort of understanding the spread of contaminants such as the 2010 Deepwater Horizon oil spill.

In order for OGCM output to be useful for the study of the physical energetic processes mentioned in this chapter, models must be carefully compared to observations. Furthermore, the mechanisms relating to energy dissipation and damping need to be better understood in order to eventually implement more accurate parameterized energy dissipation and damping in OGCMs. With these factors mind, in this work we compare the energy levels (PE and KE) in two different OGCMs to observations, and we also use in-situ data to examine a wide range of dissipation processes.

1.3 Overview

In Chapter II, we develop a methodology to estimate low-frequency eddy APE (EAPE) from temperature anomaly time series at 1,057 individual moored historical instrument observations. These estimates are then compared with estimates of EAPE made from OGCM model output from HYCOM at the same locations. Model output from both a free running simulation and a data assimilative run are used to test the effect of data assimilation on model output. Additionally, Chapter II compares these EAPE estimates to estimates made from Argo floats both at the locations of the moored historic estimates, and globally. Lastly, we show that there is considerable scatter whenever averages of the EAPE estimates are compared against each other. A brief analysis of the EAPE fields in a horizontally homogeneous quasi-geostrophic (QG) turbulence model illustrate that scatter is inherent in EAPE comparisons made from a turbulent and chaotic mesoscale eddy field. We use established theory (*Flierl and McWilliams*, 1977) in conjunction with the analysis of an idealized model to quantify the expected scatter in comparisons such as the one presented here.

Chapter III builds upon techniques and methodology used in Chapter II, but applies them to a larger number of models and across a wide range of frequencies. Outputs from two dynamically different models are utilized. We compare simulations from the MITgcm run at three different horizontal resolutions and from the HYCOM run at two different horizontal resolutions to moored historical observations of temperature variance and kinetic energy. By integrating over six different frequency bands (subtidal (12-2.06 cpd), semi-diurnal (2.05-1.86 cpd), diurnal (1.05-0.87 cpd), near-inertial (0.9-1.1f), subtidal (0.7-0.1 cpd), and mesoscale (0.09-0.01 cpd)), we test the ability of these simulations to model motions ranging from mesoscale eddies to the internal gravity wave continuum as discussed above. As in Chapter II, this study is quasi-global, in that 3,096 instrumental records of temperature and 3,133 instrumental records of velocity, distributed over the major ocean basins, are used.

Lastly, we compare geostrophic eddy kinetic energy from both MITgcm and HYCOM to values computed from the AVISO satellite altimeter database in order to obtain a global view of model-data agreement.

Chapter IV focuses on an inertial-convective subrange scaling estimate of turbulence dissipation made from in-situ moored thermistor chains. The mooring data presented in Chapter IV represents an unprecedented and unique dataset, with both spatial and temporal coverage of Turbulent KE (TKE) dissipation. As part of the FLEAT (FLow Encountering Abrupt Topography) project, five moorings containing thermistor chains were deployed allowing both a spatial and temporal view of mixing around the island of Palau. This study aims at better understanding the mixing response of flows as they interact with the steep topography in the region north of Palau. Through a qualitative assessment of the depth-time series of the TKE dissipation rate ϵ, we highlight multiple physical processes that impact the temporal modulation of turbulent dissipation. TKE dissipation plays a key role in the energy dissipation and damping that must be parameterized well in order to make OGCMs more physically accurate. Further work based upon the research presented here will be addressed in Chapter V.

CHAPTER II

The Global Mesoscale Eddy Available Potential Energy Field in Models and Observations

2.1 Introduction

Low-frequency flow in the ocean is dominated by mesoscale eddies. These eddies have time scales on the order of 30-200 days, have length scales on the order of 50-200 km, and have been studied through many observational platforms including moored current meters and thermistors (e.g., *Richman et al.*, 1977; *Schmitz*, 1988), satellite altimetry (e.g., *Chelton et al.*, 2007), and surface drifters (e.g., *Lumpkin and Pazos*, 2007). In recent years, increased computer power has led to high-resolution, three-dimensional ocean models that are able to simulate and forecast mesoscale eddies on a global scale (e.g., *Hecht and Hasumi*, 2008; *Chassignet et al.*, 2009). Because global eddying models are used for forecasting oceanic flows and for dynamical process studies, the question arises as to how accurate these models are at representing energetic phenomena in the ocean. A number of recent studies have focused on comparisons of high-resolution three-dimensional ocean models with observational data. For example, model kinetic energy in both low-frequency (*Penduff et al.*, 2006; *Scott et al.*, 2010; *Thoppil et al.*, 2011) and tidal (*Timko et al.*, 2012, 2013) bands have been compared with kinetic energy measured from moored ocean current meters and

surface drifters.

This chapter presents global maps of mesoscale Eddy Available Potential Energy (EAPE) from both a free-running simulation and a reanalysis of the HYbrid Coordinate Ocean Model (HYCOM: *Chassignet et al.*, 2009), run on a $\frac{1}{12.5}^{\circ}$ global grid. The global maps of low-frequency EAPE computed from HYCOM are compared to global EAPE maps enabled by, and recently computed from, the Argo float array (*Roullet et al.*, 2014). To our knowledge, no truly global model-data comparison of EAPE has been attempted until now.

The model-data comparison of EAPE in this work tests the ability of models to represent mesoscale eddy dynamics in the ocean interior. Available Potential Energy (APE) is defined as the amount of potential energy in a stratified fluid that is available for mixing and conversion into kinetic energy (*Munk and Wunsch*, 1998; *Huang*, 1998). Although much literature has been focused on the subject of the time-mean APE (*Winters et al.*, 1995; *Saenz et al.*, 2012; *Tailleux*, 2013), there is little in the way of validating the realism of EAPE in realistic, high-resolution ocean models. The computation of EAPE differs from the computation of time-mean APE in the works cited above in that it requires no complex reference state or background potential energy, and instead relies upon a locally calculated mean-isopycnal state. EAPE presented in this study is the result of time varying displacements of density surfaces away from a mean density surface within a stratified fluid. As these vertical displacements of density layers occur, they bring deeper (usually colder) water upwards, and shallower (usually warmer) water downwards. Because of this, motions associated with changes in APE lead to temperature variations. A schematic of this process can be seen in Figure 2.1. For the purpose of this chapter, a low-frequency "eddy" is defined as a departure from a long-term temporal mean, with a period of greater than two days. EAPE –the energy of fluctuations in density around a time-mean– is a function of both background stratification and isopycnal fluctuations, and is, there-

fore, a critical component of the structure of the pycnocline (*Gnanadesikan*, 1999). Validating the ability of HYCOM to predict EAPE lays the groundwork for further study of energetics in high-resolution ocean models.

We compare the HYCOM simulation, HYCOM reanalysis, and Argo EAPE to independent estimates computed from anomaly time series at 1,057 individual moored historical instrument observations, in conjunction with buoyancy frequencies taken from a global climatology. Hereafter, the Moored Historic Observations will be referred to as MHO. An advantage of using MHO instruments as an observational dataset for EAPE is that the relatively high temporal resolution of many MHO instruments permits us to separate the EAPE due to low-frequency mesoscale eddy motions from EAPE due to high-frequency motions such as internal gravity waves and tides. High-frequency motions are aliased into Argo records which have a ~ 10 day cycle time. Disadvantages of the MHO dataset include its sparse spatial coverage, a likely seasonal bias due to the fact that it is simpler to deploy moorings in summer than in winter, and the lack of salinity data at the majority of MHO locations. Due to the lack of salinity data, the MHO EAPE are calculated using temperature as a proxy for density, a procedure that has a long historical precedent in oceanography (*Dantzler*, 1977; *Wunsch*, 1999). The use of temperature as a proxy for density is less accurate in the upper ocean due to density compensated motions (*Rudnick and Ferrari*, 1999). For this reason, we compute EAPE only at MHO instruments that are 60m or more below the surface. We also test the differences between EAPE computed from density variations versus EAPE computed using temperature as a proxy for density, using both HYCOM output and output from modern McLane in-situ profiler instruments (*Doherty et al.*, 1999).

An additional goal of this chapter is to test whether modeled EAPE is improved with data assimilation. Recent advances in both remotely sensed and in-situ oceanic observations have dramatically increased the amount of data available for assimilation

in a reanalysis. In this chapter we will demonstrate that the data assimilation in the reanalysis improves the background buoyancy frequency, a critical constituent of the EAPE calculation. We will also show that the spatial structures of EAPE in the global HYCOM reanalysis more closely resemble the spatial structures seen in the Argo maps than do the spatial structures in the HYCOM simulation map. Finally, we employ the *Murphy* (1988) skill score to further quantify improvement in the reanalysis relative to the simulation. In the case of global EAPE, the skill score is computed between HYCOM and Argo EAPE, while at MHO locations, the skill score is computed using the square of temperature anomalies in HYCOM and MHO.

We will show that there is considerable scatter whenever averages of the estimates used here – HYCOM simulation, HYCOM reanalysis, MHO, and Argo– are compared against each other. A brief analysis of the EAPE fields in a horizontally homogeneous quasi-geostrophic (QG) turbulence model demonstrates that statistical scatter is inherent in EAPE comparisons made from a chaotic mesoscale eddy field, even without the complicating factors present in the actual ocean (laterally inhomogeneous environments, varying topography etc.). Established theory (*Flierl and McWilliams*, 1977) in conjunction with our analysis of the idealized model quantifies the expected scatter as a function of record length, which is typically on the order of several months to a year for MHO records.

2.2 Models, Observational Data, and Methods

We use a free running global HYCOM simulation run for 20 years from 1993-2012, and a data-assimilative reanalysis run over the same time period. For our global comparison with Argo, all HYCOM EAPE is computed using density anomalies. Due to the size of the 20 year model output, we chose output from one model year (2003) for our global comparisons. Our global comparisons are made at a depth of 500m, close to the depth of the EAPE maximum presented in *Roullet et al.* (2014). Model

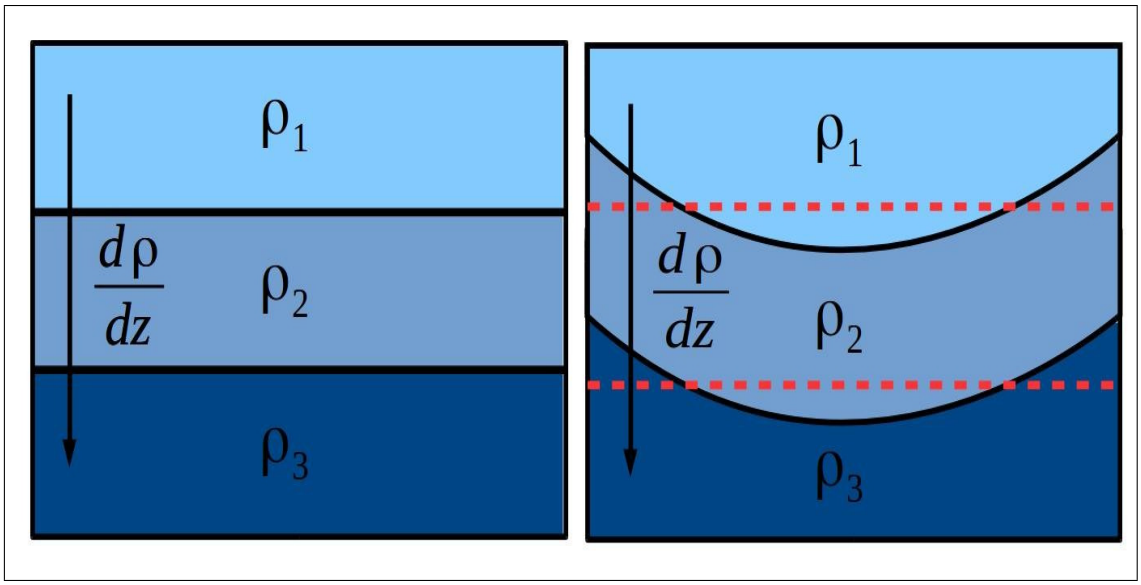

Figure 2.1: Schematic showing a simplified layered model of the ocean. ρ_1, ρ_2, and ρ_3 represent layers of increasing density. The panel on the left shows the layers in their respective lowest available potential energy state, while the panel on the right depicts the vertical displacements of the layers that result in the production of APE.

EAPE is calculated using the native $\frac{1}{12.5}^{\circ}$ resolution, and then decimated to $\frac{1}{4}^{\circ}$ degree resolution for mapping purposes. For our MHO-HYCOM comparison, we choose an EAPE computation method that is straightforward and consistent with the limitations inherent in the MHO data. Salinity data are generally not available alongside the historical temperature time series records. With this in consideration, we take temperature anomalies – low-frequency departures from a temporal mean – as a proxy for density anomalies. Where Argo EAPE is compared with our MHO estimates, we still use values drawn from *Roullet et al.* (2014), which are computed from density anomalies. The MHO-Argo comparisons are thus inconsistent in this way. The errors introduced in using temperature as a proxy for density are examined using in-situ data from McLane profilers (*Doherty et al.*, 1999). Because MHO temperature time-series data is generally too sparse in the vertical direction to allow for the quantification of oceanic stratification at mooring locations, we use the World Ocean Atlas 2009

(WOA: *Locarnini et al.*, 2010; *Antonov et al.*, 2010) records to compute background Brunt-Väisälä buoyancy frequency at the mooring sites. For the sake of clarity, EAPE calculated from a combination of MHO data and WOA climatology will be referred to as "MHO EAPE."

2.2.1 Models

EAPE is computed from runs of the Naval Research Laboratory (NRL) Global Ocean Forecast System (GOFS: *Metzger et al.*, 2014). The free-running simulation (hereafter, "simulation") and reanalysis both employ the HYbrid Coordinate Ocean Model (HYCOM) configured with 32 layers in the vertical direction, and an equatorial horizontal resolution of 0.08° ($\frac{1}{12.5^\circ}$ or 9 km) on a tripolar grid. The model is spun up for twenty years with the atmospheric forcing from an annual climatology of the National Center for Environmental Prediction Climate Forecast System (CFS) and is then run with hourly forcing from the CFS Reanalysis (*Saha et al.*, 2010) from 1993 to 2010 and from CFSv2 (*Saha et al.*, 2013) for the remaining two years (2011 and 2012). During the 20 year spin-up, the simulation stratification drifts away from climatology as will be seen later. Neither the HYCOM simulation nor the reanalysis contain tides. For the simulation, designated internally at NRL as GLBb0.08_expt10.2, daily means are archived on the Navy Department of Defense (DoD) Shared Resource Center (DSRC) at Stennis Space Center.

For the reanalysis, designated at NRL as GLBb0.08_expt19.0/19.1, an analysis using the Navy Coupled Ocean Data Assimilation system (NCODA: *Cummings and Smedstad*, 2013) is performed daily. Daily means are archived at the DSRC at Stennis Space Center and are available at the HYCOM consortium server (`https://hycom.org/dataserver/glb-reanalysis`). While the model code and configuration are fixed for the reanalysis, the observing network changes significantly over the twenty years. Both satellite altimeters and Argo floats are important sources

of observations to be assimilated in the reanalysis. Altimetric sea surface height anomalies are converted to synthetic profiles of temperature and salinity in NCODA. The number of altimeters available for assimilation varies between two and four over the twenty years of the run. During the last decade of the reanalysis, the Argo floats provide approximately 370 profiles of temperature and salinity per day.

While global maps of HYCOM EAPE are computed from one model year (2003), the full 20 year model output is used for our comparison to MHO EAPE. Because the model runs are 20 years in duration, we will refer to "20 year runs" and "20 years of output" although reanalysis output for year 2001 has been discarded due to data corruption in a large portion of the model output for that year. The majority of MHO records are of order one year in length, much shorter than the 20 year model outputs. To ensure a consistent comparison between the long model runs and the shorter in-situ MHO data sets, we analyze individual model years as well as 20 year means.

2.2.2 Observations

Argo global EAPE fields are obtained from *Roullet et al.* (2014) on a $\frac{1}{2}^\circ$ grid. *Roullet et al.* (2014) can be consulted for a discussion of the methods employed to extract EAPE from Argo floats. Discussions of the Argo array are given in numerous sources including *Roemmich and Owens* (2000), www.argo.net, and www.argo.ucsd.edu. For our later comparisons involving MHO data, Argo EAPE from the closest location and nearest depth to the MHO instrument in question is used.

Time-series of temperature from moored historical observations (MHO) are obtained from the Global Multi-Archive Current Meter Database (GMACMD: *Scott et al.*, 2010; *Timko et al.*, 2012, 2013), and can be found at `http://stockage.univ-brest.fr/~scott/GMACMD/gmacmd.html`. These records span from 1974 to 2008, and are generally not contemporaneous with the HYCOM runs or Argo data. To

avoid problems with abyssal temperature records, in which the small magnitude of the fluctuating temperature variations are not well resolved by the measurements, we use only instruments in water depths of 1,500 meters or less. Only locations with seafloor depths greater than 500 meters are included, owing to the lack of climatological data for computing buoyancy frequency on the shelf. Data within the mixed layer shallower than 60 meters are excluded; at such locations the buoyancy frequency is often locally very small, causing the numerical EAPE estimates (see Equation 2.1) to become unphysically large. Additionally, within the mixed layer, temperature anomaly correlates less strongly with density fluctuations as a result of density compensation (*Rudnick and Ferrari*, 1999). Finally, we use only instruments between $65°N$ and $65°S$ in order to eliminate locations where salinity fluctuations play a larger role in density anomalies; the sparsity of Argo in polar regions is another reason to exclude them.

We select MHO temperature time-series that are longer than 180 days, and exclude records containing gaps in the time-series. The remaining records are then visually inspected and quality controlled for instrument errors and other problems such as severe discretization of temperature anomalies, thermistor calibration drift, and non-stationarity in the variance of temperature signals. The total number of instruments excluded for these reasons is relatively small ($< 10\%$). Our selection criteria yields a total of 1,057 instruments distributed globally. The horizontal locations of the MHO instruments are given in the left panel of Figure 2.2. The spatial coverage is sparse and uneven. Some basins (e.g. the North Atlantic and North Pacific) are relatively well sampled, while others (e.g. the South Pacific) are sampled very little. The vertical coverage of the MHO dataset is given in the right panel of Figure 2.2. Generally, the number of records is larger in shallower depths (upper 500 or so meters). To remove high-frequency motions such as internal tides and internal gravity waves, we low-pass filter the MHO records using a second-order Butterworth filter with a 2

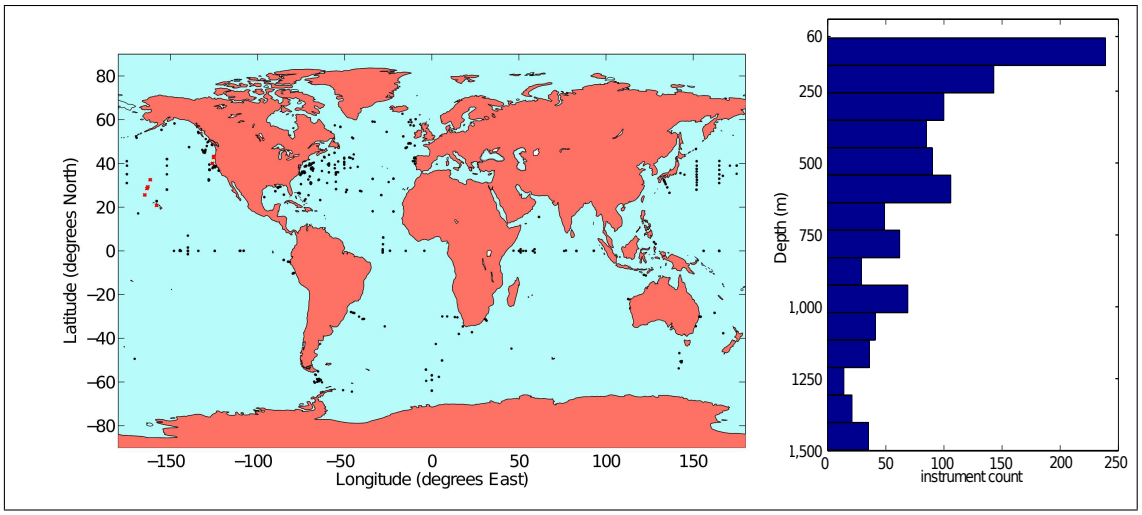

Figure 2.2: (Left) Horizontal locations of MHO instruments. Locations of McLane profilers used to test our use of temperature as a proxy for density are shown with a red X. (Right) Distribution of MHO instruments by depth, binned into 15 equally distributed depths from 60 to 1500m. Reprinted from *Luecke et al.* (2017).

day cut-off period. We also remove linear trends from the time series in order to remove seasonal trends not fully resolved by records shorter than a year. In order to validate our use of temperature time series in this chapter, we compare temperature and density variance using McLane in-situ profile data (*Doherty et al.*, 1999) at 10 locations marked by a red "X" in the left panel of Figure 2.2. At these 10 locations, time series of temperature and salinity were taken at selected depths between 200 and 1300 meters. This yielded a total of 31 distinct temperature and salinity time series where density variance could be compared with density variance using temperature as a proxy for density.

2.2.3 Calculation of EAPE

Consistent with the method of calculation used in the global Argo estimates (*Roullet et al.*, 2014), we use the "APE_3" term in *Kang and Fringer* (2010) to calculate EAPE. Note that, as is standard, the potential densities ρ and density anomalies ρ'

are computed with respect to the local vertical position. To first order, the "APE_3" term, adjusted by a factor of ρ_0, is given by:

$$EAPE = \frac{g^2 \rho'^2}{2\rho_0^2 N^2}, \tag{2.1}$$

where g is the acceleration due to gravity, ρ' is a seawater potential density anomaly defined as a departure from a time-mean of density, ρ_0 is the average density of seawater, and the square of the Brunt-Väisälä buoyancy frequency $N^2 = -\frac{g}{\rho_0}\frac{d\rho}{dz}$, where z represents the vertical coordinate. We have divided the *Kang and Fringer* (2010) EAPE by an additional factor of ρ_0, in order to obtain units consistent with the units given by *Roullet et al.* (2014).

For our HYCOM global map calculations, model density output at a depth of 500m is used to calculate density anomalies, and N^2 is calculated with a centered difference derivative using model output at 550m and 450m. For the computation of global averages from HYCOM maps, model output is interpolated to the Argo native resolution of $\frac{1}{2}^\circ$. Spatial averages are computed only over locations where both model output and Argo data is available.

In our analysis of the MHO, the buoyancy frequency is determined using WOA annual mean temperature and salinity climatology and the TEOS-10 Gibbs Sea Water equation of state package (*McDougall and Barker*, 2011). In the calculation of HYCOM EAPE at MHO locations, the modeled buoyancy frequency is computed from annually averaged model output interpolated to a depth level grid, in analogy to the WOA climatology used in conjunction with the MHO data.

For the calculation of MHO and HYCOM EAPE at MHO locations, we estimate a density anomaly ρ' from the temperature anomaly T', using a linearized equation of state for seawater:

$$\rho' \approx \rho_0[-\alpha T' + \beta S'] \approx -\rho_0 \alpha T', \tag{2.2}$$

where α and β are the thermal expansion and haline contraction coefficients of seawater respectively. The prime notation again denotes a departure from the time-averaged value, and the salinity term S' is dropped due to its absence in most historical in-situ measurements. For consistency, the salinity term is also dropped in the calculation of HYCOM EAPE at MHO locations. The coefficient α is calculated locally at instrument locations and depths from either the World Ocean Atlas climatology (for MHO data) or from annual averages (for HYCOM output.)

2.2.4 Statistical Analysis

We use several metrics to quantify differences between EAPE in HYCOM and observations. For our global comparisons of HYCOM and Argo, we present global area-weighted averages of EAPE. For our MHO location comparison, we present HYCOM, MHO and Argo EAPE, as well as the constituent terms in the calculation of the EAPE, T'^2 and N^2. A linear regression coefficient A for EAPE is calculated using standard methods. The ratio γ of the means of the model and observations is defined as:

$$\gamma = \frac{\sum_{i=1}^{n} EAPE_{model}}{\sum_{i=1}^{n} EAPE_{observed}}, \tag{2.3}$$

where i is a location index and n is the total number of MHO instruments used in the calculation. Additionally, a correlation coefficient R is calculated between pairs of estimates (model, MHO, Argo) across the MHO locations. The ideal values expressing a perfect comparison are equal to one for all of the metrics A, γ, and R. Following the above methodology, means and correlations for the constituent terms T'^2 and N^2 are also calculated. Comparison statistics denoted as "20 year mean" are calculated on output that has been binned yearly, then averaged over 20 years, and then spatially averaged, prior to the calculation of statistics.

In order to quantify improvement between the model simulation and reanalysis,

we employ a skill score used in *Murphy* (1988). The skill score (SS) is defined as:

$$SS(R, S, Obs) = 1 - [MSE(R, Obs)/MSE(S, Obs)], \tag{2.4}$$

Where the mean square error (MSE) is defined as:

$$MSE(R, Obs) = \frac{1}{n}\sum_{i=1}^{n}(R_i - Obs_i)^2, \tag{2.5}$$

Where R denotes model reanalysis predictions, S denotes model simulation predictions, and Obs denotes the observational predictions. In the case of our global comparisons with Argo, we use EAPE predictions, and in the case of our Model vs. WOA comparisons we use temperature variance. The skill score is positive when the accuracy of the reanalysis is greater than that of the simulation. $SS = 1$ represents a reanalysis that perfectly matches observations ($MSE(R, Obs) = 0$), while $SS = 0$ when $MSE(R, Obs) = MSE(S, Obs)$, representing no improvement in the reanalysis. Multiplying by 100 translates SS into a measure of percent improvement.

Because we present spatial means as a metric for comparison between our model runs and observational data, it is convenient to include estimates of the error of these means. We employ bootstrap methods to estimate 95th percentile confidence intervals on our means. Bootstrapping is performed with N=1000 bootstrap re-samples of our original data. In the case of our global area-weighted integrals, where the global integral and non-weighted average differ slightly, we estimate the percent error using the global average, and apply it to the global integral.

2.3 Results

We first present global maps of EAPE from HYCOM and Argo. We then examine HYCOM, Argo, and MHO EAPE at the MHO locations. We compare HYCOM and

MHO values of the EAPE constituent terms N^2, the square of the Brunt-Väisälä buoyancy frequency, and T'^2, the square of the low-passed temperature anomalies.

2.3.1 Global EAPE Maps

Global maps of EAPE at 500m computed from the HYCOM simulation and reanalysis (top and middle panels respectively, of Figure 2.3) show spatial structures consistent with the Argo map (bottom panel), such as increased EAPE in western boundary currents and in the Southern Ocean. Because Argo, as well as other observations including satellite altimetry, are used as a source of assimilative observations for the reanalysis, one would expect that the reanalysis EAPE maps would more closely reproduce Argo estimates, and this is indeed the case. The spatial structure in the reanalysis more closely resembles the Argo structure in several respects, confirming the added value of data assimilation. Perhaps the most apparent improvement is the lack of an artificial South Atlantic "eddy train" in the reanalysis. The simulation contains a distinctive "eddy train," resulting from eddies escaping the Agulhas Current into the South Atlantic. We note that this "eddy train" is not a unique feature of the HYCOM simulation, and can be seen in other high-resolution simulations (*Maltrud and McClean*, 2005), where the train was diagnosed using sea surface hight variance and was not seen in altimeter observations. One possible cause of this "eddy train" is illustrated in *McClean et al.* (2011), where introduction of ocean-atmospheric fluxes in a coupled model is shown to improve the realism of these eddies. It is also possible that improvements in the ocean-atmosphere wind shear implemented in HYCOM could improve the dynamics in the region. The train results in a large local over-estimation of EAPE in the simulation when compared to Argo, while much of the rest of the simulation South Atlantic EAPE is below the Argo values. In the reanalysis however, the eddy train is no longer apparent, and the rest of the South Atlantic is more energetic, in line with the Argo maps.

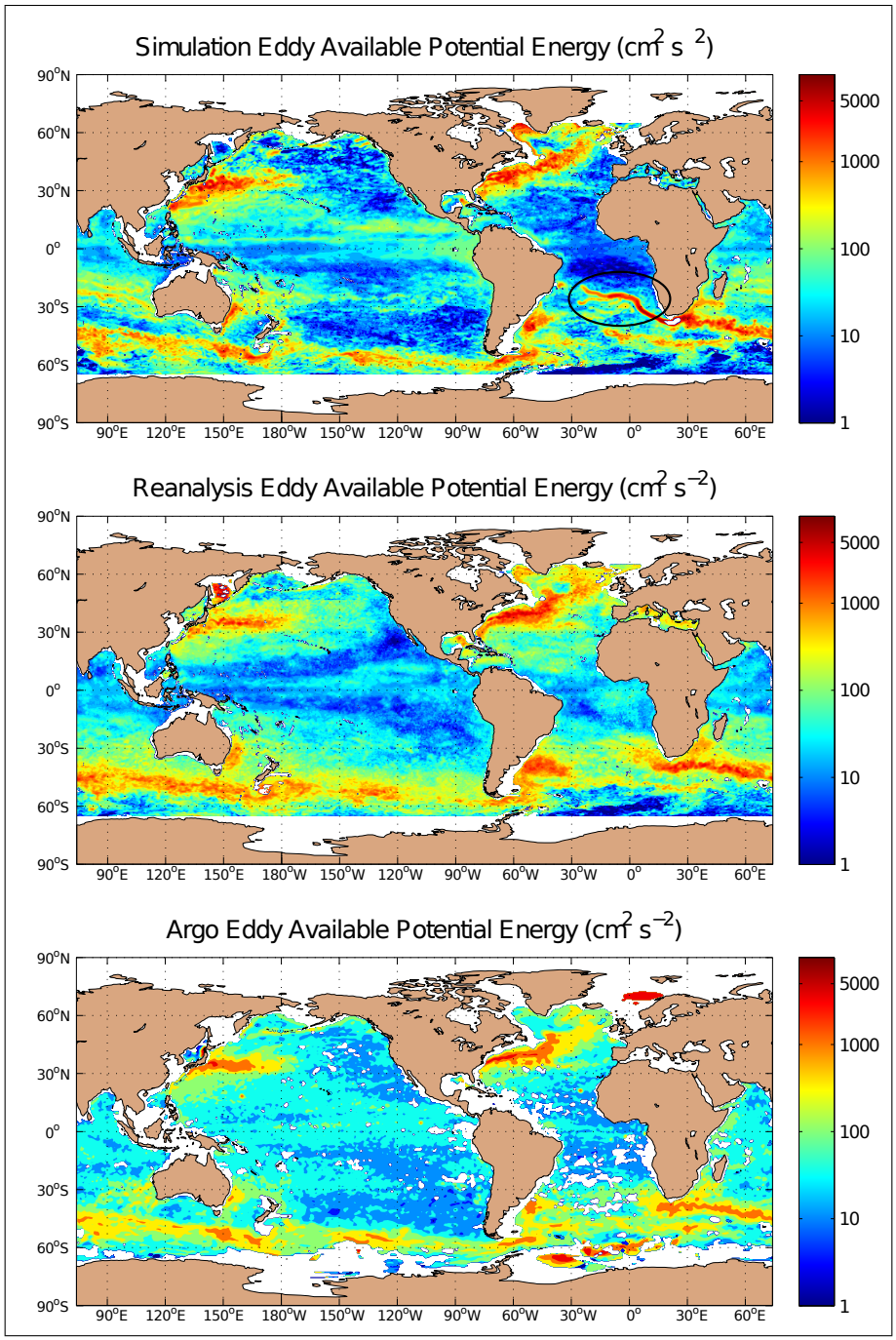

Figure 2.3: Global EAPE ($\mathrm{cm}^2 s^{-2}$) at 500 meters depth in the (top) HYCOM simulation, (middle) HYCOM reanalysis, and (bottom) *Roullet et al.* (2014) Argo analysis. The eddy "train" discussed in the results section is encircled in the top sub-figure. In this figure, both HYCOM maps are given on a $\frac{1}{4}^\circ$ grid while the Argo map is shown on its native $\frac{1}{2}^\circ$ resolution. Reprinted from *Luecke et al.* (2017).

The reanalysis also matches the spatial structure of the Argo maps in the Kuroshio and Gulf Stream regions more closely than the simulation does. For instance, in both Argo and the HYCOM reanalysis, the Gulf Stream hooks northward at about 45°W, while the HYCOM simulation does not. There are a number of factors that may cause a model to differ from observation. *Chassignet and Xu* (2017), for instance, show that resolution plays a role in the realism of the Gulf Stream. While the model runs used in this chapter contain an energetic eddy field, they lack sufficient resolution to accurately portray all featured of western boundary currents (*Thoppil et al.*, 2011). While the simulation over-estimates EAPE in the Indian Ocean between 10°S and 30°S, the reanalysis predicts EAPE values closer to that of Argo. On the other hand, the simulation arguably recreates more accurately the 500m EAPE fields in the near equatorial Pacific, and parts of the Southern Ocean.

Figure 2.4 displays point to point comparisons of the 500m EAPE values between (left) the simulation and Argo, and (right) the reanalysis and Argo. Model output was decimated to the Argo native resolution of $\frac{1}{2}^\circ$ for both global point-to-point scatterplots. The simulation exhibits more scatter, and lower correlation with respect to Argo, with $R = 0.52$ and $R = 0.65$ for the simulation and reanalysis respectively. To further quantify differences between the simulation and reanalysis, we compute a skill score (SS). Globally referenced to Argo EAPE, the skill score for HYCOM is $SS(\mathrm{R}_{EAPE}, \mathrm{S}_{EAPE}, \mathrm{Argo}_{EAPE}) = 0.50$ implying that the modeled EAPE is improved by close to 50 percent in the reanalysis compared to the simulation through the introduction of data assimilation.

The visual impression from Figure 2.3 is that the HYCOM simulation and reanalysis are both more energetic than the Argo maps. We confirm this by computing global averages (left column of Table (2.1)). The model simulation provides the highest estimate with a global average EAPE of 185 ± 6 cm$^2 s^{-2}$, while the reanalysis is slightly lower at 183 ± 4 cm$^2 s^{-2}$. EAPE estimated using Argo provides the lowest global

estimate at 168 ± 4 cm$^2 s^{-2}$, about 10% lower than the HYCOM estimates. Zonal averages of EAPE (Figure 2.5) demonstrate that both the simulation and reanalysis reproduce the qualitative structure of observed Argo EAPE between about $60°N$ and $55°S$. However both model runs generally predict slightly higher values of EAPE than does Argo between these latitudes. In the Southern Hemisphere between $35°S$ and $55°S$, the reanalysis over predicts EAPE. However the peaks are more closely positioned in latitude in the Argo observations when compared to the simulation, which has a peak EAPE that is slightly shifted to the North. The simulation also has local EAPE maxima just poleward of $20°N$ and $20°S$ that do not appear in either the reanalisys or in Argo. From $30°N$ - $60°N$, both model runs agree closely in both latitudinal dependence and magnitude. However, once again, the simulation predicts a maximum EAPE slightly shifted towards the equator than either the reanalysis or Argo. Poleward of $55°S$ and $60°N$, there is a marked disconnect between Argo and HYCOM, with HYCOM exhibiting much higher zonal EAPE in the north, and much lower zonal EAPE in the south. In polar regions, weak stratification causes issues with our expression for EAPE. Additionally, south of $55°S$ Argo observations generally becomes sparse. These factors are most likely one cause of the somewhat poor model-data agreement in these regions.

Prompted by the differences between the HYCOM and Argo EAPE maps, we present another observational EAPE estimate for comparison to HYCOM and Argo values. In the next 3 sections we compute EAPE from HYCOM, Argo, and MHO at the individual locations of the MHO instruments. We also compare the constituent terms used in our calculation of EAPE, using HYCOM output and MHO/WOA data.

Table 2.1: Means of EAPE, computed over the entire globe (left column), and over all available MHO locations (right column), for MHO, Argo, HYCOM simulation and reanalysis. For the global calculations, we use model year 2003 for the HYCOM simulation and reanalysis, and for the MHO comparison, HYCOM 20-year means are used.

Mean EAPE (cm^2s^{-2})		
	global	at MHO locations
Simulation	185 ±6	600 ±90
Reanalysis	183 ±4	598 ±87
MHO	N/A	709 ±143
Argo	168 ±4	462 ±55

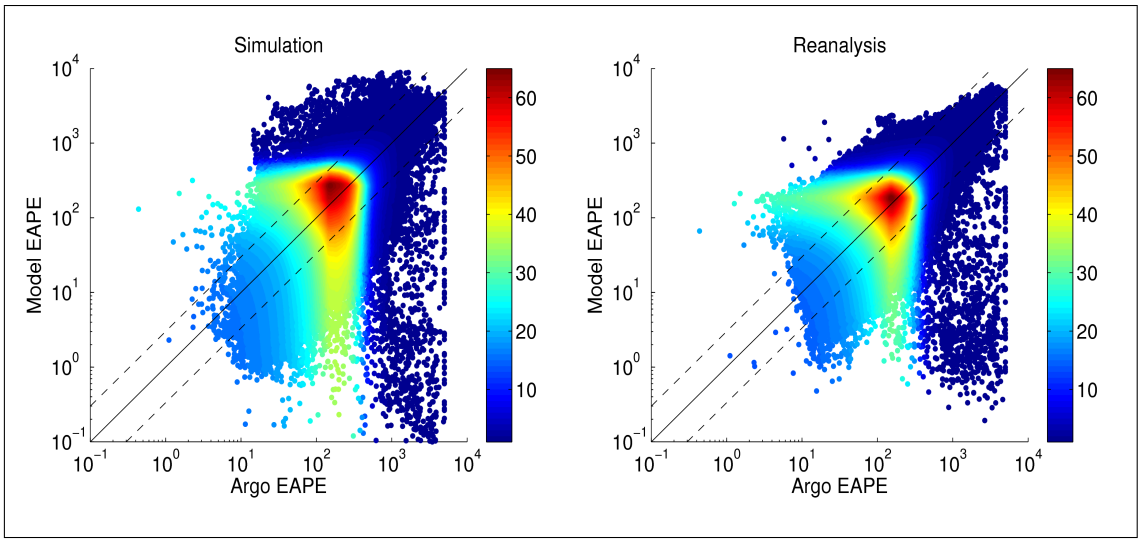

Figure 2.4: A point-to-point comparison of global EAPE ($cm^2 s^{-2}$) at 500m (a) between simulation and Argo, and (b) between reanalysis and Argo. Population density is given by color, with the most tightly grouped data shown in red, and the sparsest data in blue. The one-to-one line is shown in black along with bounding lines representing a factor of 3. Reprinted from *Luecke et al.* (2017).

2.3.2 Stratification

We compare N^2 in HYCOM versus the WOA observational climatology at the MHO locations shown in Figure 2.2. Both the simulation and reanalysis stratifications are initialized from the same 20 year spin-up period with climatological forcing. However, during the spin-up period, the simulation drifts away from the WOA climatology. We might expect that once inter-annual forcing is applied during the 1993-2012 analysis period, the simulation will remain relatively far from climatology, whereas the data assimilation employed in the reanalysis should result in more accurate model stratification. Consistent with this expectation, the reanalysis outper-

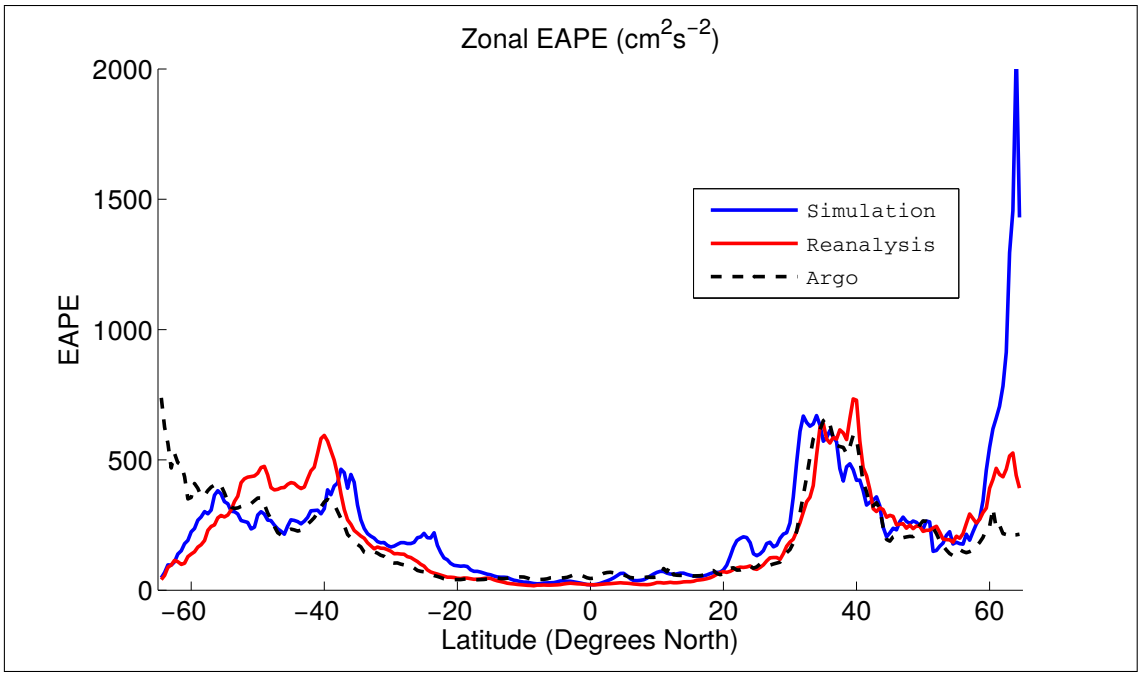

Figure 2.5: Zonal-mean distribution of EAPE (cm$^2 s^{-2}$) for simulation, reanalysis, and Argo. Reprinted from *Luecke et al.* (2017).

forms the simulation with respect to climatological stratification over the duration of the model runs. A comparison of the stratification in the HYCOM runs versus WOA is shown in Figure 2.6. The scatter in Figure 2.6a (20 year simulation average vs. WOA annual average) is visually greater than in Figure 2.6b (20 year reanalysis average vs. WOA annual average). Both the reanalysis and the simulation have linear regression coefficients A and ratios of the means γ that are very close to one (Table (2.2)), suggesting that when averaged over MHO locations, the model shows fairly good skill with respect to reproducing accurate stratification. When viewed in the context of point to point correlation, the reanalysis shows notable improvement, with correlation being higher between the reanalysis and WOA ($R = 0.97$) than between the simulation and WOA ($R = 0.78$). In a free-running simulation, the forcing that produces the stratification in the model is independent of the climatological stratification that was used to initialize the run. The dynamic stratification produced in the model is a product of the mixing occurring within the model. It is possible that

the simulation drifts from the climatology because of inaccuracies in model mixing dynamics.

Table 2.2: Statistical metrics and 20 year means for EAPE constituent terms, the square of the temperature anomaly and the square of the buoyancy frequency at MHO locations, denoted by terms in$\langle\rangle$.

	Temperature Variance				Stratification			
	$\langle T'^2\rangle_{MHO}{}^\circ C^2$	$A_{T'^2}$	$\gamma_{T'^2}$	$R_{T'^2}$	$\langle N^2\rangle_{WOA}10^{-4}s^{-2}$	A_{N^2}	γ_{N^2}	R_{N^2}
Data	0.95 (MHO)				0.50 (WOA)			
Simulation	1.06	0.68	1.10	0.54	0.56	1.00	1.15	0.78
Reanalysis	1.08	0.83	1.12	0.76	0.50	1.00	1.02	0.97

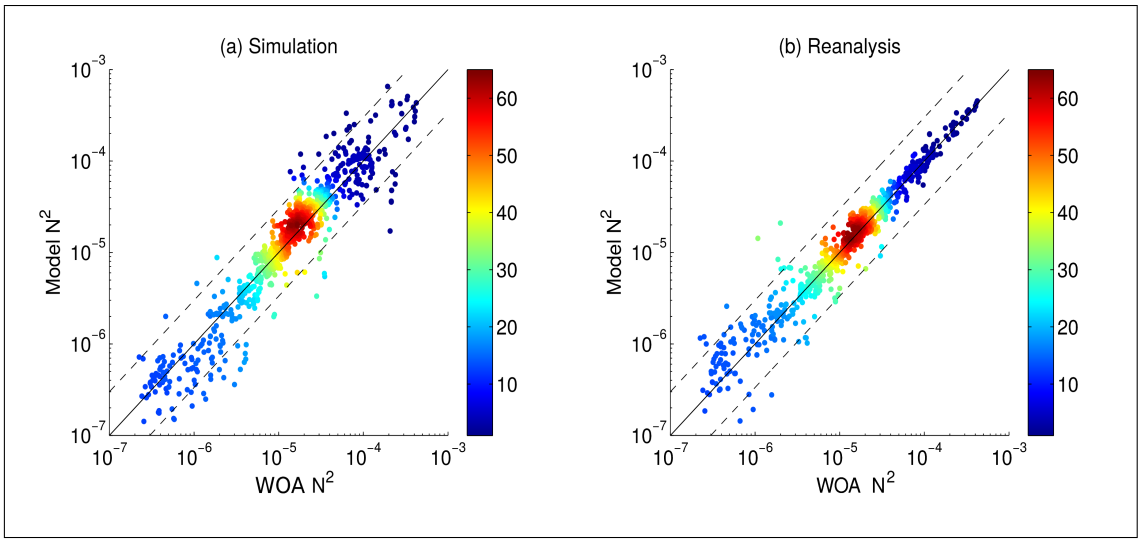

Figure 2.6: Global point-to-point comparison of squared Brunt-Väisälä buoyancy frequency (s^{-2}) at MHO locations, averaged over 20 years of model output (a) between simulation and WOA, and (b) between reanalysis and WOA. Population density is given by color, with the most tightly grouped data shown in red, and the sparsest data in blue. The one-to-one line is shown in black along with bounding lines representing a factor of 3 as described in Figure 2.4. Reprinted from *Luecke et al.* (2017).

To illustrate the temporal drift of model stratification, we display in Figures 2.7a-c the vertical profiles of N^2, spatially averaged over the locations shown in Figure 2.2 for model years 1993, 2002, and 2012. The N^2 profile in the simulation has a maximum that is slightly deeper than seen in WOA. The maximum N^2 values in the reanalysis, while slightly larger than those in WOA, occur at depths that are noticeably closer to the depths seen in WOA. It is also evident that the temporal drifts in the stratification are greater in the simulation than in the reanalysis, with the pycnocline both broadening and deepening over time. The temporal drift of the stratifications in the reanalysis and the simulation is also seen in Figure 2.7d, which

displays the yearly spatially averaged N^2 profiles in the upper 300 meters. From this it is clear that the HYCOM reanalysis more closely recreates the depth of maximum stratification than does the simulation. It is important to note that the stratification drift of the model, along with the background stratification used in our calculation of MHO EAPE is biased toward the summer seasonal pycnocline. As many of our MHO observations are located shallower than 250m, this most likely contributes to a bias in both our model and MHO EAPE estimates at MHO locations presented in Section 2.3.4, as well as in the stratification temporal drift discussed here. Furthermore, as we are averaging over a globally distributed data-set of MHO locations, there is certainly introduced bias from global-merging of stratification. We believe however, that despite this, spatial and yearly means of N^2 still provide a useful metric to diagnose model performance.

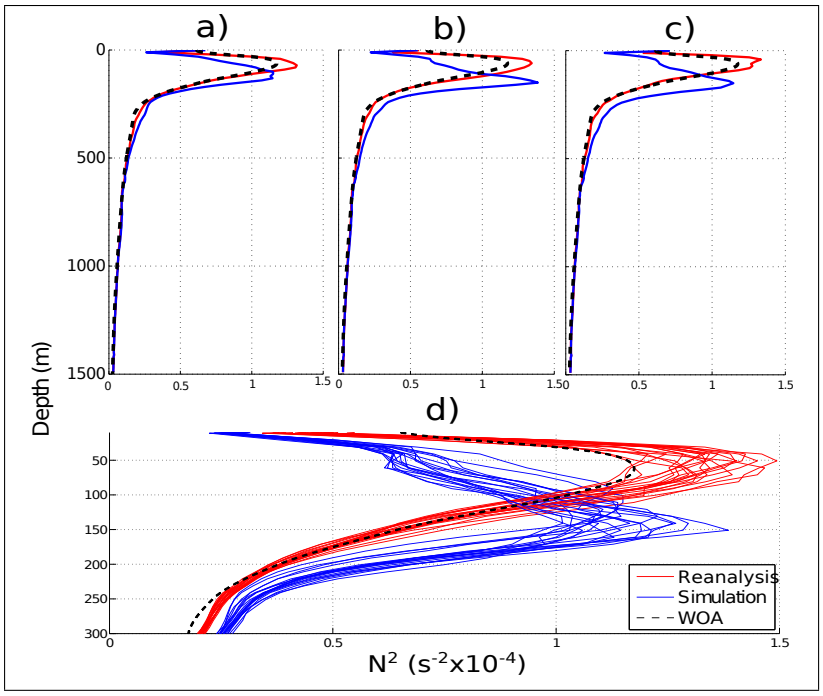

Figure 2.7: Vertical profile of spatially averaged buoyancy frequency N^2 (s^{-2}) in HYCOM and WOA taken over comparison points shown in Figure 2.2. Profiles are shown of yearly averaged snapshots of model output for a) 1993, b) 2002, c) 2012, and, d) profiles for all years of model output over the upper 300m of water column. In all subplots, we display the WOA annual profiles averaged over the same locations. Reprinted from *Luecke et al.* (2017).

2.3.3 Temperature and Density Anomaly

In this section we compare T'^2 between HYCOM and MHO. However, before we discuss the results of the MHO analysis, we display some typical model results at selected locations. Frequency spectra of the low-passed temperature anomalies at individual locations for MHO records, simulation, and reanalysis are shown in Figure 2.8. The simulation and reanalysis results are computed from model year 1993. The corresponding annually averaged Brunt-Väisälä stratification frequency profiles from

the WOA climatology, simulation, and reanalysis output are also shown. Note that inter-annual EAPE variability in the model output does not appear to have significant impact on the agreement between model and data at most locations.

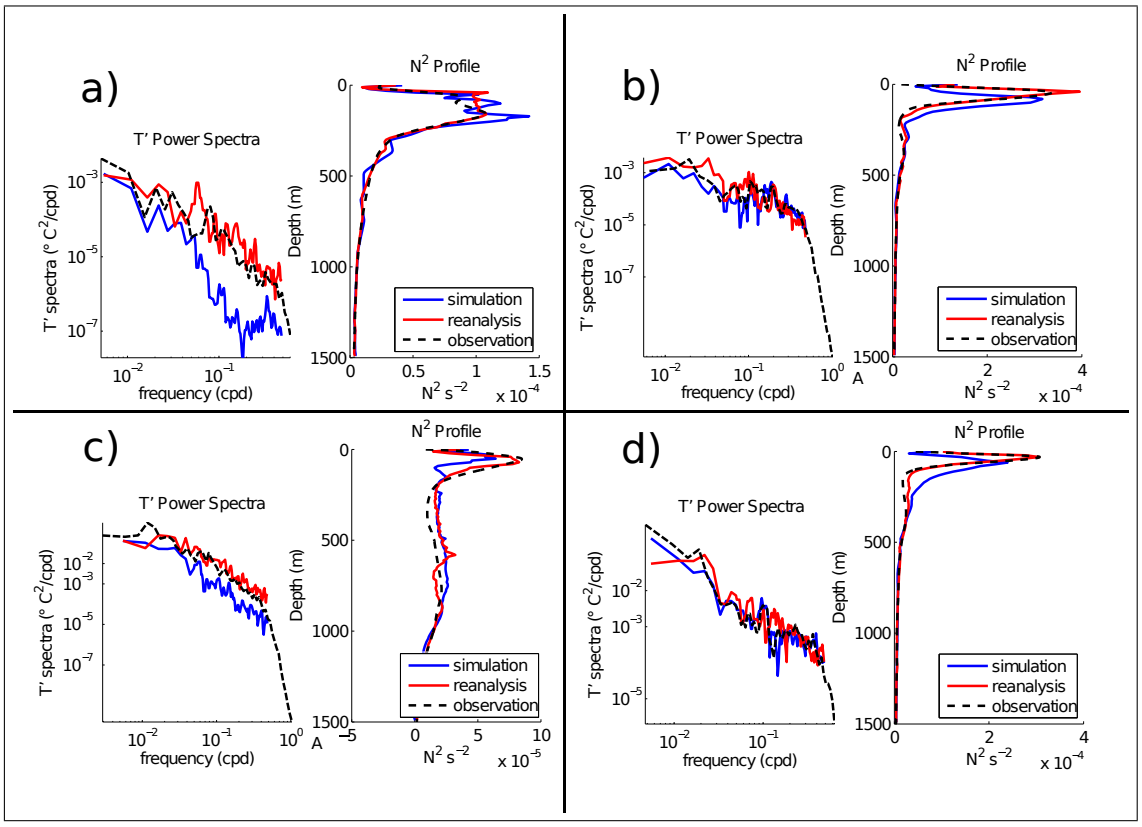

Figure 2.8: Temperature anomaly frequency spectra (at depths given below) and annual average N^2 profiles, for 1993 HYCOM simulation and reanalysis output, showing different levels of agreement with spectra computed from MHO observations (left plots) and N^2 computed from WOA observational climatology (right plots). Locations are: a) 32.44°N, 127.769°W (454m), in the North-Eastern Pacific, b) 0.02°S, 110.21°W (927m) in the Eastern Equatorial Pacific, c) 37.8°N, 55.7°W (497m) in the Gulf Stream, and d) 5.96°S, 82.50°W (100m) off the coast of Peru. Reprinted from *Luecke et al.* (2017).

At the locations shown in Figures 2.8a and 2.8c, the simulation temperature spectra fall off more steeply at periods shorter than $\sim$ 20 days (0.05 cycles per day (CPD)), while the reanalysis spectra lie closer to the MHO spectra. In Figures 2.8b and 2.8d, both the simulation and reanalysis temperature frequency spectra are in fairly close agreement with the MHO spectra. While HYCOM displays some skill at many locations, records exist where much of the variance occurring at periods of less than $\sim$ 20 days is not captured by the dynamics of the simulation alone. It is possible that assimilation in the reanalysis introduces some of this unresolved low-frequency mesoscale energy. At the same time, data assimilation increments can introduce artificially high levels of gravity waves through geostrophic adjustment. However, any such excess high-frequency energy would be reduced by the daily averages employed here. The better agreement of the reanalysis EAPE maps with Argo EAPE maps, as is seen in the global model vs. Argo comparison of Figure 2.3, and the close agreement of the globally averaged EAPE in the reanalysis versus the simulation, suggest that the data assimilation is not introducing gross inaccuracies in the reanalysis, at least in the daily averaged fields. Further evidence of this is seen in the frequency spectra of the reanalysis shown in Figure 2.8; no artificial peaks are seen as one approaches the high frequencies characteristic of gravity waves. At all four locations shown in Figure 2.8, buoyancy frequency profiles reveal a greater accuracy in the reanalysis over the simulation, consistent with the discussion in Section 2.3.2.

A point-to-point comparison of T'^2 in HYCOM vs. MHO, shown in Figure 2.9, reveals substantial scatter but a small bias. The scatter in the reanalysis plot (Figure 2.9b) is marginally tighter than that in the simulation plot (Figure 2.9a). However, the reduction in the scatter between the reanalysis and simulation comparisons with MHO for T'^2 is not as visually striking as in the comparison with WOA of N^2 (Figure 2.6). While Table 2.2 shows that the correlation between the model and MHO T'^2 is improved in the reanalysis ($R = 0.76$) vs. the simulation ($R = 0.54$), the reanalysis

overestimates T'^2 slightly more in a spatial average than does the simulation, as can be seen in the ratio of the means ($\gamma = 1.12$) vs. ($\gamma = 1.10$) for the reanalysis and simulation respectively. We compute the skill score (SS) of HYCOM with respect to MHO T'^2 as a metric for examining the impact of data assimilation on HYCOM. We find the skill score $SS(\mathrm{R}_{T'^2}, \mathrm{S}_{T'^2}, \mathrm{MHO}_{T'^2}) = 0.47$, again implying a close to 50 percent improvement between the reanalysis and simulation. The large spread in the comparisons of T'^2 dominates the scatter seen in our EAPE comparison in the next section, and will be further addressed in Section 2.4.

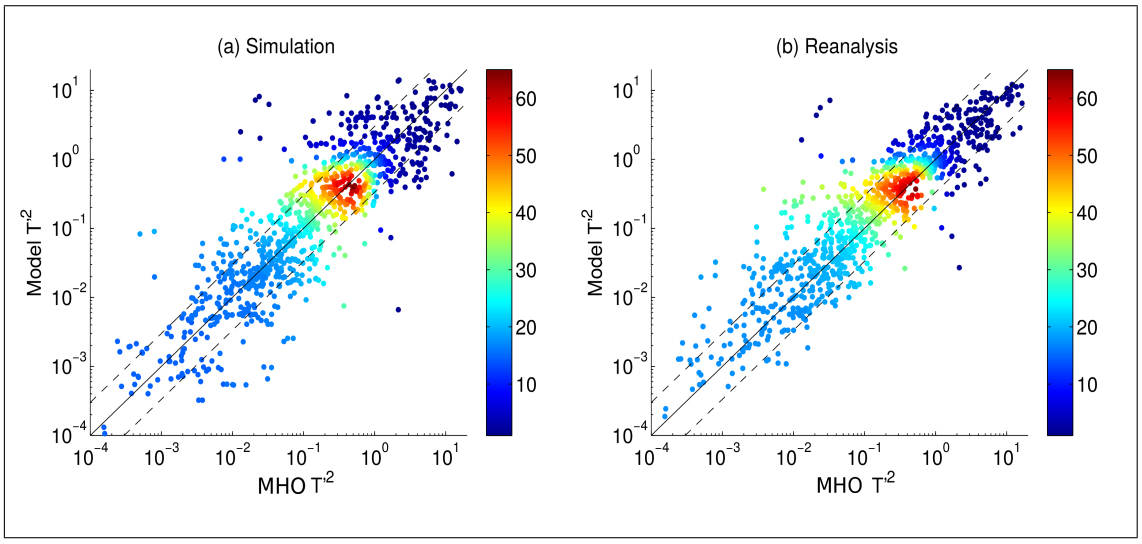

Figure 2.9: As in Figure 2.4, but for a point-to-point comparison of 20 year averaged T'^2 ($^\circ C^2$) (a) between simulation and MHO, and (b) between reanalysis and MHO. Reprinted from *Luecke et al.* (2017).

To test the accuracy of the approximate linearized equation of state discussed in Section 2.2.3, we compare the square of the inferred density anomaly $(-\rho_0 \alpha T')^2$ against the square of the density anomaly ρ'^2 calculated from the full non-linear equation of state (*McDougall and Barker*, 2011). The left panel of Figure 2.10 displays a scatterplot of inferred verses actual density values taken from the HYCOM reanalysis

at MHO locations. The right panel of Figure 2.10 displays the same comparison at the McLane profile locations described in section 2.2.2, where observations of both temperature and salinity are available. In both cases, the majority of locations lie close to the 1:1 line. In both the HYCOM and McLane exercises, the correlation between the actual and inferred density anomaly is $R = 0.93$. The reasonably good comparison seen in Figure 2.10 suggests that the error in EAPE introduced via this approximation (Equation 2.2) is smaller than other sources of scatter (discussed below, and in Section 2.2.4).

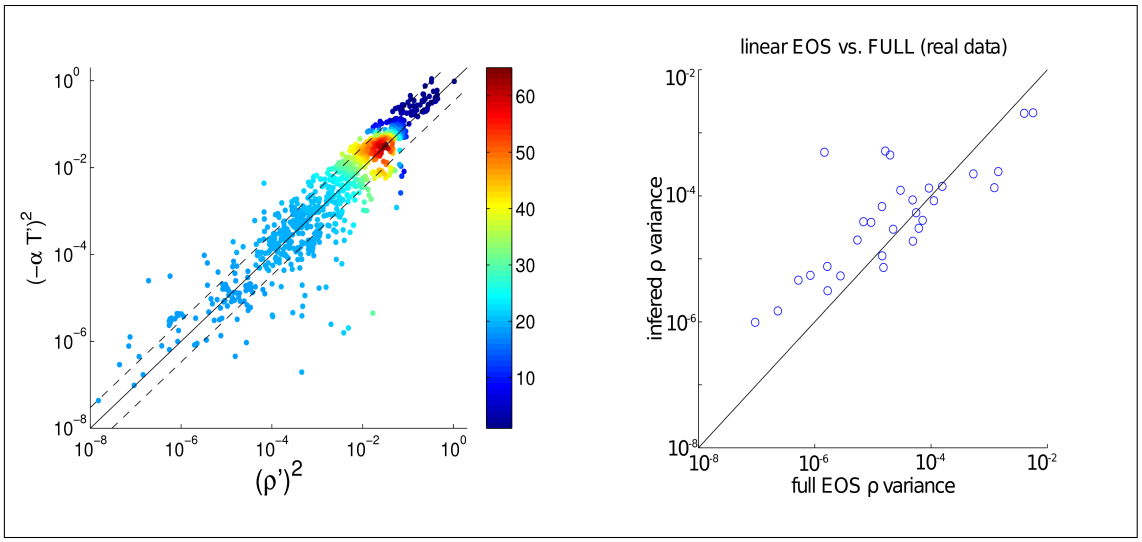

Figure 2.10: (Left) As in Figure 2.4 but for a comparison of the squared inferred density anomaly $(-\rho_0 \alpha T')^2$ against the actual squared density anomaly ρ'^2 calculated using the full non-linear equation of state (*McDougall and Barker*, 2011), with HYCOM reanalysis salinity and temperature fields as inputs at MHO locations. (Right) A similar comparison performed at 31 depths over 10 locations using in-situ McLane profiler temperature and salinity data. Units are $(\frac{kg}{m^3})^2$. Reprinted from *Luecke et al.* (2017).

2.3.4 MHO EAPE

Both the simulation and reanalysis EAPE, averaged over all MHO locations, are about 16% lower than the MHO EAPE (Table (2.1)). The HYCOM bias to lower energies evident in Table (2.1) can also be seen in the scatterplots of EAPE in Figure 2.11, where the bulk of the HYCOM points compared fall slightly to the right of the 1:1 comparison line. The reanalysis vs. MHO EAPE scatterplot (Figure 2.11b) does show a marginally tighter clustering than the scatterplot of EAPE in the simulation vs. MHO (Figure 2.11a). The statistical comparison metrics outlined in Section 2.2.4 display similar trends for the HYCOM comparisons to both MHO and Argo Table (2.3). The value of γ effectively remains constant from the simulation to the reanalysis, while the linear regression coefficient A shows a slight improvement in the reanalysis when compared to the simulation. It is clear that R, the model correlation with MHO on a point to point basis, is improved in the reanalysis ($R = 0.84$) versus the simulation ($R = 0.56$), and this trend is repeated when the model EAPE is compared to Argo at the same locations ($R = 0.62$ vs. $R = 0.47$ respectively). Both model runs tend to slightly under estimate the EAPE relative to MHO estimates, although all mean EAPE values are comparable, especially when one considers the wide scatter shown in Figure 2.11.

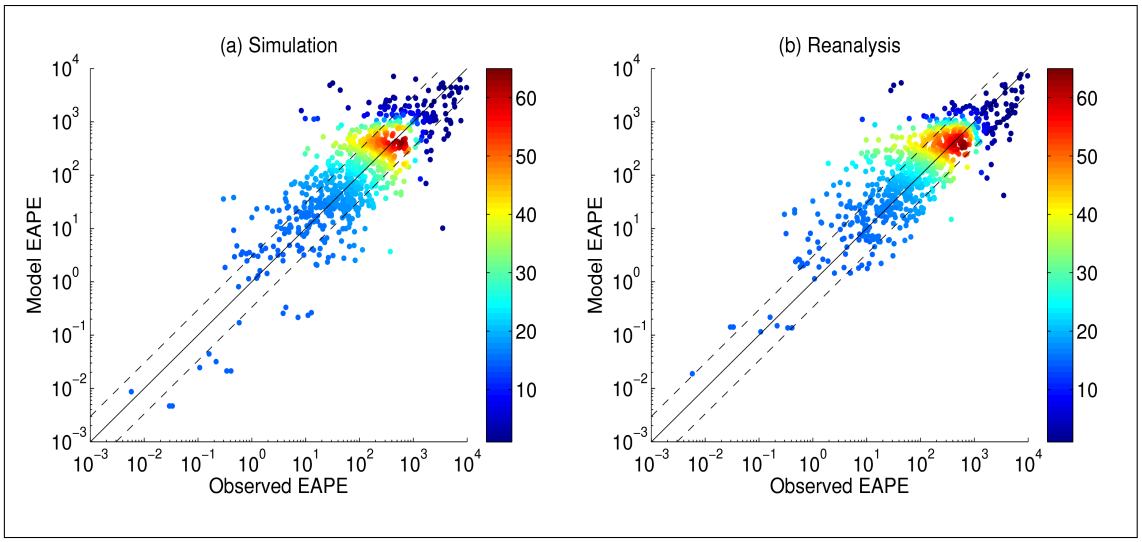

Figure 2.11: As in Figure 2.4, but for a point-to-point comparison of EAPE ($cm^2 s^{-2}$) (a) between a 20 year average of the simulation and MHO, and (b) between a 20 year average of the reanalysis and MHO. Reprinted from *Luecke et al.* (2017).

Lastly, we compare our EAPE results at MHO locations with the EAPE calculated from Argo floats (*Roullet et al.*, 2014). Because of the relatively frequent temporal sampling of the MHO records, we are able to provide estimates of the amount of aliasing that may be present in the Argo EAPE estimates. As a proxy for Argo sampling, we subsample the MHO records at 10 day intervals, and compute the variance. As in *Roullet et al.* (2014), any motions that occur at periods less than ten days will be aliased into the Argo-like estimate of low-frequency variance. We also compute variance from a 10 day low-pass of the MHO temperature time series. The variance computed from the 10 day low-pass does not contain aliased high-frequency motions. We find that 32% of the variance in the Argo-like estimates is due to aliased contributions from motions with periods of 10 days or less. Because the MHO EAPE estimates presented here employ a two day low-pass filter, some but not all of the

aliased energy that is in Argo is included in our MHO EAPE estimates. By comparing the variance in the Argo-like sampled MHO observations with the two day low-passed MHO data used in this chapter, we conclude that Argo should over estimate EAPE by about 15% when compared to our MHO predictions, suggesting that in the locations of the MHO comparison, the true observed low-frequency energy should be slightly less than the the low-frequency Argo EAPE estimates. It is worth noting however, that the Argo model still predicts the lowest EAPE estimates when averaged over MHO locations (Table (2.1)).

As shown in Figure 2.12, the vertical profiles of spatial mean EAPE between the simulation, reanalysis, MHO, and Argo at MHO locations are in qualitative agreement, with all EAPE estimates having a local minimum at about 200m, and a local interior maximum between 300 and 700m. For many of the depths between 200 and 600m, it is worth noting that both model EAPE predictions are "bounded" by observations, with MHO serving as an upper limit, and Argo EAPE representing a lower limit. The globally- and depth-averaged EAPE values given in Table (2.1) display similar trends; Argo is the lowest estimate, MHO is the highest estimate, and the models fall in between. The vertical profile of spatially averaged EAPE shown in Figure 2.12 is presented as a useful and interesting metric. However, due to the sparse sampling in the vertical, as well as the spatial sampling bias depicted in Figure 2.2, it is not representative of the global vertical structure of EAPE.

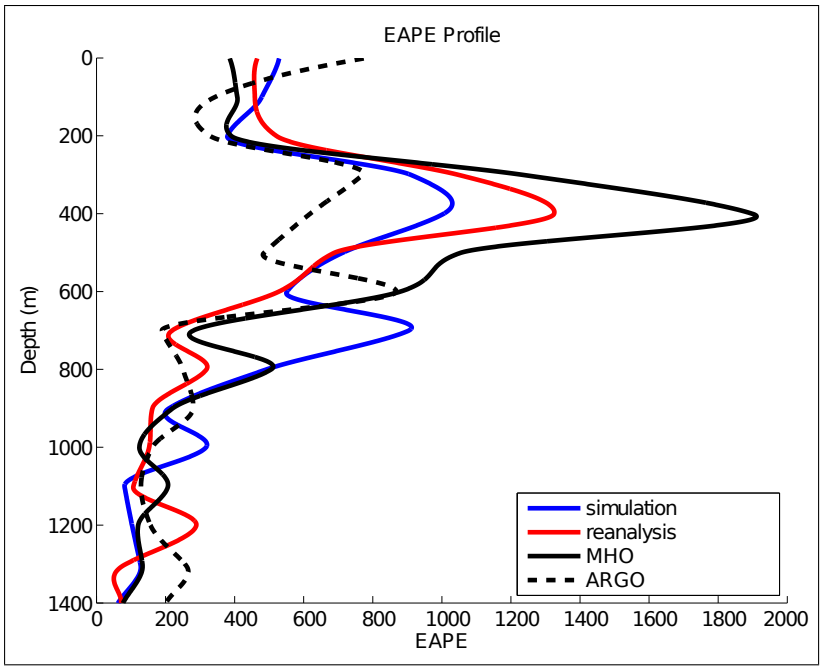

Figure 2.12: Vertical distribution of EAPE ($\mathrm{cm}^2 s^{-2}$) for simulation, reanalysis, MHO, and Argo over MHO locations. EAPE is binned into 15 evenly distributed depth bins in the vertical, and then splined for continuity. Reprinted from *Luecke et al.* (2017).

Scatterplots of HYCOM and MHO EAPE values against Argo EAPE values, at the MHO locations shown in Figure 2.2, are displayed in Figure 2.13. Although on a point-to-point basis, the subplots in Figure 2.13 show large scatter, it is also true that EAPE calculated from the MHO, simulation and reanalysis are close to values in *Roullet et al.* (2014) when spatially averaged. As shown in Table (2.1), the spatial means of both the simulation and reanalysis EAPE (600 $\pm$90 and 598 $\pm$87 $cm^{-2}s^{-2}$ respectively) lie between the mean values inferred from MHO and Argo (709 $\pm$143 and 462 $\pm$55 $cm^{-2}s^{-2}$ respectively). The large errors of the EAPE calculated at MHO locations in comparison to our global EAPE estimates are due to the decreased sample size of our MHO database. Both the simulation and reanalysis EAPE are less than 16% lower than MHO and less than 30% higher than Argo estimates, and all four mean EAPE

values are within a factor of 1.5 of one another Both the simulation and reanalysis EAPE means lie within the error bars of MHO and Argo, however the estimated error in Argo EAPE and MHO EAPE at MHO locations do not overlap. Interestingly, the scatter seen in MHO versus Argo EAPE estimates ($R = 0.60$) is comparable to the scatter in the comparisons of the HYCOM simulation and reanalysis versus Argo given in Table (2.3). The fact that two different observationally-based EAPE estimates yield a similar scatter to that seen in the model-Argo comparisons reinforces the notion that such model-data comparisons of mesoscale eddy fields are prone to large scatter. In the following section, we use an idealized model to show the influence of sampling times on this scatter.

Table 2.3: Statistical comparison metrics (see text for definitions) for EAPE between HYCOM (computed using 20 years of output) and observations (MHO and Argo).

Model Run	Comparison Metric		
	A	γ	R
Simulation EAPE (MHO)	0.40	0.84	0.56
Reanalysis EAPE (MHO)	0.55	0.84	0.84
Simulation EAPE (Argo)	0.91	1.30	0.47
Reanalysis EAPE (Argo)	1.07	1.30	0.62

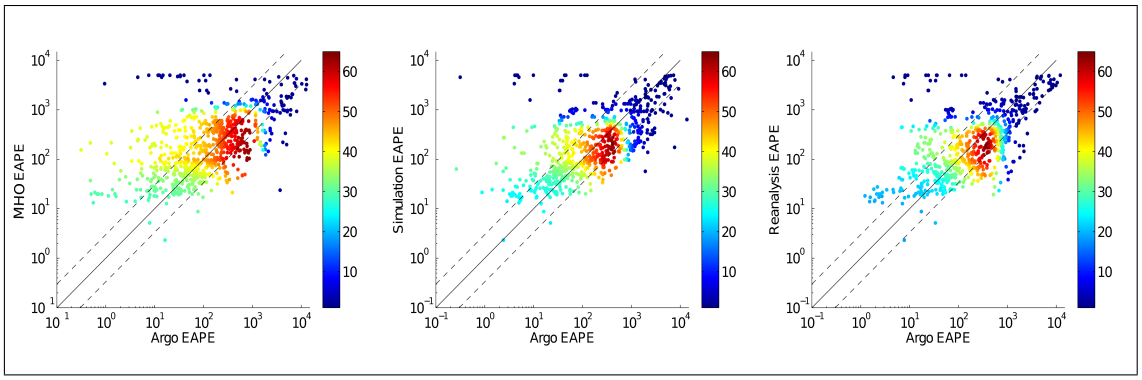

Figure 2.13: As in Figure 2.4, but for a point-to-point comparison EAPE ($log_{10}(\mathrm{cm}^2 s^{-2})$) in (left) reanalysis, (middle) simulation, and (right) MHO, versus Argo EAPE (*Roullet et al.*, 2014) at MHO locations. Reprinted from *Luecke et al.* (2017).

2.4 Estimates of Inherent Scatter in Eddy Statistics

Mesoscale eddies are, by their nature, chaotic. In model-data comparisons such as the ones presented in this chapter, the question arises as to how much of the "scatter" seen in the model-data scatterplots is due simply to the unpredictable nature of the underlying EAPE fluctuations. HYCOM and other realistic-domain high-resolution ocean models exhibit dynamical variability due to complex and varying topography, atmospheric forcing, and horizontal inhomogeneities arising from basin geometries. The scatter plots in Figures 2.4, 2.9, 2.11, and 2.13 are made from model output and observations that are impacted by all of these factors. However, some of the scatter is due simply to the fact that we are sampling a chaotic field, in both model output and observations, irrespective of the complexities introduced by the horizontally inhomogeneous factors described above.

Estimates of the temporal sampling requirements for chaotic systems have been previously made, giving predictions for the degree of spread expected in the variance

of temperature time-series data of a given length. *Flierl and McWilliams* (1977) estimate the error in temperature variance (a quantity proportional to EAPE assuming a given buoyancy frequency) to be on the order of 20-30% for records of 700 days in length, and 10% or lower only for records longer than 15 years. Because many of the MHO records used in this data are on the order of a year in length, and because the MHO, HYCOM, and Argo EAPE estimates used here are not contemporaneous, we expect a substantial amount of spread in even the best model-data comparisons.

To illustrate the intrinsic spread expected in our model-data comparison, we compare EAPE between different grid points in a simulation of an idealized model that is horizontally homogeneous. As our idealized model is horizontally homogeneous, the confounding spatially varying factors mentioned above –topography, atmospheric forcing, and basin geometry– are not present. The idealized model is quasi-geostrophic (QG), containing two vertical layers on an f-plane domain. The forcing for the QG model consists of a horizontally homogeneous mean flow that is vertically sheared to induce baroclinic instability. The model is damped by linear bottom Ekman friction with a decay coefficient R_2. The nondimensional bottom friction strength parameter is $\kappa = [\frac{R_2 L_d}{\overline{u_1}-\overline{u_2}}]$, where L_d is the first baroclinic mode Rossby radius of deformation, overbars denote an imposed time mean, and $\overline{u_1} - \overline{u_2}$ is the difference in the imposed (zonal) mean flow in the upper (1) and lower (2) layers. The value of κ in the simulation used here is 0.4. Snapshots of the model output are saved at every unit of non-dimensional time $[\frac{L_d}{\overline{u_1}-\overline{u_2}}]$. The correlation time is about 16.5 snapshots. Further details about the simulation used here can be found in *Arbic et al.* (2012a, 2014) and references therein. Because we are using the QG simulation as an analogue for the mid-latitude mesoscale eddy field, we equate the 16.5 snapshot correlation time for the simulation with 40 days, a typical correlation time for mid-latitude mesoscale eddies (*Kuragano and Kamachi*, 2000; *Jacobs et al.*, 2001). EAPE in the QG model

is given by:

$$EAPE = \frac{1}{2}\frac{\psi_{bc}^2}{L_d^2} = \frac{1}{2}\frac{\delta(\psi_1 - \psi_2)^2}{(1+\delta)^2 L_d^2}, \tag{2.6}$$

where ψ_{bc} is the baroclinic streamfunction, ψ_1 and ψ_2 are the upper and lower layer streamfunctions, and δ is the ratio between the top and bottom layer thickness. In the simulation used here, $\delta = 0.2$.

Because our HYCOM-MHO comparisons involved about 1100 instruments, we compare EAPE at 1100 randomly selected unique locations in the QG model versus EAPE at 1100 different randomly selected locations. EAPE is averaged over 8 and 182 model correlation time periods (approximately equivalent to 320 days and 20 years for mid-latitude oceanic eddies respectively). As predicted by *Flierl and McWilliams* (1977), the longer period of time averaging dramatically reduces the scatter between the point to point comparisons as seen in the difference between Figures 2.14a and 2.14b.

We are able to validate our QG model runs against the quantitative predictions *Flierl and McWilliams* (1977) make on the amount of error expected in temperature variance for various record durations. To make these comparisons, we use the QG analogue of T', the temperature anomaly. It can be shown using the thermal wind relation that the temperature anomaly $T' \propto (\psi_1 - \psi_2)$. The temporal variance of T' is then calculated for several different lengths of time. We use 100, 320, and 700 days, which correspond to temporal-averaging lengths assessed in *Flierl and McWilliams* (1977). In order to quantify statistical errors in temperature variance in the model, we calculate the ratio of the standard deviation of the time-mean temperature variance computed over all 1100 points, to the magnitude of the time-mean temperature variance averaged over the same model grid points. For 100, 320, and 700 days of sampling time, we estimate the temperature variance error to be 63%, 36%, and 23% respectively, which agree well with the 60%, 40%, and 20% estimates made by *Flierl and McWilliams* (1977). Additionally it takes 12 years of time averaging for our

QG temperature variance error to drop below 10%, which lies fairly close to the 15 years predicted by *Flierl and McWilliams* (1977). This result suggests that given the duration of sampling common in the MHO records, an order 30-40% error in EAPE estimates is to be expected. It is reasonable then, that the discrepancies in EAPE estimates displayed in Table (2.1) fall roughly within this range. The large error in temperature variance due to the chaotic nature of mesoscale eddies must certainly account for some of the spread seen in the scatterplots of T'^2 and EAPE shown in Figures 2.4, 2.9, 2.11, and 2.13.

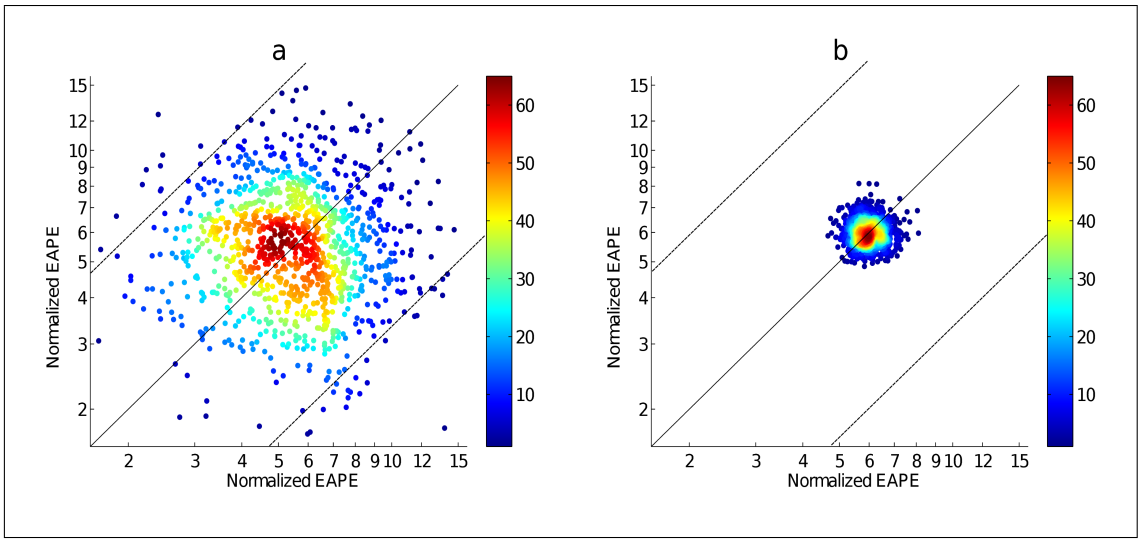

Figure 2.14: Scatterplots of EAPE taken from 1100 random points in an idealized horizontally homogeneous QG turbulence model verses EAPE taken from 1100 different random points within the same QG model, used to illustrate of the effect of record duration on scatter. The QG EAPE [normalized by $\frac{1}{2}(\overline{u_1} - \overline{u_2})^2$] is averaged over 8 model decorrelation time periods in (a), and over 182 model decorrelation time periods in (b) (approximately equivalent to 320 days and 20 years for mid-latitude oceanic eddies respectively.) As in previous plots, bounding lines represent a factor of 3, and colorbars represent population density. Reprinted from *Luecke et al.* (2017).

2.5 Conclusions

In this chapter, we have assessed the ability of both a simulation and reanalysis of a three-dimensional global ocean model (HYCOM) to reproduce the statistics of the low-frequency eddy available potential energy (EAPE) field in global maps made from Argo floats (*Roullet et al.*, 2014) and in local moored historical observations

(MHO). EAPE plays an important role in the vertical structure and mixing in the ocean, as well as in the overall oceanic energy budget. It is therefore essential that high-resolution ocean models, which are increasingly being used for ocean forecasting and dynamical process studies, be evaluated for the accuracy of their EAPE fields. As far as we know, this study is the first to compare, on a global scale, the EAPE fields in high-resolution ocean models with EAPE fields computed from observations.

Both the HYCOM simulation and reanalysis predict global area averaged EAPE estimates that are within 10% of Argo global estimates. At MHO locations, the spatially averaged EAPE falls within 16% of MHO estimates, and within 30% of Argo estimates. At the MHO locations, both the highest EAPE estimate (MHO) and lowest estimate (Argo) only differ about 50%, and effectively bound the estimates from the models. Both model EAPE estimates fall within the error of our observations. If account is taken of the fact that Argo estimates include aliased high-frequency motions, then the Argo EAPE values spatially averaged over the MHO locations are lower than the model estimates by about 50%, and in the globally averaged EAPE estimates made from maps, Argo becomes lower than the model estimates by 30%.

Point-to-point comparisons of Argo, simulation, reanalysis and MHO EAPE at MHO locations exhibit considerable scatter. However we show improvement in the local point-to-point correlation of EAPE from the simulation to the reanalysis. As we have shown in an idealized quasi-geostrophic model, and as discussed in *Flierl and McWilliams* (1977), some amount of scatter is to be expected given the chaotic nature of the mesoscale eddies underlying the EAPE fields. While both the HYCOM simulation and reanalysis stratification profiles agree reasonably well with climatological estimates, it is clear that the reanalysis stratification stays closer to climatology, and exhibits less temporal drift than does the simulation stratification. Data assimilation in the reanalysis also improves the spatial structure of the global EAPE with respect to the Argo maps. We show using the skill score that in both our Argo and MHO

comparisons, model perfomance (EAPE and T'^2 respectively) is increased through data assimilation. The results presented in this chapter show that HYCOM recreates the global low-frequency EAPE field reasonably well. This suggests that it would be reasonable to use HYCOM to quantify global– and basin–scale EAPE reservoirs.

CHAPTER III

From Internal Gravity Waves to Mesoscale Eddies: Temperature Variance and Kinetic Energy in Global Models and Historical Observations

3.1 Introduction

In this chapter, we examine the ability of high-resolution global ocean models to recreate an accurate temperature variance and kinetic energy spectrum ranging from mesoscale eddies (periods of 30-200 days) through high-frequency (supertidal) internal gravity wave continuum.

In recent years, global ocean models have been run at higher spatial and temporal resolutions. Increased computer power has led to high-resolution, three-dimensional ocean models that are able to simulate mesoscale eddies on a global scale (e.g., *Hecht and Hasumi*, 2008; *Chassignet et al.*, 2009). The HYbrid Coordinate Ocean Model (HYCOM) and Massachusetts Institute of Technology general circulation model (MITgcm) simulations examined here models now include both astronomical tidal forcing and realistic atmospheric forcing. High-frequency atmospheric forcing generates near-inertial waves (*Silverthorne and Toole*, 2009; *Simmons and Alford*, 2012), and barotropic tidal flow over topographic features creates internal tides (e.g., *Garrett and Kunze*, 2007). In models with sufficient horizontal and vertical resolution, nonlinear

wave-wave interactions fill out the oceanic internal gravity wave continuum.

Resolving a spectrum of internal gravity waves (hereafter, often referred to simply as"internal waves", or IGWs) represents a new paradigm for global ocean models. Because internal waves redistribute large amounts of energy over long distances, the realism of the modeled internal wave spectrum is essential for our understanding and simulation of the three-dimensional geography of mixing that is in turn important for large-scale ocean dynamics (*Munk and Wunsch*, 1998; *Kunze*, 2017). Tidal and atmospheric forcing were first added to a high-resolution general circulation model in HYCOM (*Arbic et al.*, 2012b, 2010), and the HYCOM tidal simulations were shown to have an internal gravity wave spectrum (*Müller et al.*, 2015; *Savage et al.*, 2017a,b). Later, MITgcm simulations were run with higher resolution and were also shown to have an IGW spectrum (*Rocha et al.*, 2016a,b; *Savage et al.*, 2017b). An overview of global internal tide and wave modeling in HYCOM and MITgcm is given in *Arbic et al.* (2018).

High-resolution ocean model simulations have been compared with observations in a number of studies. For instance, low-frequency sea surface height (SSH) variance in high-resolution models has been compared with altimeter results in several studies such as *Maltrud and McClean* (2005); *Chassignet and Xu* (2017), amongst others. Comparisons of low-frequency kinetic energy in high-resolution models with mooring, surface drifter, and altimeter observations have been done in several studies (e.g., *Maltrud and McClean*, 2005; *Penduff et al.*, 2006; *Scott et al.*, 2010; *Thoppil et al.*, 2011). Low-frequency eddy available potential energy in non-tidal HYCOM simulations was compared to mooring and Argo float observations in (*Luecke et al.*, 2017).

A number of model-data comparisons have been performed with the HYCOM and (to a lesser extent) MITgcm tidal simulations. However these comparisons often focus on a specific frequency band, or a particular geographic location, or both. For

example, barotropic and internal tide sea surface height signatures in HYCOM have been compared with altimetry (*Shriver et al.*, 2012; *Stammer et al.*, 2014; *Ansong et al.*, 2015; *Ngodock et al.*, 2016). HYCOM tidal kinetic energy and internal tide energy fluxes have been compared with in-situ observations in *Timko et al.* (2012, 2013) and *Ansong et al.* (2017) respectively. In *Buijsman et al.* (2016) the semidiurnal internal tide dissipation rates are compared with Argo inferred dissipation rates. *Savage et al.* (2017b) compares the dynamic height variance in both HYCOM and MITgcm to the variance computed from moored McLane profiler data, across a wide range of frequencies. The McLane profilers (*Doherty et al.*, 1999) used in *Savage et al.* (2017b) were set up to study internal gravity waves, and have high vertical and temporal resolution, However *Savage et al.* (2017b) found only 9 such records that were useful for comparing with models in the open-ocean. *Rocha et al.* (2016a) compared kinetic energy wavenumber spectra in the MITgcm with along-track Acoustic Doppler Current Profiler data in one Southern Ocean location.

In this study, we compare three simulations of MITgcm and two simulations of HYCOM to moored historical observations of temperature variance and kinetic energy. By integrating over different frequency bands, we test the ability of these simulations to model motions ranging from mesoscale eddies to the internal gravity wave continuum. Our study is quasi-global, in that thousands of records, distributed over the major ocean basins, are used. Our study builds upon our model-data comparison of low-frequency eddy available potential energy, in *Luecke et al.* (2017), to examine temperature variance over a wider range of frequencies. Both the HYCOM and MITgcm simulations are performed at different resolutions, thus allowing us to study the impact of resolution on model-data comparisons. Additionally, we compare geostrophic eddy kinetic energy from both MITgcm and HYCOM to values computed from the AVISO satellite altimeter database. Our study is unique in being a quasi-global comparison of models and in-situ data, across five simulations of varying

resolutions performed with two different models, of both temperature variance and kinetic energy, across a range of frequencies running from the mesoscale eddy band to the internal gravity wave continuum.

3.2 Models, Observations, and Methods

We use temperature variance and kinetic energy spectra from HYCOM simulations of two resolutions (1/12.5° and 1/25°), and MITgcm simulations of of three resolutions (1/12°,1/24°, and 1/48°). More general information about HYCOM can be found in *Chassignet et al.* (2009), and more general information about MITgcm can be found in *Marshall et al.* (1997). Temperature variance and kinetic energy spectra computed from the models are compared to spectra calculated from a database of moored historical observations (MHO) obtained from the Global Multi-Archive Current Meter Database [GMACMD; *Wright et al.* (2014)]. For our comparison of geostrophic eddy kinetic energy from AVISO, we use the methodology and data from Figure (1) of *Qiu et al.* (2018). We use the global SSH anomaly dataset created by Ssalto/Duacs and distributed by AVISO with support from CNES (`http://marine.copernicus.eu/`). This dataset has a 7-day temporal resolution and a 0.25 degree spatial resolution obtained through the spatial-temporal interpolation of altemetric data (*Ducet et al.*, 2000).

3.2.1 Moored Historical Observations

Time-series of temperature and velocity from moored historical observations (MHO) are obtained from the GMACMD can be found at `http://stockage.univ-brest.fr/~scott/GMACMD/gmacmd.html`. These records span from 1974 to 2008, and are not contemporaneous with the model runs.

Only locations with seafloor depths greater than 500 meters are included. We select MHO time-series that are longer than 90 days, and exclude records containing

gaps in the time-series. The remaining temperature and velocity records are then visually inspected and quality controlled for instrument errors and other problems such as severe discretization. The total number of instruments excluded for these reasons is relatively small ($< 10\%$). Our selection criteria yields a total of 3,096 instrumental records of temperature and 3,133 instrumental records of velocity, some of which are co-located and some of which are not, distributed around the global ocean. The geographical locations are shown in Figure 3.1. The spatial coverage of both temperature and velocity is sparse and uneven, with some basins such as the North Atlantic and North Pacific being much better instrumented than others. The bottom panel of Figure 3.1 shows the distribution of instruments by depth for velocity (right) and temperature (left) records. There is a clear bias for measurements in the upper 1000m.

3.2.2 HYCOM

Two simulations of HYCOM are used in this comparison. HYCOM12, with a 1/12.5 degree horizontal resolution, and HYCOM 25, with a 1/25 degree horizontal resolution. The spatial scales of the model grids are approximately 8km and 4km at the equator respectively. The HYCOM output is saved hourly, and HYCOM12 output spans October 1, 2011 through April 1, 2012, while HYCOM25 output spans January 2014 through December 2014. Both simulations contain 41 hybrid layers in the vertical. Atmospheric fields used in both HYCOM simulations, such as pressure, buoyancy, and wind forcing, are taken from the U.S. Navy Global Environmental Model, NAVGEM (*Hogan et al.*, 2014). HYCOM12 is forced by NAVGEM on three hour intervals, while HYCOM25 is forced hourly. The HYCOM simulations are forced using a 0.5° application grid interpolated from the NAVGEM primary 37 km grid.

The HYCOM simulations are additionally forced by the astronomical tidal potential of the two largest diurnal constituents (K_1 and O_1) along with the three largest

semidiurnal constituents (M_2, S_2, and N_2) (*Cartwright*, 1999). These five tidal constituents account for 97 percent of the global variance in the 10 largest tidal constituents in the Global Ocean Tide Model (GOT99.2; *Ray*, 1999). The self-attraction and loading (SAL) (*Hendershott*, 1972) term is taken from the TPXO model of *Egbert et al.* (1994) and and *Egbert and Erofeeva* (2002). An Augmented State Ensemble Kalman Filter is implemented in both simulations to reduce the global RMS error of M_2 barotropic tidal elevations in waters deeper than 1 km, with respect to TPXO, to approximately 2.6 cm (*Ngodock et al.*, 2016).

A Smagorinsky scheme is employed for horizontal viscosity and a Laplacian scheme is utilized for horizontal diffusivity, while a KPP scheme (*Large et al.*, 1994) is used for both vertical diffusivity and viscosity. The topographic wave drag field taken from *Jayne and St. Laurent* (2001) is tuned to minimize barotropic tidal errors with respect to the altimeter-constrained tide model TPXO (*Egbert et al.*, 1994; *Egbert and Erofeeva*, 2002). The wave drag tuning computed for HYCOM25 was half the of what was used in HYCOM12. A description of the wave drag tuning can be found in *Buijsman et al.* (2015), and more information on the importance of the wave drag on barotropic and baroclinic tides can be found in *Ansong et al.* (2015) and *Buijsman et al.* (2016).

3.2.3 MITgcm

Three global ocean simulations of MITgcm (*Marshall et al.*, 1997) are used in this comparison: MITgcm 1/12 degree , MITgcm 1/24 degree, and MITgcm 1/48 degree referenced to as MITgcm12, MITgcm24, and MITgcm48 respectively. All three MITgcm simulations have 90 z-levels in the vertical, with level thicknesses varying from 1 m at the surface to 480 m near the bottom at the maximum model depth of 7 km. Bathymetry is taken from the *Smith and Sandwell* (1997) Version 14.1 and IBCAO Version 2.23 *Jakobsson et al.* (2008). MITgcm is forced at the surface

with atmospheric fields from the 0.14° European Center for Medium-Range Weather Forecasts (ECMWF) atmospheric operational model analysis at six-hour intervals. Starting in 2011, atmospheric forcing is converted to surface fluxes using the bulk formulae of *Large and Yeager* (2004). In regions of ice coverage, ocean surface fluxes are computed using the sea ice model of *Losch et al.* (2010).

The model includes atmospheric pressure forcing and tidal forcing for 16 tidal constituents, the latter applied to MITgcm as additional atmospheric pressure forcing (*Ponte et al.*, 2015). The MITgcm runs employ the full luni-solar tidal potential of *Weis et al.* (2008).

A Leith scheme is used for horizontal diffusivity and a KPP scheme is used for vertical diffusivity. The MITgcm12 simulation is initialized on 1 January 2010 from a data-constrained 1/6° simulation provided by the Estimating the Circulation and Climate of the Ocean, Phase II project (ECCO2) (*Menemenlis et al.*, 2008) and integrated for 1 year without tides with ERA-Interim (*Dee et al.*, 2011) surface boundary conditions. Tidal forcing and atmospheric boundary conditions from the 0.14° ECMWF analysis are applied starting on 1 January 2011. The MITgcm24 simulation is initialized from MITgcm12 fields on 17 January 2011. The MITgcm48 simulation is initialized from MITgcm24 fields on 10 September 2011.

We use $\sim$ 7 months of hourly model output from the three MITgcm simulations for the following periods: 1 January 2012 through 20 July 2012 for MITgcm12, 2 October 2012 through 22 April 2013 for MITgcm24, and 28 January 2012 through 22 August 2012 for MITgcm48. The MITgcm records are only 7 months long due to the fact that that, at the time we extracted the model output it had only been run for this long (after a suitable spinup period).

3.2.4 Methods

In order to compute frequency spectra, a linear trend and mean are removed from each time t series of temperature $T(t)$, zonal velocity $U(t)$ and meridional velocity $V(t)$. Each detrended time series is multiplied by a Tukey window with a ratio of 0.2. Approximately 10-15 percent of the total variance is lost as a result of the Tukey window.

The frequency spectra are computed from each time series for each MHO instrument, and the corresponding nearest neighbor model grid point is interpolated to the depth of the MHO instrument. A discrete Fourier Transform is defined as:

$$\widehat{Field(\omega)} = \sum_{t=0}^{N-1} Field(t) e^{-i\omega t}, \tag{3.1}$$

where Field denotes either temperature or velocity component, ω denotes frequency, t denotes time, and N denotes the total number of sample points. In the case of temperature, variance is calculated as

$$\text{Temperature variance} = \frac{2\delta t}{N} \int_{\omega_{min}}^{\omega_{max}} |\widehat{T(\omega)}|^2 d\omega \tag{3.2}$$

and for kinetic energy,

$$\text{KE} = \frac{\delta t}{N} \int_{\omega_{min}}^{\omega_{max}} |(\widehat{U(\omega)})^2 + (\widehat{V(\omega)})^2| d\omega, \tag{3.3}$$

where KE denotes kinetic energy, dt is the temporal sampling interval, and ω_{min} and ω_{max} represent the lower and upper bounds of the frequency band of interest. We integrate over five bands, supertidal (12-2.06 cpd), semidiurnal (2.05-1.86 cpd), diurnal (1.05-0.87 cpd), subtidal (0.7-0.1 cpd) and mesoscale (0.09-0.01 cpd). In the case of the MHO records shorter than 100 days in length, the mesoscale band is integrated to the lowest possible frequency. Additionally, for kinetic energy, we

integrate over the near-inertial band defined as $0.9-1.1f$, where f is the local Coriolis frequency. This represents a 'double counting' of variance in regions where f and the diurnal tides overlap.

We employ several statistical metrics to quantify differences between temperature variance and kinetic energy in the models and observations. A linear regression coefficient, A for both temperature variance and kinetic energy is calculated using standard methods. A ratio γ between the mean of the model variances and the mean of the observational variances is defined as:

$$\gamma = \frac{\sum_{i=1}^{n} Variance_{model}}{\sum_{i=1}^{n} Variance_{observed}}, \tag{3.4}$$

where i is a location index and n is the total number of instruments used in the calculation. Finally, a Spearman correlation coefficient r_s is calculated between model and data variance across the MHO locations.

In order to calculate our AVISO-derived eddy kinetic energy (EKE) values, we average the modeled SSH data into a weekly time series on a 0.25 degree longitude Mercator grid and compute the EKE from the geostrophic velocity field as in *Qiu et al.* (2018) where:

$$u = -\frac{g}{f}\frac{\partial \eta}{\partial y}, \quad \text{and} \quad v = \frac{g}{f}\frac{\partial \eta}{\partial x}, \tag{3.5}$$

where g is the local acceleration due to gravity, f is the coriolus frequency, and x and y are the zonal and meridional spatial coordinates, which gives the geostrophic velocities for u and v respectively, and EKE $= \frac{1}{2}(u^2 + v^2)$.

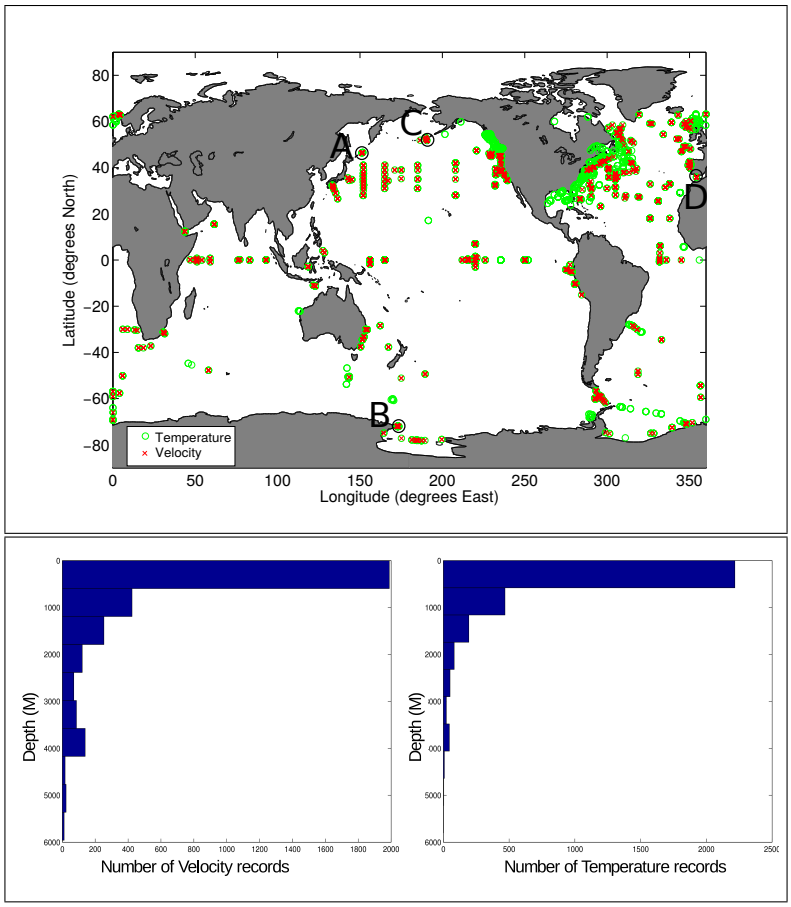

Figure 3.1: Geographical locations of MHO records in the comparison. Temperature observations are shown in green circles, while velocity observations are denoted by red X's. The bottom panels show the depth distribution for velocity(left) and temperature (right) instrument record locations. The labels "A", "B", "C", and "D" will be referred to later in the text.

3.3 Results

In this section, we present our global model-data comparisons of temperature variance and kinetic energy. Results for both temperature variance and kinetic energy have been grouped into the six frequency bands defined above (supertidal, semi-diurnal, diurnal, near-inertial, subtidal, and mesoscale). Before we discuss the results in each frequency band, we present sample frequency spectra of the temperature

variance and kinetic energy at four individual locations in Figure 3.2. The left two panels in Figure 3.2 depict typical temperature variance spectra, while the right two panels show KE spectra. At supertidal frequencies, the highest resolution model (MITgcm48) clearly has more variance, and matches the observations more closely than the lower resolution models. The lowest resolution simulations (MITgcm12 and HYCOM12) have the least variance at supertidal frequencies. Also of note is a model deficiency in both KE (bottom right panel) and temperature variance (bottom left panel) that occurs in between 0.1 and 1 CPD. This lack of energy has been noted in other model-data comparisons, for instance in *Savage et al.* (2017b), and prompted our division of the low-frequency band into subtidal and mesoscale.

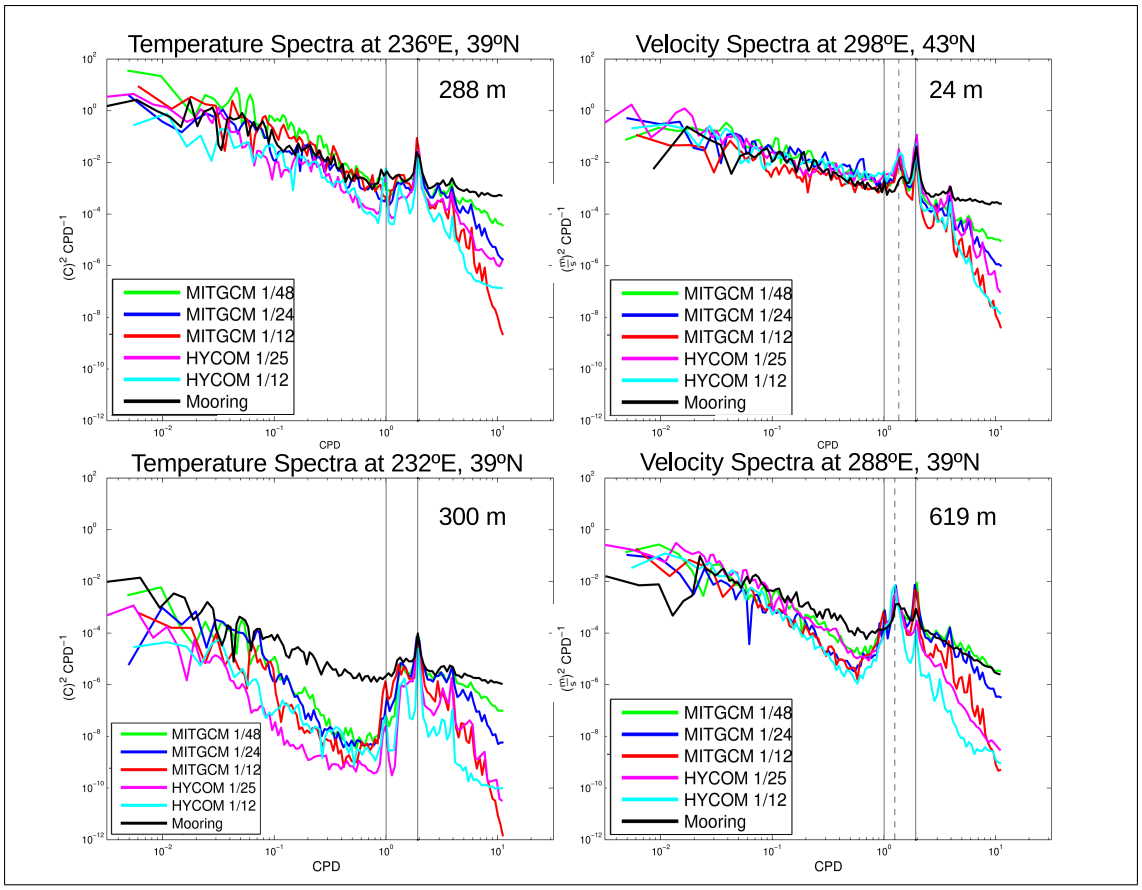

Figure 3.2: Sample spectra of temperature (Eastern Pacific) and velocity (Northeast Atlantic) for all 5 simulations. Instrument locations and depths are given in the subplots. The solid vertical lines show the diurnal (left) and semi-diurnal (right) tidal frequencies, and the dashed vertical line shows the local Coriolis frequency.

3.3.1 Supertidal Frequency Band

Figure 3.3 shows scatterplots of band-integrated MITgcm and HYCOM supertidal kinetic energy values against MHO values. Comparisons are shown for varying model resolutions at the MHO locations and depths given in Figure 3.1. For both MITgcm and HYCOM, increased model resolution yields increased KE. From visual inspection, HYCOM12 (bottom left) is biased lowest compared to MHO, while MITgcm48 (upper

right) , although still somewhat lower than observations, lies closest to the one-to-one line. The comparison metrics, which are given on each individual subplot of Figure 3.3 confirm this, as HYCOM12 has both the lowest ratio of the means, γ, and the smallest linear regression coefficient, , while MITgcm48 possess the highest. The correlation coefficients are slightly higher for HYCOM than for MITgcm, implying that the supertidal KE has a geographical distribution that is slightly more accurate in HYCOM than in MITgcm, even if the HYCOM values are generally too low. Within each model, subsequently higher resolution runs generally contain more KE variance.

There is a distinct group of points representing energies around ($10^{-1}\mathrm{m}^2 s^{-2}$) in the MHO data. This group of points has been enclosed with an ellipse in the HYCOM25 panel, and enclosed with a box in the MITgcm24 panel of Figure 3.3 for clarity, although the anomalous nature of the group is clearly visible in all five subplots of Figure 3.3. These instrument locations correspond to the circles labeled "A", "B", "C" and "D" in Figure 3.1. At these locations, MITgcm is systematically under-energetic, while HYCOM appears to do better in its representation of these near-shelf observations. It is important to note that while the overall relationships stated above do not change, the statistical metrics that we use do change upon removal of the "A", "B", "C" and "D" points. See the values with asterisks in the subplots of Figure 3.3. After the removal of these, correlation in HYCOM becomes slightly lower, while in MITgcm correlation becomes higher. Aditionally, the ratio of the means γ, and the linear regression coefficient, tend to get larger, showing the effect of these outliers on the statistical metrics.

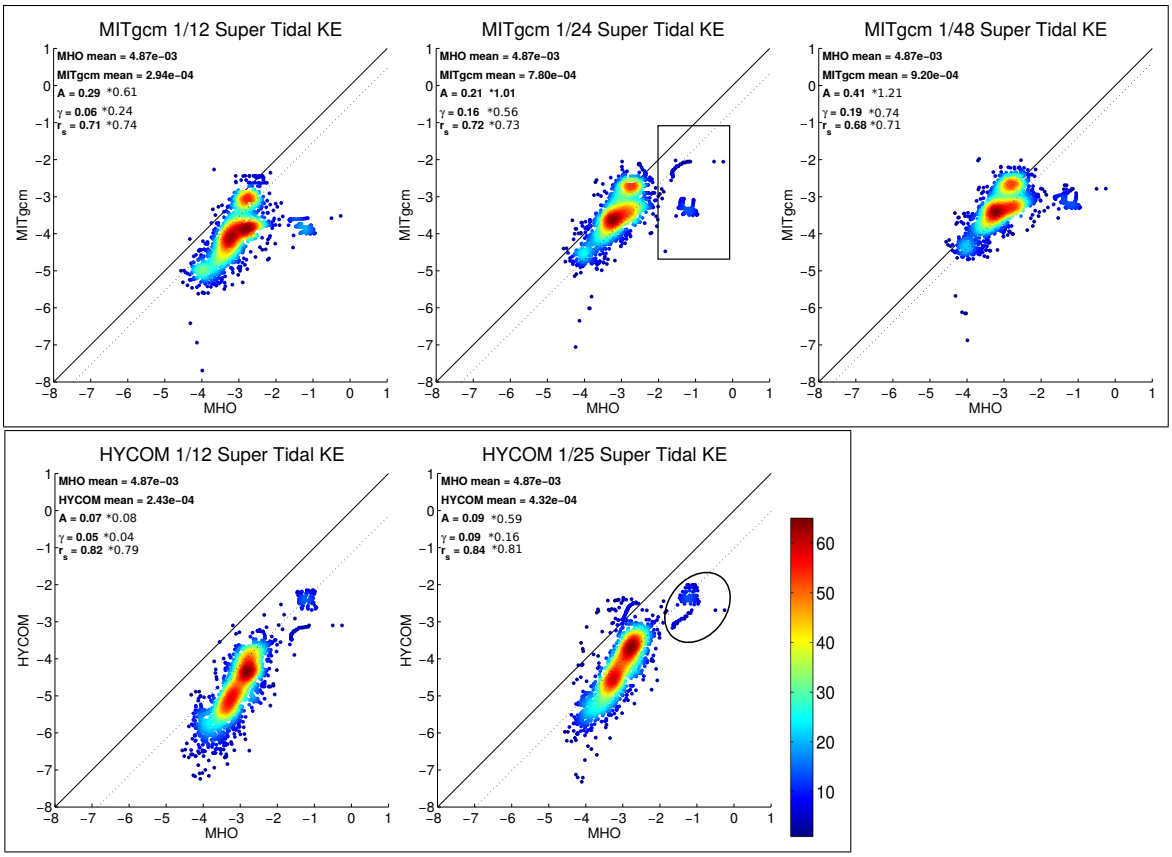

Figure 3.3: A point-to-point comparison of supertidal kinetic energy $[\log_{10}(\mathrm{m}^2 s^{-2})]$ between model and MHO. The top panel shows MITgcm12, MITgcm24, and MITgcm48, while the bottom panel shows HYCOM12 and HYCOM25. Population density is given by color, with the most tightly grouped data shown in red, and the sparsest data in blue. The one-to-one line is shown in solid black, and the linear regression A is shown as a dashed line. Statistical metrics between each model and the MHO data are printed on the upper left of each subplot. The A, γ, and r_s values with an asterisk are computed after the high-velocity values, enclosed by a box in the MITgcm24 subplot and an ellipse in the HYCOM25 subplot, have been removed.

As with KE, supertidal temperature variance shows improvement with model resolution in both HYCOM and MITgcm (Figure 3.4). As with KE, HYCOM12

(bottom left) is biased lowest compared to MHO,while MITgcm48 (upper right), although still somewhat lower than observations, lies closest to the one-to-one line. Again, the comparison metrics confirm this, as HYCOM12 has both the lowest ratio of the means, γ and the smallest linear regression coefficient,A, while MITgcm48 possesses the highest. In both MITgcm24 and MITgcm48, A values greater than 1 are a result of a small subset of locations where MITgcm greatly over-predicts the total supertidal temperature variance. The correlation coefficients r_s for supertidal temperature variance are higher in HYCOM than in MITgcm.

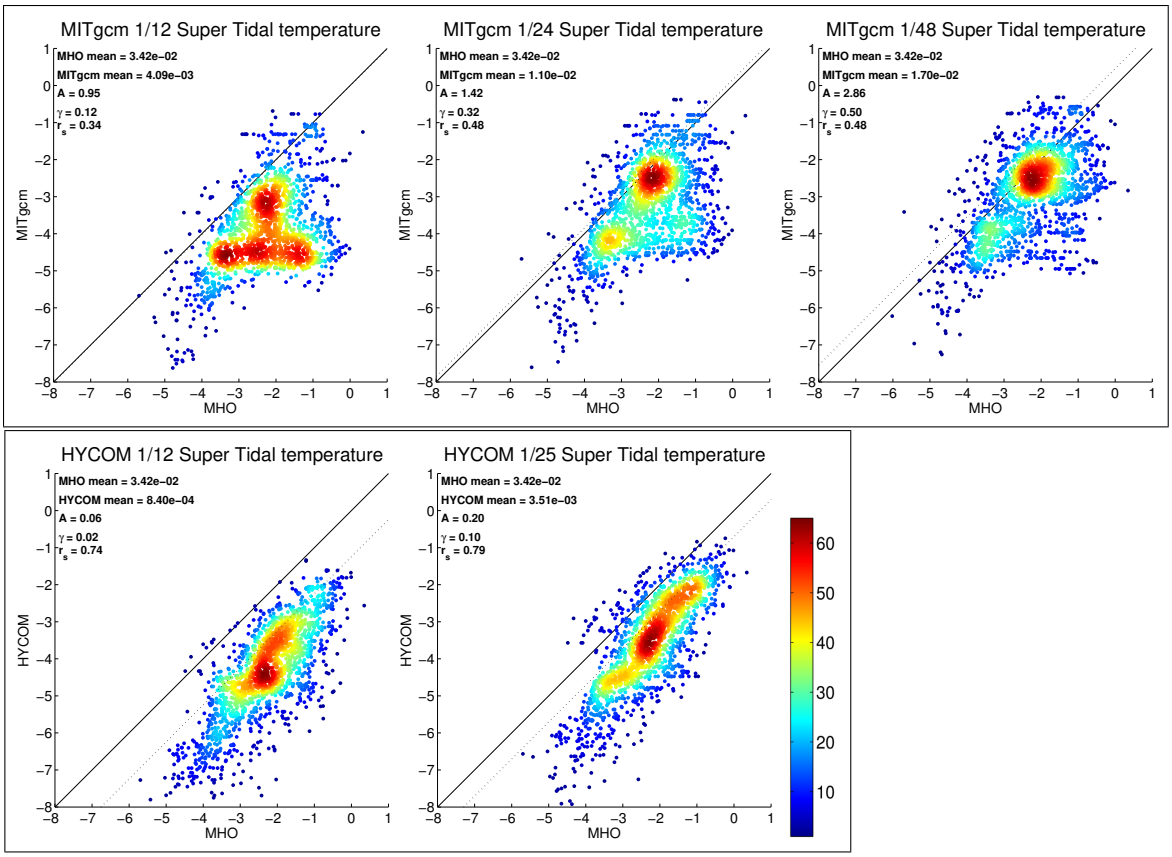

Figure 3.4: A point-to-point comparison of supertidal temperature variance [$\log_{10}(°C^2)$] between model and MHO. The top panel shows MITgcm12, MITgcm24, and MITgcm48, while the bottom panel shows HYCOM12 and HYCOM25. Population density is given by color, with the most tightly grouped data shown in red, and the sparsest data in blue. The one-to-one line is shown in solid black, and the linear regression A is shown as a dashed line. Statistical metrics between each model and the MHO data are printed on the upper left of each subplot.

3.3.2 Semi-Diurnal Band

Scatterplots of HYCOM and MITgcm semi-diurnal kinetic energy values against MHO values are shown in Figure 3.5 . From visual inspection, all three MITgcm runs appear to be biased high compared to the MHO values, except for a small number of

high-velocity points in the MHO, where MITgcm is biased much too low. HYCOM25 has both the highest ratio of the means and a linear regression coefficient closest to unity. In addition, the correlation coefficient r_s in HYCOM is higher than in MITgcm, reflecting the visual appearance of tighter correlations in HYCOM.

The high-velocity points, representing energies around ($10^{-1}\mathrm{m}^2 s^{-2}$) in the MHO data have been highlighted in the HYCOM25 and MITgcm24 panels of Figure 3.5 as was done in Figure 3.3. The high-velocity points are clearly visible in the model-data comparisons across all resolutions. These instrument locations correspond to the circle labeled "D" in Figure 3.1. At this location (in the Strait of Gibraltar), MITgcm is under-energetic for all three resolutions, while HYCOM lies much closer to observations. When these instruments are removed, the resulting A and γ values, denoted with asterisks in Figure 3.5, reveal an overall over-energetic bias in the great bulk of the MITgcm points. It is likely that the topographic wave drag employed in HYCOM plays in important role in damping HYCOM tidal KE to realistic levels. This would be consistent with discussions in *Ansong et al.* (2015), who showed that an extra damping, such as wave drag, is needed to make modeled internal tide SSH signatures agree with altimeter observations (see *Buijsman et al.* (2016) for related discussions on the impact of wave drag on tidal energetics). MITgcm does not employ a wave drag, which may explain its overly large KE outside of special regimes such as the Strait of Gibraltar. More analyses of the MITgcm results are currently underway in order to further test this hypothesis. The high sensitivity of the comparison metrics to outliers, particularly in the case of the linear regression coefficient A, illustrates some of the difficulties inherent in bulk model-data comparisons such as this.

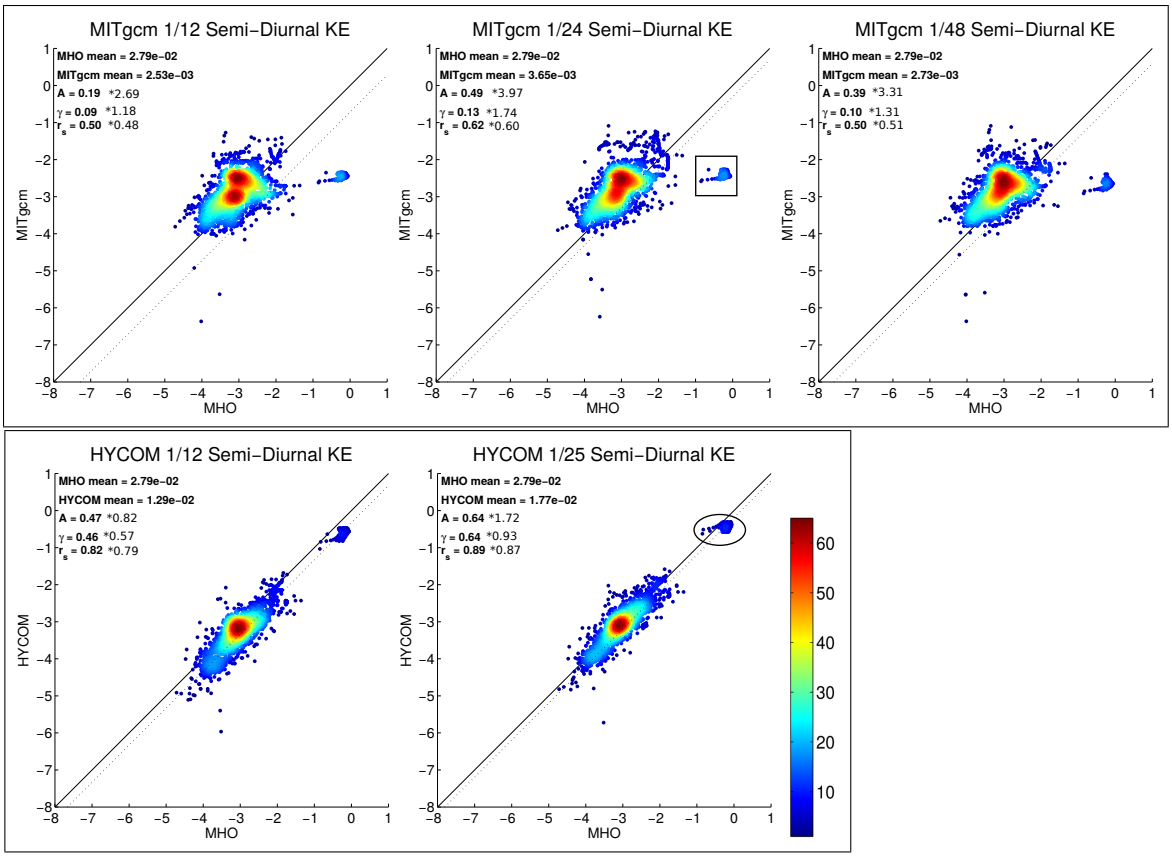

Figure 3.5: As in Figure 3.3 but for semi-diurnal KE.

Figure 3.6 shows scatterplots of HYCOM and MITgcm semi-diurnal temperature variance values against MHO values. Visually, there is more improvement between MITgcm12 and MITgcm24, with the values becoming more tightly clustered around the one-to-one line, than there is between MITgcm24 and MITgcm48. Both HYCOM12 and HYCOM25 display lower variance levels than their MITgcm counterparts, although HYCOM25 is nearly centered on the one-to-one line. The ratios of the means are closer to one for MITgcm than for HYCOM, but the linear regression values A suggest that MITgcm might be over-energetic for semidiurnal temperature variance as well, again suggesting that a lack of wave drag in MITgcm may lead to overly strong internal tides. As in all previous comparisons, the correlation coefficients r_s are higher in HYCOM than in MITgcm, reflecting the tighter correlations seen in the scatterplots.

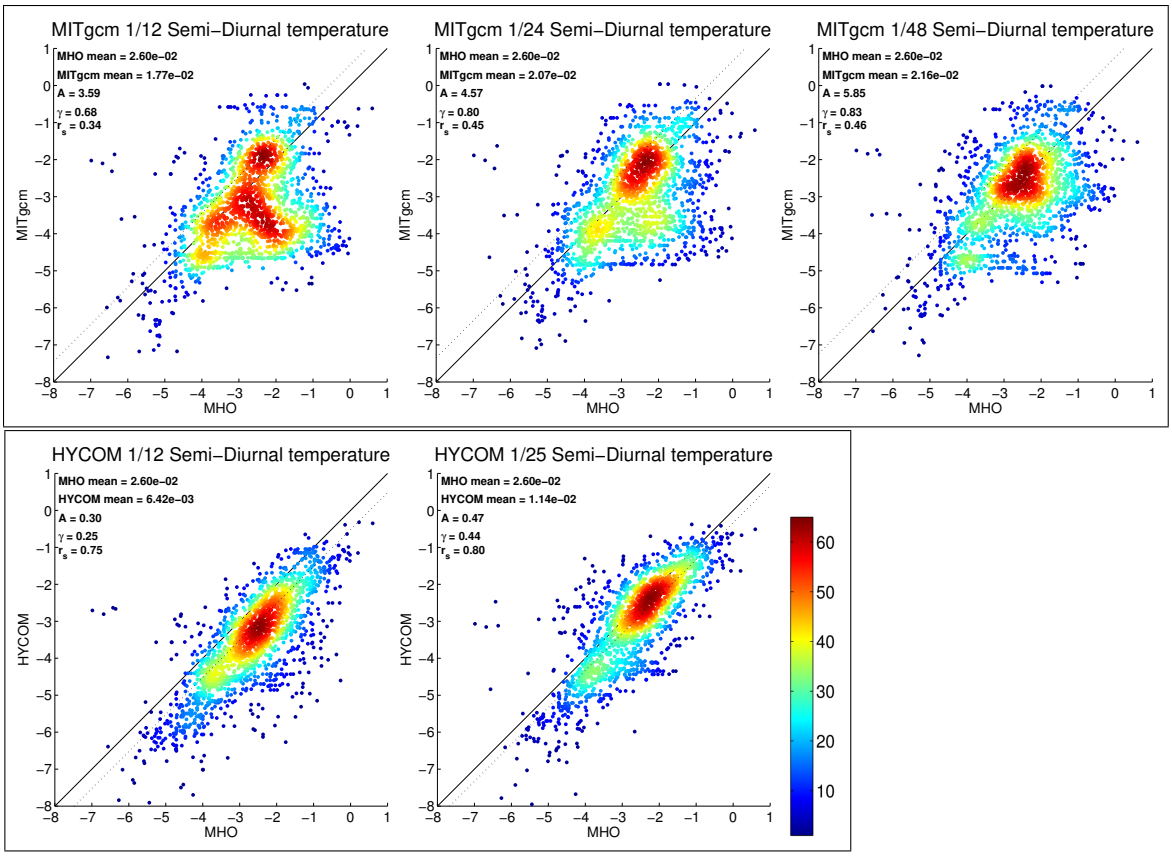

Figure 3.6: As in Figure 3.4 but for semi-diurnal temperature variance.

3.3.3 Diurnal Band

Figure 3.7 shows scatterplots of HYCOM and MITgcm diurnal KE values against MHO values. Interestingly, it appears as if MITgcm24 is better performing than both MITgcm12, and MITgcm48 , and this is supported by the "A", γ ,and r_s values. Because outliers tend to dominate the statistics, as discussed below, this result should be treated with some amount of skepticism. The majority of points visually display a similar amount of scatter in MITgcm and HYCOM here compared with earlier plots, although outliers for high-velocity MHO values are again more apparent in MITgcm. The HYCOM results suggest a slight weak bias for the great bulk of points, and we suggest that this may be due to over-damping of diurnal tides due to the fact that wave drag in HYCOM is optimally tuned for semidiurnal rather than diurnal tides,

as discussed in *Timko et al.* (2013); see also discussions in *Skiba et al.* (2013), a study focused solely on diurnal tides and optimally tuning wave drag for diurnal tides.

Again, there are several distinct group of points representing energies beyond ($10^{-2}\mathrm{m}^2 s^{-2}$) in the MHO data that are under energetic in MITgcm. The instrument locations correspond to the circles labeled "A", "B", "C", "D" , as well as instruments located in regions near coastal North West Atlantic, West Pacific,near Taiwan, East Pacific off the Californian coast, and the coastal Antarctic, in the Ross sea, and off the eastern extent of the Weddell sea. These locations, plus the locations labeled "A", "B", "C", "D" are contained in the large rectangle in the central top panel of Figure 3.7, and corresponding locations have been covered with a circle and an ellipse in the HYCOM25 subplot of Figure 3.7. At these locations, MITgcm is systematically under-energetic, while HYCOM appears to do better in its representation of these near-shelf observations. Additionally, there is a group of points representing energies beyond ($10^{-2}\mathrm{m}^2 s^{-2}$) in the MITgcm24 output (and analogous clusters in both MITgcm12 and MITgcm48). These locations are marked with a smaller rectangle in the central top panel of Figure 3.7. When the instruments enclosed in the rectangle are removed, the statistics change slightly for HYCOM12 and HYCOM25 and MITgcm24, while the changes are more pronounced for MITgcm12, and MITgcm48. This illustrates that even within a single model, outlier locations can vary between resolution. Removal of these locations also greatly normalizes the correlation between all 5 model runs.

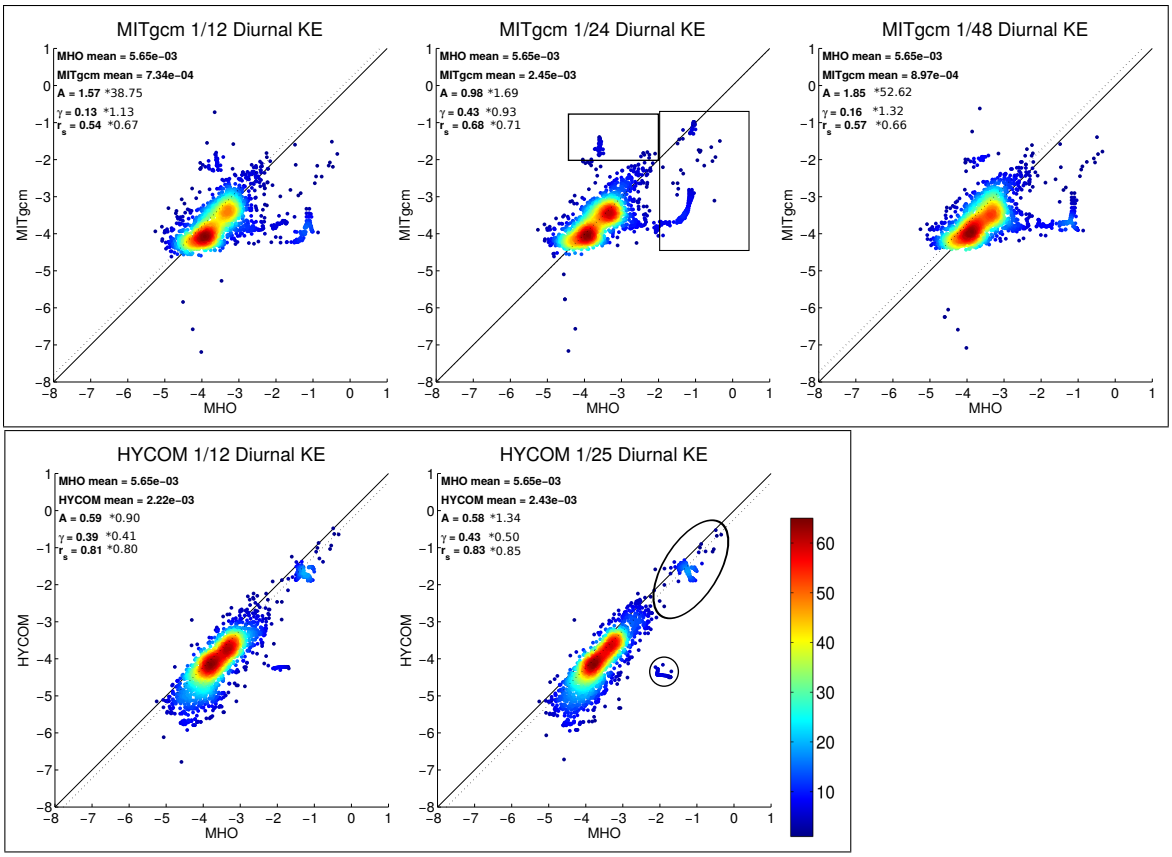

Figure 3.7: As in Figure 3.3 but for diurnal KE.

Figure 3.8 shows scatterplots of HYCOM and MITgcm diurnal temperature variance values against MHO values. Both HYCOM12 and HYCOM25 are weaker on average than MITgcm, as is seen in lower values of γ, and we suggest again that this may be due to over-damping of diurnal tides by the wave drag employed in HYCOM. MITgcm however has a linear regression A value greater than 1 in all three resolutions, possibly suggesting a need for wave drag or other additional damping in MITgcm. Once again, HYCOM has higher correlation values r_s than MITgcm.

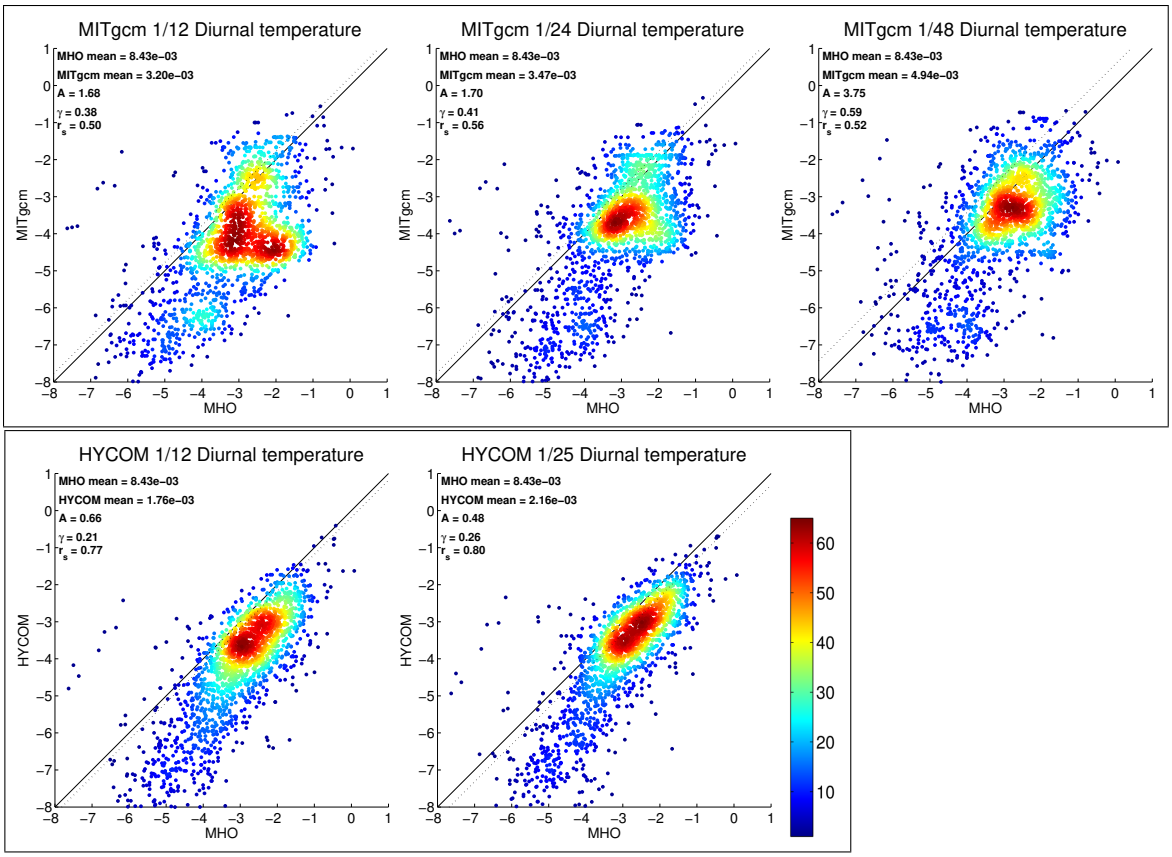

Figure 3.8: As in Figure 3.4 but for diurnal temperature variance.

3.3.4 Near-Inertial Band

As near-inertial motions do not have first order vertical motions, we do not compare temperature variances in the near-inertial band. Hence this section only compares modeled and MHO KE in the near-inertial band. Figure 3.9 shows scatterplots of HYCOM and MITgcm near-inertial KE values against MHO values as in Figure 3.3. The performance of MITgcm and HYCOM is fairly similar in this band as seen in all three metrics (A, γ, and r_s), and is also not greatly sensitive to resolution, consistent with the fairly large horizontal scales of near-inertial waves (e.g., *Simmons and Alford* (2012)).

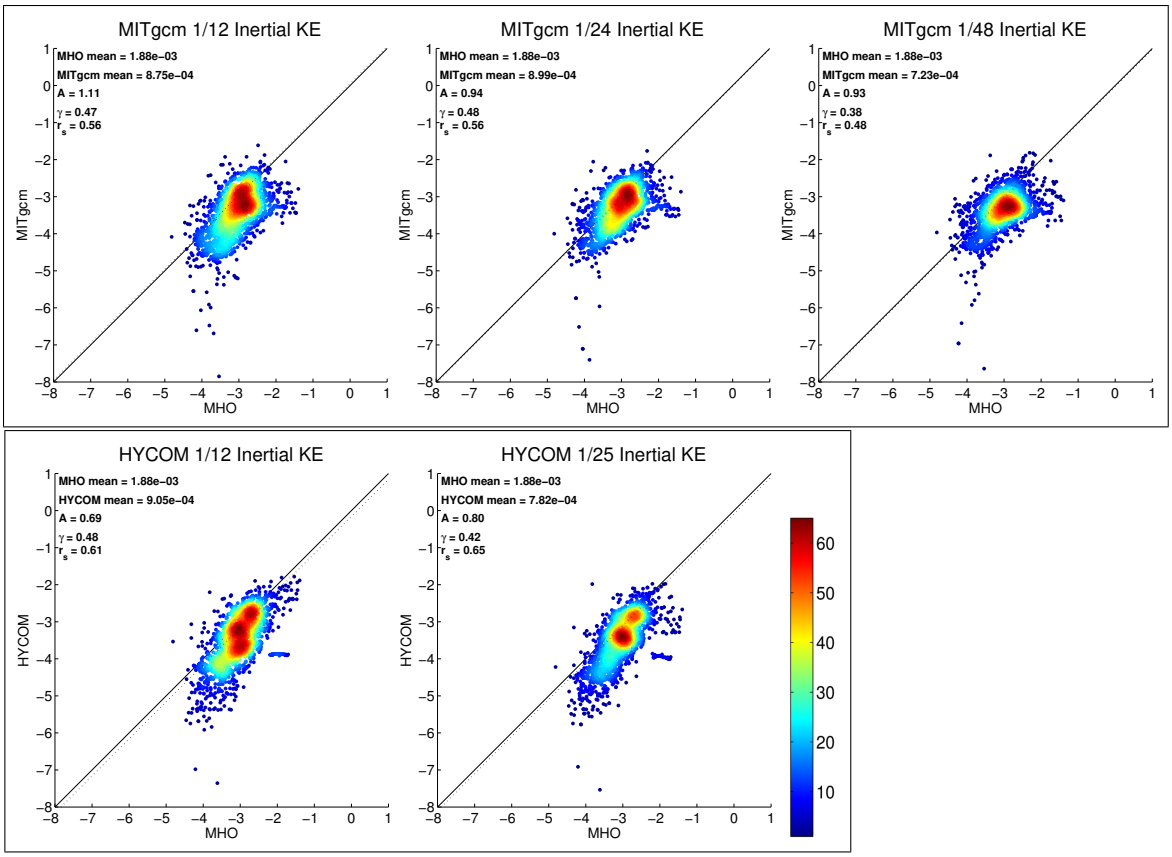

Figure 3.9: As in Figure 3.3 but for near-inertial KE.

3.3.5 Subtidal Frequency Band

The subtidal band covers periods from 0.7 cpd, a little over once per day, to once every 10 days, and is most likely to contain sub-mesoscale motions, which have shorter timescales than mesoscale motions (*Su et al.*, 2018). One might expect an increase in model resolution to enhance the dynamics within these time scales, as higher spatial resolutions precipitate frontal instabilities and other submesoscale motions. Figure 3.10 shows scatterplots of HYCOM and MITgcm subtidal kinetic energy values against MHO values. From visual inspection, both HYCOM12 and HYCOM25 are similar, with both runs being about a factor of 2 lower than the MHO mean ($\gamma = 0.46, 0.44$ and $A = 0.79, 0.57$ for HYCOM12 and HYCOM25 respectively). MITgcm however shows a steady increase in variance as resolution is

increased ($\gamma = 0.17, 0.41, 0.48$ and $A = 0.36, 0.59, 1.09$ for MITgcm12, MITgcm24, and MITgcm48 respectively). Although MITgcm48 has the highest variance, it is only slightly larger than the MITgcm24 and HYCOM variances. Thus we cannot conclude with any confidence that better resolution of the submesoscale is responsible for the changes seen with higher resolution in Figure 3.10. As in most other frequency bands, the HYCOM scatterplots have a tighter visual appearance, and accordingly, somewhat higher r_s values.

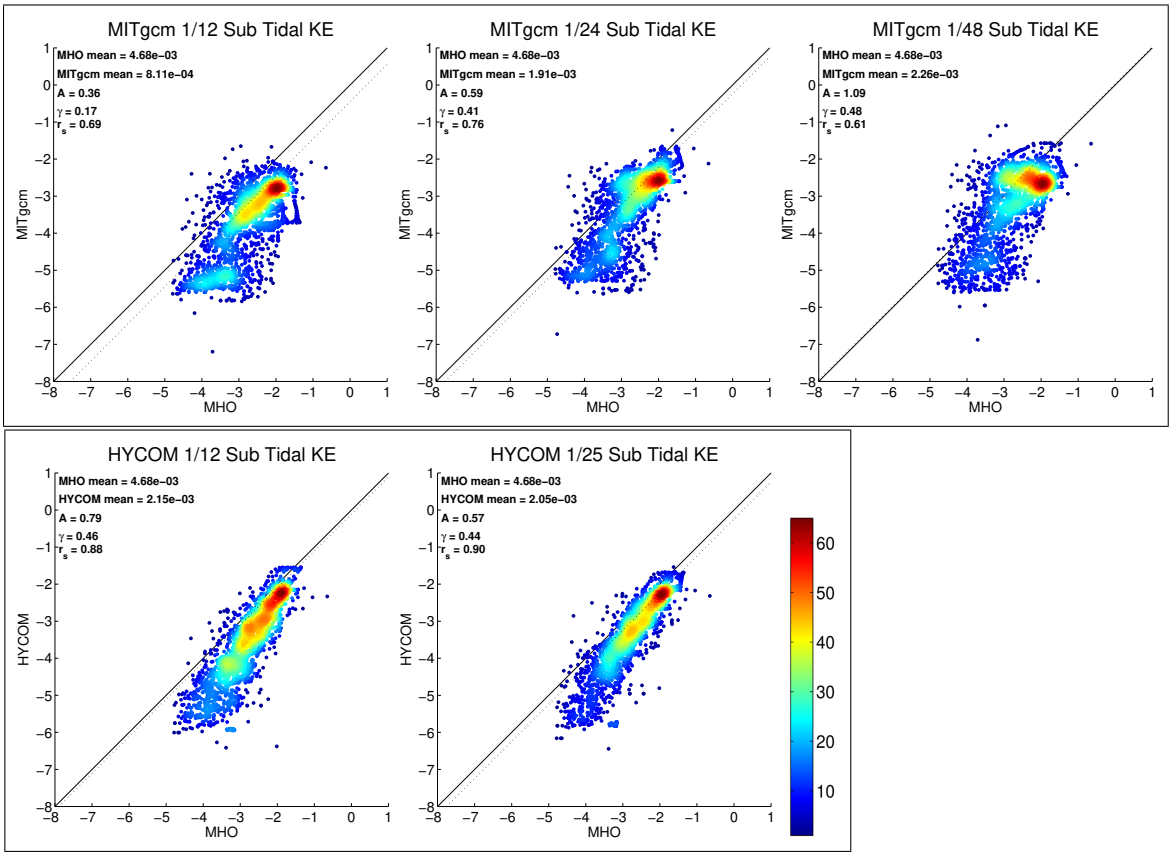

Figure 3.10: As in Figure 3.3 but for subtidal KE.

The subtidal temperature variance scatterplots are displayed in Figure 3.11. Visually, both HYCOM12 and HYCOM25 are similar, with both runs having lower means than the MHO. However, there is marked improvement in some statistics with $\gamma = 0.17, 0.35$ and $A = 0.21, 0.58$ for HYCOM12 and HYCOM25 respec-

tively. Similarly, MITgcm also increases temperature variance as resolution increases ($\gamma = 0.08, 0.13, 0.20$ and $A = 0.18, 0.41, 0.67$ for MITgcm12, MITgcm24, and MITgcm48 respectively). However, as the submesoscale is just beginning to become evident at the ∼2 km grid spacing in MITgcm48 (*Capet et al.*, 2008), it is again difficult to be confident that resolution of the submesoscales is responsible for the changes with resolution seen in Figure 3.11. As has been true for all frequency bands except for the near-inertial band, the r_S values are higher for HYCOM than for MITgcm in this set of results on subtidal temperature variance.

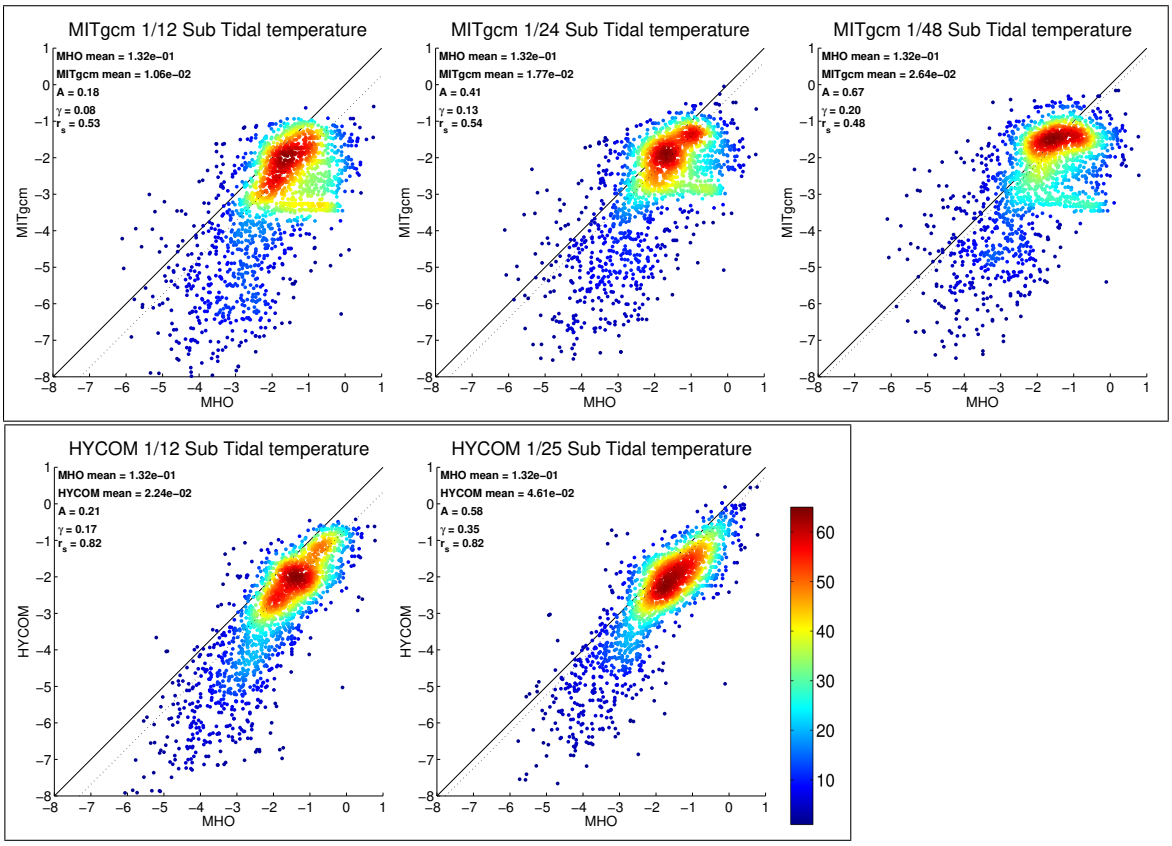

Figure 3.11: As in Figure 3.4 but for subtidal temperature variance.

3.3.6 Mesoscale Frequency Band

Figure 3.12 shows scatterplots of HYCOM and MITgcm mesoscale kinetic energy values against MHO values. From visual inspection, MITgcm 1/12 is biased

lowest compared to MHO,while HYCOM 1/25 is the closest to the one-to one line, although still somewhat lower than observations. Within both models, higher resolution runs generally appear to contain more KE variance, ($\gamma = 0.32, 0.35, 0.45$ and $A = 0.62, 0.62, 0.99$ for MITgcm12, MITgcm24, and MITgcm48 respectively, and $\gamma = 0.50, 0.52$ and $A = 0.70, 0.62$ for HYCOM12 and HYCOM25 respectively). HYCOM is more correlated than MITgcm, with $r_s = 0.80, 0.85$ for HYCOM12 and HYCOM25 versus $r_s = 0.59, 0.63, 0.51$ for MITgcm12, MITgcm24, and MITgcm48.

Figures 3.12 and 3.13 respectively display scatterplots of kinetic energy and temperature variance comparisons in the mesoscale band. As in all the other frequency bands except for the near-inertial band, the HYCOM scatterplots have a visually tighter appearance, and accordingly are associated with larger values of the correlation coefficient r_s. The ratios of the means, γ, are also closer to 1 in HYCOM, especially for temperature variance. Increased resolution tends to improve performance in both models. The HYCOM A, γ, and r_s values computed from the HYCOM runs used here are similar to those computed in the analysis of low-frequency eddy available potential energy in older HYCOM runs in *Luecke et al.* (2017).

3.3.7 Summary of Mean Temperature Variance and KE in all Frequency Bands

While we have compared the integrated variance within each frequency band (supertidal, semi-diurnal, diurnal, near-inertial, subtidal, and mesoscale) for temperature variance and kinetic energy, some summary figures are needed. Figure 3.14 shows the total integrated variance within each frequency band for all 5 model runs and the MHO locations for both temperature variance(top) and KE (bottom). In some frequency regemes, within each model, increased resolution leads to more variance. This is particularly noticable in the case of both supertidal KE and temperature variance. To a lesser extent this is also the case within the mesoscale band. The dramatic

increase in both KE and temperature variance within the supertidal frequency band suggests that the increase in resolution in both HYCOM and MITgcm is resulting in a large increase in energy within the IGW continuum. In other frequency bands, such as the near-inertial band, changes in resolution appear to make little difference. Within the semi-diurnal and diurnal frequency bands, it appears as if differences between HYCOM and MITgcm, such as the presence of paramaterized wave drag make a larger difference than resolution with respect to model-data agreement.

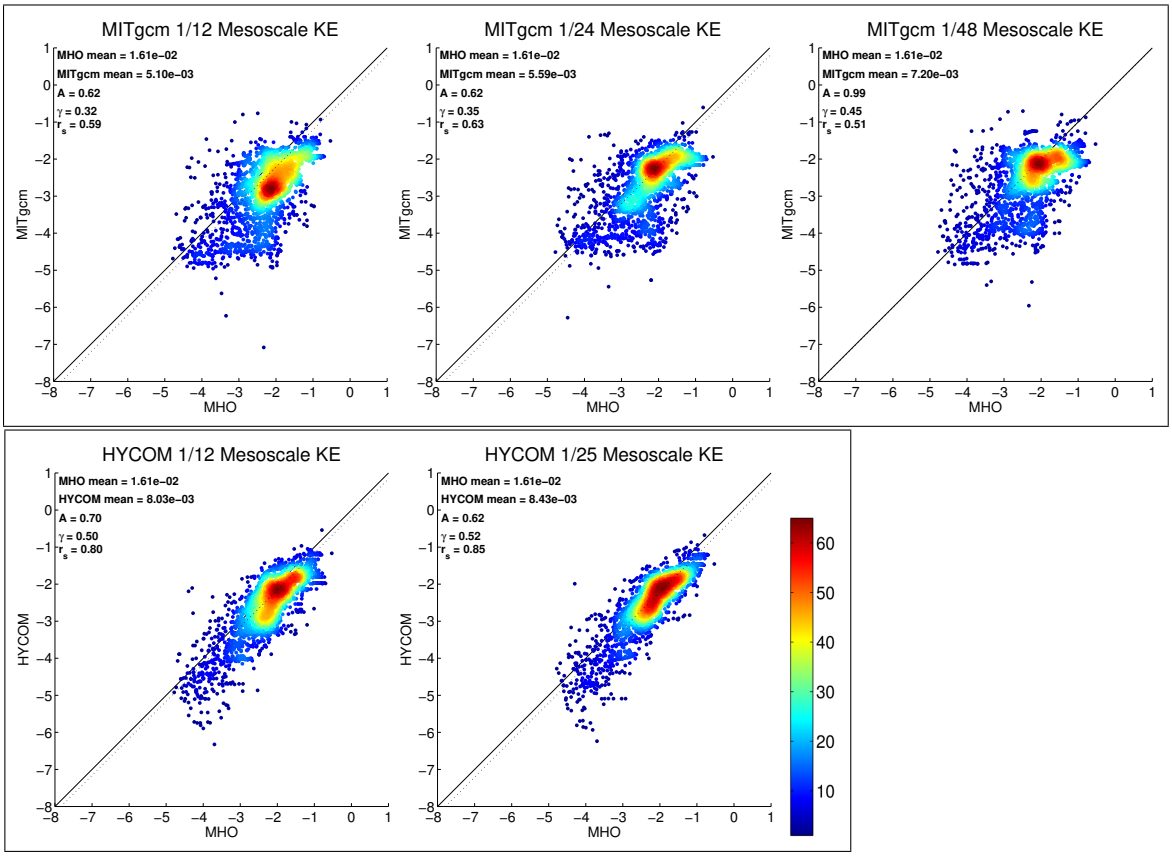

Figure 3.12: As in Figure 3.3 but for mesoscale KE.

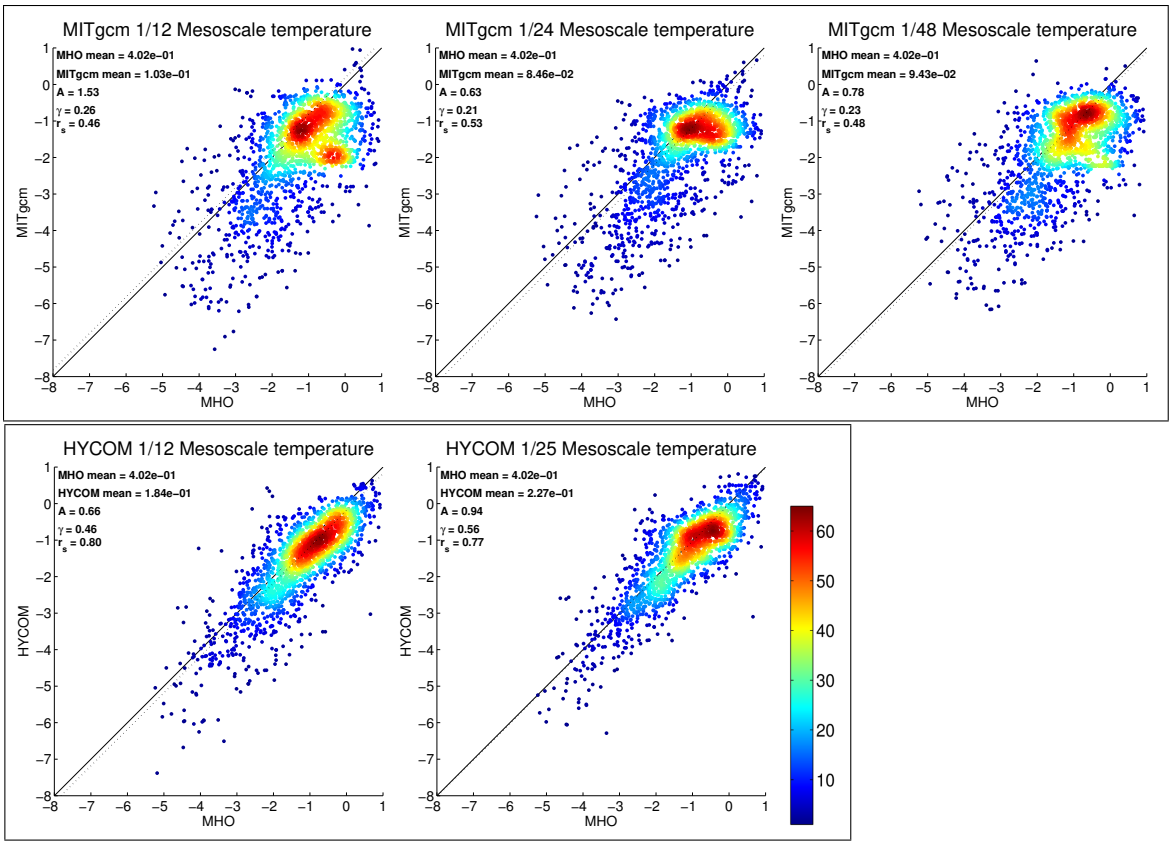

Figure 3.13: As in Figure 3.4 but for mesoscale temperature variance.

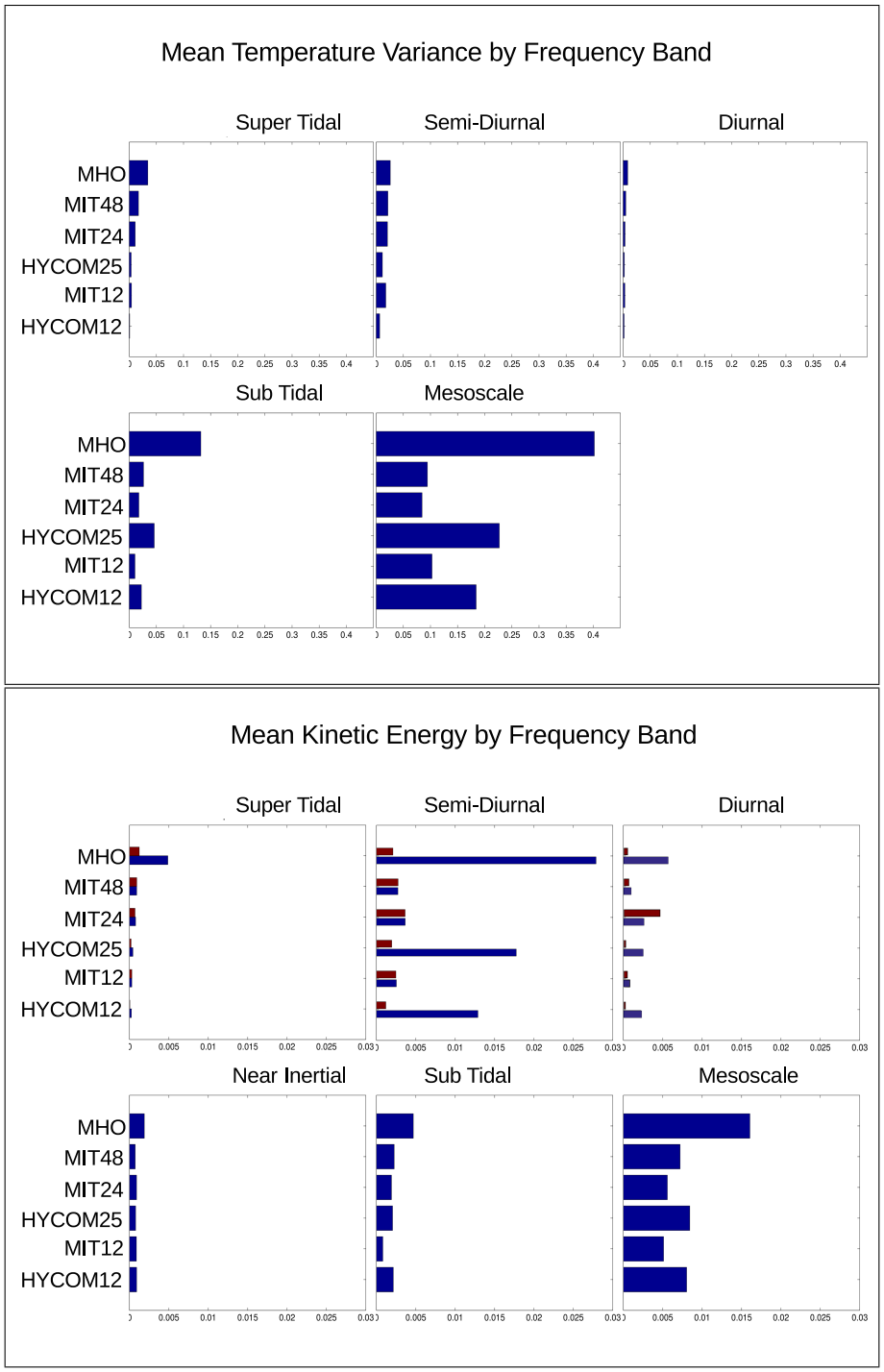

Figure 3.14: (top) Total integrated temperature variance ($^{\circ}C^2$) separated by frequency band (supertidal, semi-diurnal, diurnal, near-inertial, subtidal, and mesoscale). (bottom) Same but for kinetic energy ($m^2 s^{-2}$), with the near-inertial band added in. All bands are averaged over the MHO locations. The red bars denote averages where outliers have been removed.

3.3.8 Global Comparisons of Geostrophic Eddy Kinetic Energy

Prompted by differences between MITgcm and HYCOM in our MHO comparison, we present a global comparison of geostrophic EKE between HYCOM, the AVISO satellite altimeter product, and MITgcm, shown shown in Figure 3.15. The spatial structure in both MITgcm48 (bottom panel) and HYCOM25 (top panel) match those seen in AVISO (center) reasonably well. However, there are several differences. For instance, HYCOM25 appears to have more energy than AVISO in the South Atlantic, Southern Indian Ocean, and South Eastern Pacific, while MITgcm48 does not. Conversely HYCOM25 represents the Gulf Stream and other western boundary currents more accurately than MITgcm48.

As was done in our comparisons at MHO locations, we can also examine the point-to-point comparisons between MITgcm48, HYCOM25, and AVISO. Figure 3.16 shows geostrophic EKE between MITgcm48 and AVISO (left), and between HYCOM25 and AVISO (right) globally, taken from the data given in Figure 3.15. Globally, the linear regression A is higher in HYCOM25 than in MITGCM48, as a result of more outliers at higher energies. MITgcm48 appears more tightly correlated at higher energies. However there is a distinct tail, where MITgcm seems to be over energetic at locations with lower EKE values. As indicated in the γ values, when averaged globally, MITgcm24 slightly under predicts EKE, while HYCOM25 over predicts the EKE. Examination of the correlation r_s reveals that while both models correlate fairly well, while HYCOM12 has a slightly larger r_S value than MITGCM, consistent with the results of our MHO analysis. Lastly, Figure 3.17 shows geostrophic EKE between MITgcm48 and AVISO (left), and between HYCOM25 and AVISO (right) at the MHO locations used in this chapter. The linear regression A is much higher in HYCOM25 than in MITGCM48, again as a result of more outliers at higher energies. At MHO locations MITgcm25 slightly under predicts AVISO EKE, while HYCOM25 over predicts the EKE by a factor of four, although this is likely dominated

by HYCOM25 being biased high at larger EKE values. Unlike most other previous results stated in this chapter correlation r_s in HYCOM25 is lower than MITGCM48, although both models correlate fairly well. In summary, the results of Figure 3.17 do not provide a simple answer for why HYCOM is better correlated with the MHO results than MITgcm is, over most frequency bands.

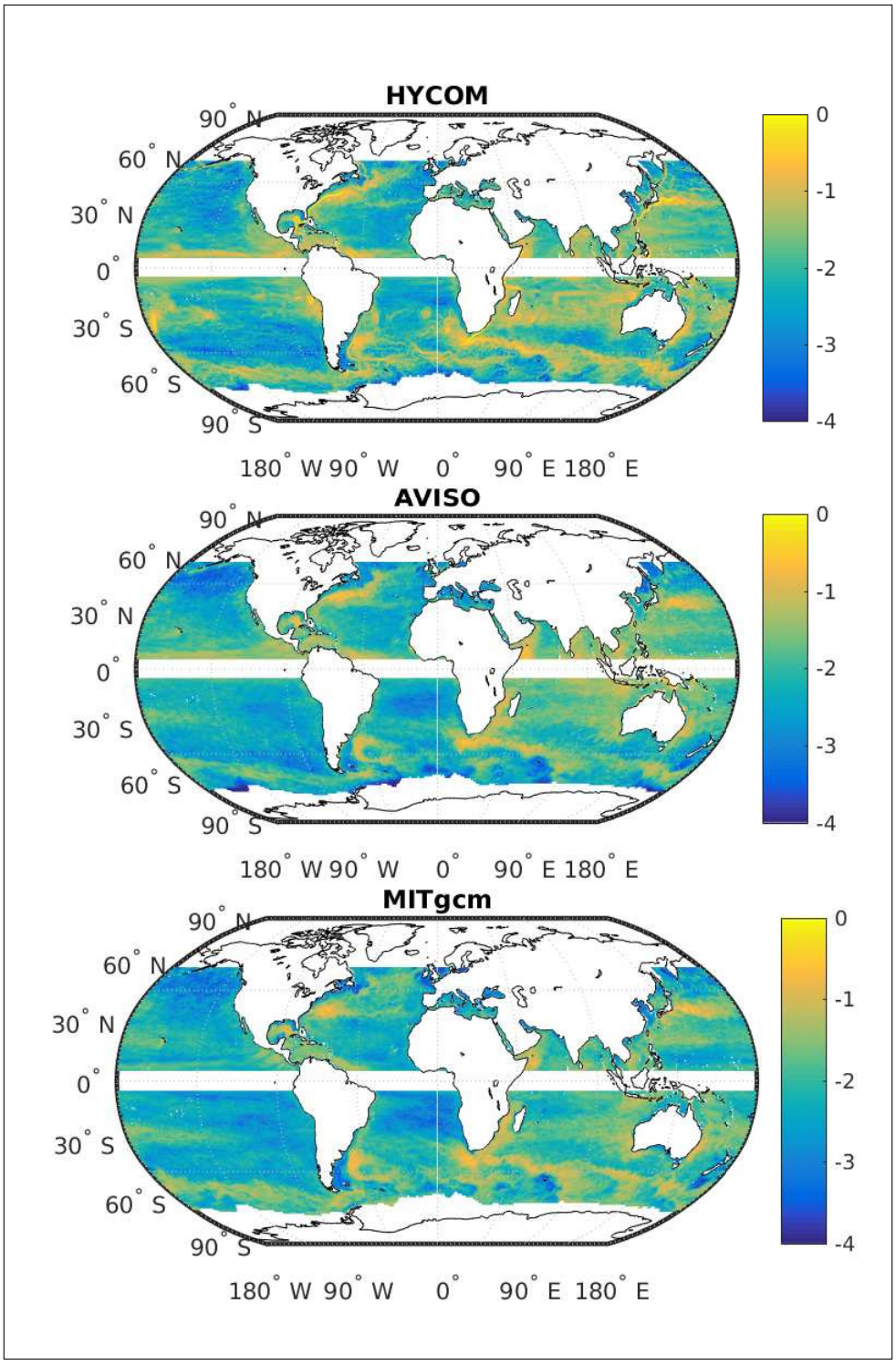

Figure 3.15: Global geostrophic eddy kinetic energy ($\log_{10}(\mathrm{m}^2 s^{-2})$) in HYCOM25 (top), AVISO (center), and MITgcm48 (bottom). Maps are given on a 0.25 degree grid.

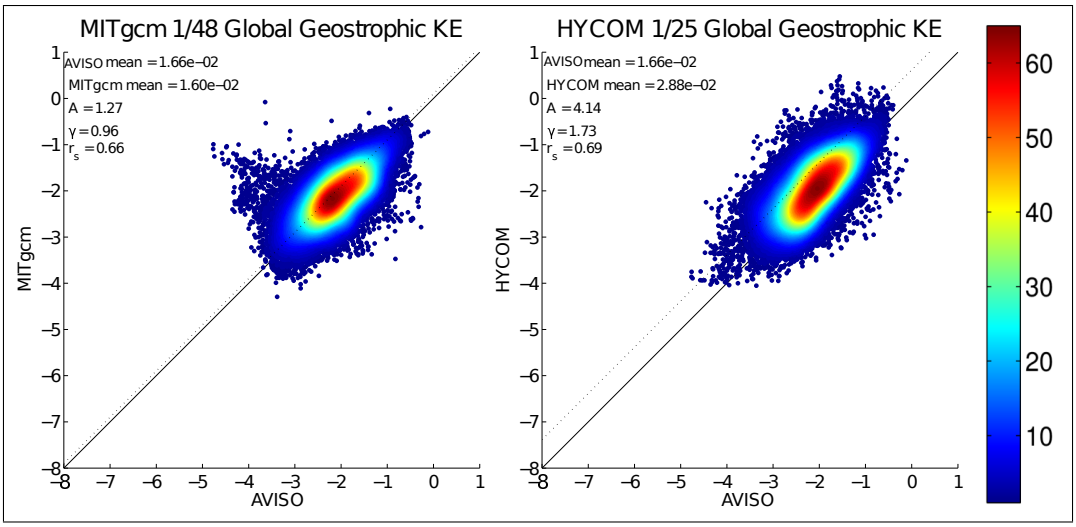

Figure 3.16: As in Figure 3.4 but with geostrophic EKE between MITgcm48 and AVISO (left), and between HYCOM25 and AVISO (right) globally.

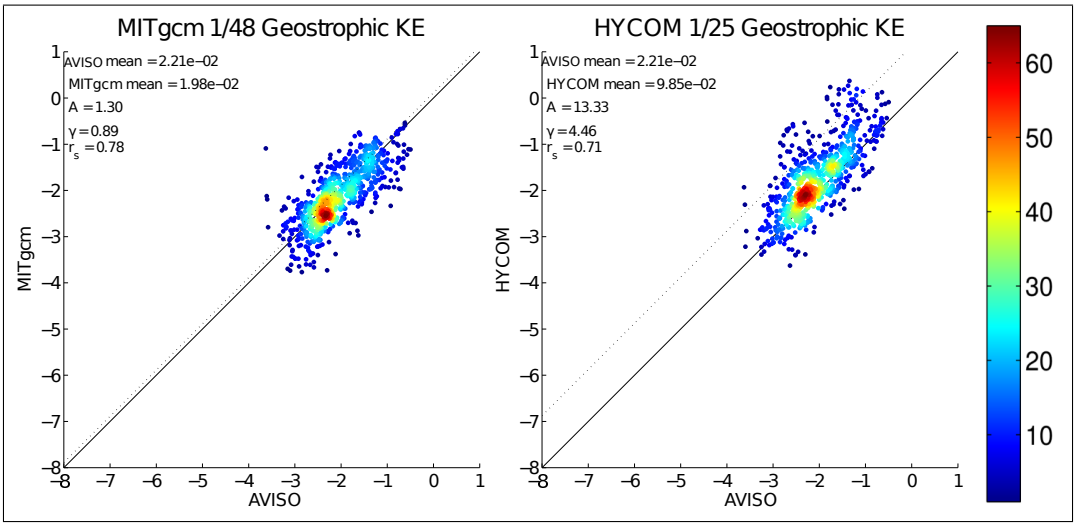

Figure 3.17: As in Figure 3.4 but with geostrophic EKE between MITgcm48 and AVISO (left), and between HYCOM25 and AVISO (right) at the MHO locations.

3.4 Conclusion

In this chapter, we have assessed the frequency content of temperature variance and kinetic energy in multiple resolutions of two global ocean general circulation models with embedded tides (MITgcm 1/12, 1/24 and 1/48 degree, and HYCOM 1/12 and 1/25 degree) using both a database of moored historical observations (MHO). We also compared geostrophic eddy kinetic energy in the models and in the AVISO satellite altimeter product. Model resolution is shown to effect KE and temperature variance within each frequency band differently. For instance, within the near-inertial band, model performance was not dramatically improved by an increase in resolution. However in the supertidal, subtidal, and mesoscale bands (and to a lesser extent semi-diurnal and diurnal bands), models more closely match the observations as resolution is increased. Particularly within the supertidal band, it appears that increasing resolution plays an important role in transferring energy into the IGW continuum. Although both models show advantages and disadvantages in some respects, for instance HYCOM has better spatial correlations than MITgcm at all resolutions and most frequency bands, the highest resolution run of both MITgcm and HYCOM perform very well compared to both observational datasets. As high-resolution GCMs that partially resolve an internal gravity wave continuum become increasingly used both at to study dynamics, and as a tool for informing observational oceanography, model-data validation across a wide range of frequencies becomes increasingly important.

CHAPTER IV

Estimates of Turbulent Dissipation From Fast Sampling Moored Thermistor Chains

4.1 Introduction

Turbulent dissipation drives the small-scale redistribution of energy (momentum and temperature) that is in turn important for the large-scale ocean dynamics, as well as the mixing of tracers. Traditionally, measurements of turbulent mixing in the ocean have often come from direct measurements of the turbulent subranges of shear or temperature (*Osborn and Cox*, 1972; *Gregg*, 1987; *Alford and Pinkel*, 2000). In this work we employ an inertial-convective subrange scaling to estimate turbulence quantities from moored thermistor chains.

As part of the FLEAT (FLow Encountering Abrupt Topography) project, five moorings were deployed allowing both a spatial and temporal view of mixing around Palau, in locations subject to both strong tidal and mesoscale flows. This study aims at better understanding the mixing response to mesoscale, submesoscale, near-inertial, and tidal dynamics as they interact with the steep topography in the region north of Palau.

Previous work is often restricted to lowered ship-based instruments (*Lueck et al.*, 2002) ie. shear probes and χ-pods, and thus is limited in the duration of coverage.

In the case of some moored χ-pod (*Moum and Nash*, 2009) datasets, including long term mixing studies such as *Moum et al.* (2013), vertical coverage is limited. The long time series of ϵ estimated in this work builds upon methodology presented in *Zhang and Moum* (2010) and previously applied in *Musgrave et al.* (2016) to investigate the contributions of a variety of physical processes to mixing, from high-frequency i.e. tidally generated internal gravity waves (IGWs) to near-inertial contributions, and mixing due to low-frequency mesoscale flow across undersea topography. The spacing of thermistors along each mooring allows insight into the vertical mixing signatures of these physical processes.

The mooring data presented here represents unprecedented spatial and temporal coverage of turbulent kinetic energy (TKE) dissipation rate. This chapter aims to present a broad look at dissipation processes, and the groundwork for future more detailed analysis. Through a qualitative assessment of the depth-time series of ϵ, we highlight multiple physical processes that impact the temporal modulation of TKE dissipation. Averaging TKE dissipation in both time and depth at all five mooring locations shows the horizontal structure of TKE dissipation around Palau, and gives order-of-magnitude estimates of how ϵ decays to background levels as a function of distance from topography. Additionally, we present the time-mean depth profile of ϵ at the five mooring locations, providing insight into the vertical structure of mixing in relation to mooring location. Lastly, through band-passing and spectral analysis of ϵ, we are able to isolate contributions of high-frequency, tidally generated internal gravity waves, near-inertial, and low-frequency mesoscale processes on the TKE dissipation rate.

Table 4.1: Depths and Locations of Moorings.

Mooring	Latitude, Longetude	Water Column Depth (m)
F1	008 40.838' N, 134 24.087' E	3390
F2	008 30.164' N, 134 35.508' E	1515
F3	008 32.723' N, 134 37.414' E	1666
F4	008 29.862' N, 134 38.723' E	880
F6	008 28.962' N, 134 38.575' E	434

4.2 Data and Methods

4.2.1 Moored Data

Results are presented for five subsurface moorings deployed from June 2016 through April 2017 around the northern tip of Palau as shown in Figure 4.1. Mooring locations and depths are given in Table 4.1. We designate the moorings as F1, F2, F3, F4 and F6. Moorings are spatially arranged across an area spanning approximately 35km, and at depths varying from as deep as 3390m to as shallow as 434m. Moorings are equipped with 75kHz and 300kHz RDI ADCPs (Acoustic Doppler Current Profilers) to measure velocity, SBE37 CTDs (conductivity, temperature, and depth), SBE56 and RBRSolo thermistors sampling at 1Hz. RBRsolo thermistor measurements provide the temperature gradient spectrum for our estimations of ϵ are made, and which will be discussed in detail below. In addition, mooring F1 was equipped with two McLane Moored Profilers (*Doherty et al.*, 1999) in the lower part of the water column and moorings F2/F3/F4 were equipped with moored χ-pods which could aid in the validation of the estimates made in this study. To illustrate some of the data coverage available from a mooring, Figure 4.2 presents depth-time series of temperature from the RBRsolos (top), velocity at RBRsolo depths (middle) and N^2 (bottom) calculated at the thermistor depths for the mooring F2.

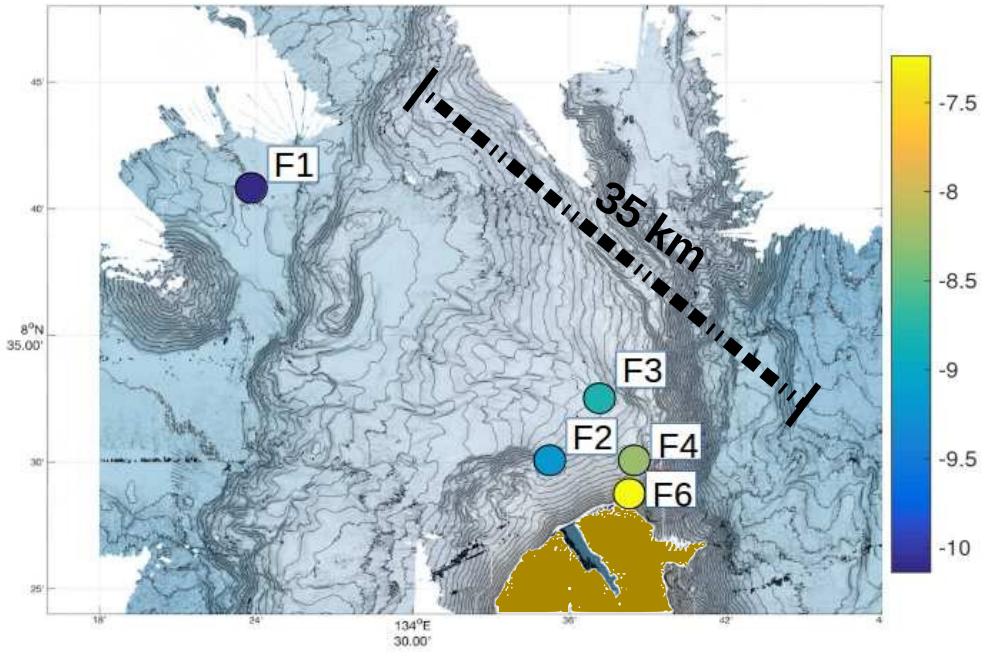

Figure 4.1: Arrangement of moorings presented in this study. Values of vertically and temporally averaged $\log_{10}[\epsilon]$ are given by color.

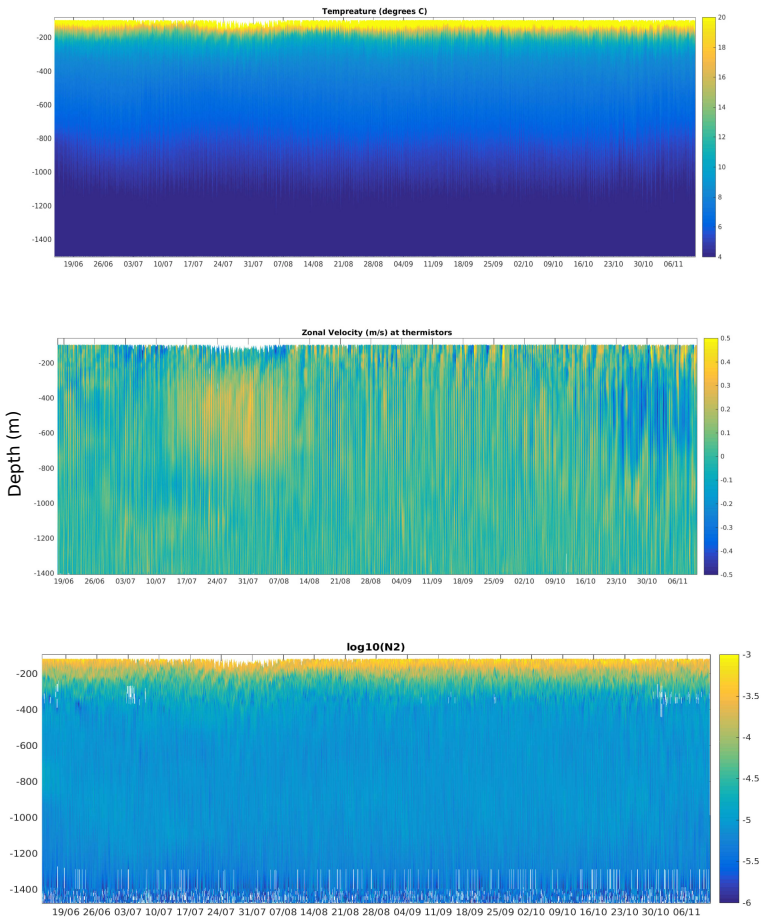

Figure 4.2: Depth-time series of temperature ($°C$) from the RBRsolos (top), velocity (m/s) at RBRsolo depths (middle) and N^2 (s^{-2}) (bottom) calculated at the thermistor depths for the mooring F2 in 2016.

4.2.2 Estimation of ϵ

The methodology for our estimates of the turbulent kinetic energy dissipation rate of ϵ follows the procedure outlined in *Zhang and Moum* (2010), as well as in *Musgrave et al.* (2016). The TKE dissipation rate is estimated from thermal variance dissipation rate χ_T derived from fitting temperature gradient spectra in in the inertial-convective subrange (*Batchelor*, 1959). In order to estimate χ_T from the inertial-convective subrange, we use the method described by *Moum and Nash* (2009) that requires an

estimate of the turbulent kinetic energy dissipation rate of ϵ;χ_T, is defined as:

$$\chi_T = 6D_T \int_0^\infty \phi_{Tx}(\omega) d\omega, \tag{4.1}$$

where D_T is the thermal diffusivity and $\phi_{T_x}(\omega)$ is the frequency spectrum of T_x. The horizontal component of the temperature gradient T_x is computed from the time derivative T_t using Taylor's frozen flow hypothesis $T_x = T_t/U$, where the background flow U is provided by ADCPs located on the moorings.

Following *Osborn and Cox* (1972), we estimate the eddy diffusivity for heat (κ_T) as

$$\kappa_T = \frac{\chi_T}{2T_z^2}. \tag{4.2}$$

The vertical gradient of temperature is computed at each mooring using a centered-difference approximation from thermistors along the mooring. Two-minute-averages were used to compute T_z in this chapter, as was done in Moum and Nash (2009). Assuming a local balance of turbulent kinetic energy (TKE) between shear production and buoyancy production, we obtain another estimate of eddy diffusivity for density κ_ρ,

$$\kappa_\rho = \frac{\Gamma\epsilon}{N^2}, \tag{4.3}$$

where N^2 is the local squared buoyancy frequency, which is calculated from a temperature-salinity relation obtained from ship-based CTD casts at the mooring recovery and deployment, and the local two-minute averaged temperature on each mooring chain. It is worth mentioning that there are numerical difficulties in calculating vertical gradients such as errors introduced in computing N^2 and T_z from in-situ instruments where there is small spatial separation or gradients are weak. Additional issues arise during events with unstable stratification and where sensor separation is small compared to overturn size. Work is ongoing to improve the accuracy of these

calculations. A more detailed discussion of these issues is presented in later in this section. We assume a constant mixing efficiency $\Gamma = 0.2$ (*Osborn*, 1980). Setting $\kappa_T = \kappa_\rho$, then

$$\epsilon = \frac{N^2 \chi_T}{2\Gamma T_z^2}, \tag{4.4}$$

where the TKE dissipation rate ϵ is estimated from thermal variance dissipation rate χ_T.

The temperature gradient wavenumber spectrum in the inertial-convective subrange (*Batchelor*, 1959) that we use to fit our data is given by:

$$\phi_{T_x}(k) = C_T \chi_T \epsilon^{-1/3} k^{1/3}, \tag{4.5}$$

where C_T is the Obukhov–Corrsin constant, taken to be 0.4, and k is the horizontal wave-number. The equivalent frequency spectra is:

$$\phi_{T_x}(\omega) = C_T \chi_T \epsilon^{-1/3} (2\pi\omega/u)^{1/3} u^{-1}. \tag{4.6}$$

Substituting Equation (4.4) into Equation (4.6) provides an expression for the Batchelor spectrum in terms of χ_T or ϵ. A least-squares procedure is then used to fit the observed spectra between the frequency ranges $0.01 < \omega < 0.2$ Hz. Estimates of ϵ are made with running three-hour spectral average with 120 second segments utilized for the least-squares fit to the $\omega^{1/3}$ spectrum. This allows us to make estimates of ϵ from χ calculated over the inertial subrange. Figure 4.3 shows several temperature gradient spectra and the associated $\omega^{1/3}$ fits taken from a depth of 900m on mooring F2. The spectra were selected by binning events of both like χ_T and ϵ. The blue specra show fits for relatively low values of ϵ ($10^{-10}(W/kg)$) and χ_T ($10^{-10}(K^2 s^{-1})$), while the green specra show fits for relatively high values of ϵ ($10^{-8}(W/kg)$) and χ_T ($10^{-8}(K^2 s^{-1})$).

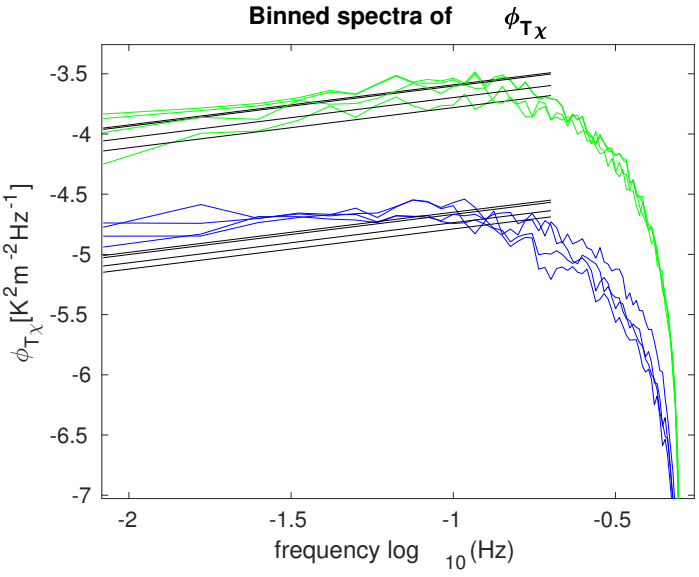

Figure 4.3: Temperature gradient spectra (ϕ_{T_x}) for events that produce high (green) and low (blue) values of ϵ ($10^{-8}(W/kg)$) and ($10^{-10}(W/kg)$) respectively located on F2 at a depth of 900m. Black lines represent the least-squares-fit to to the $\omega^{1/3}$ spectrum.

The dissipation estimates in the presented work are made from inertial sub-range scaling of the temperature gradient spectra, and thus are sensitive to vertical derivatives of temperature and stratification N^2. To further illustrate some potential pitfalls of the analysis made here, we focus on the data taken from mooring F3, because there are noticeable features in the results that raised concerns with the way the derivative analysis was performed.

Estimates of the TKE dissipation rate, ϵ, require a time varying background field of the change in temperature with respect to the change in depth, dT/dz. The Brunt-Väisälä buoyancy frequency, N^2, must also be calculated at the location of each thermistor. Care must be taken during these computations to ensure that there there are no large jumps in value, discontinuities, or anomalous changes in the derivatives of these fields that could introduce errors in the estimates of TKE dissipation. Issues such as thermistor biases from a constant offset in temperature measurements, as

well as extremely close spacing of the instruments, can potentially introduce errors in the calculation of either dT or dz. As we examine the time-mean profiles of N^2 and dT/dz at mooring F3, a few places along the water column exhibit characteristics of these derivative issues, as shown in Figure 4.4. In the left panel of Figure 4.4, dT/dz has a slight discontinuity near a depth 300m, most likely caused by a bias in a single thermistor. In addition, there is an oscillatory variation around 1600 meters, possibly caused by the close spacing of instruments at these depths. Both are highlighted with red circles.

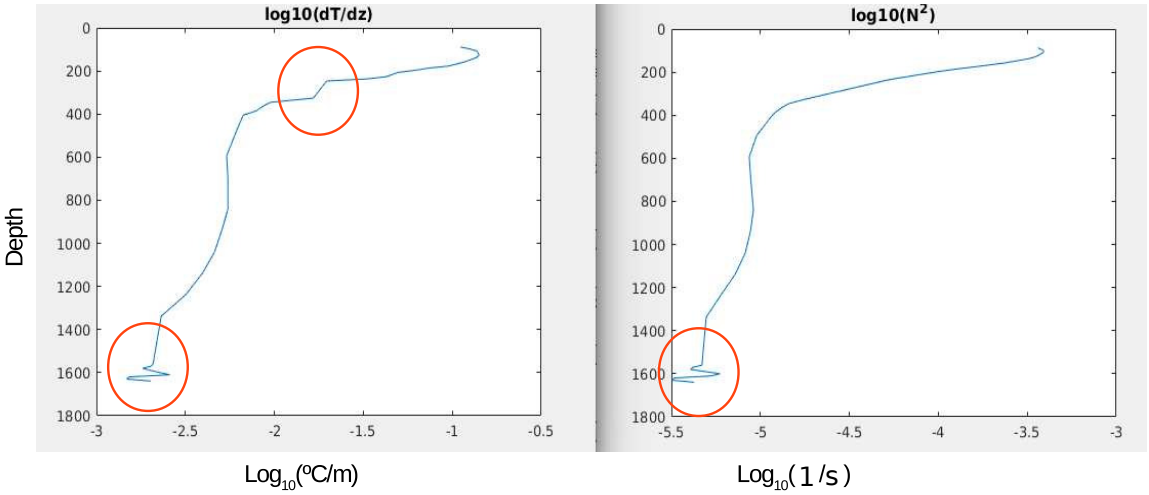

Figure 4.4: Time-averaged profiles of dT/dz (left) and N^2 (right) showing locations of "jumpy" derivatives (marked in red circles).

Initial work in removing the data from these depth levels in the calculations of ϵ presented in this chapter indicate that the qualitative results such as in the spatial decay rate of TKE dissipation, and the time-averaged dissipation profiles indicating bottom intensification, are not greatly affected by these derivative issues. However, additional work to identify and smooth these problem areas throughout the entire mooring data-set is ongoing.

One result from this chapter indicated a "hotspot" of mixing on mooring F3

around 1000m depth. Initially these mid-water column hotspots of mixing raised suspicions of a larger problem in the calculations of ϵ related to a single instrument anomaly. However, closer examination of the data, including an analysis of the high-passed temperature variance, indicates that these hotspots are independent of any derivative related issues, and the experimental indications are present at several contiguous thermistor locations along the mooring as can be seen in Figure 4.5. This would suggest that these hotspots are indeed a physical signal.

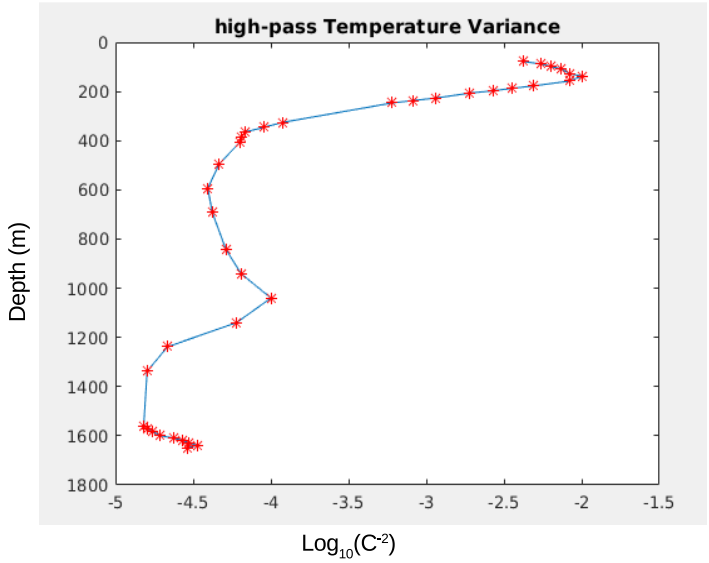

Figure 4.5: High-passed (frequencies greater than 120 seconds) profiles of temperature variance from thermistors at F3. Clearly visible is a local maxima at 1000m which corresponds to the depth of elevated ϵ seen at F3.

Another issue of concern was the method used to infer of salinity from temperature. The results presented here use a Temperature-Salinity (T-S) relationship that comes from ship-based CTD casts in the vicinity of the moorings. Two-minute averaged temperature time series are transformed into salinity values using a lookup table based on a polynomial fit of the CTD casts. In previous work, this transformation has been done with a linear T-S relationship from the CTDs contained on the mooring. There are some concerns with a linear interpolation, because at many of the moor-

ings, there are not enough CTDs to constrain an accurate T-S relation, particularly when the interpolated region is outside the span of the available CTDs. The T-S relationship in Figure 4.6 shows data taken from the ship based CTD casts, represented as black lines, which were used to develop the T-S fit for use in this analysis. The colored point clouds show the T and S data from the moored CTDs smoothed over a 3-day window. The magenta dots represent what the linearly interpolated T-S curve from the moored CTDs might look like. It is clear that a linearly interpolated T-S relation from just the moored CTDs does not represent some active regions of the curve. At other moorings, some of the thermistors lie "outside" of the endpoints, making interpolation more challenging when using a linear fit for the approximation from the moored CTDs.

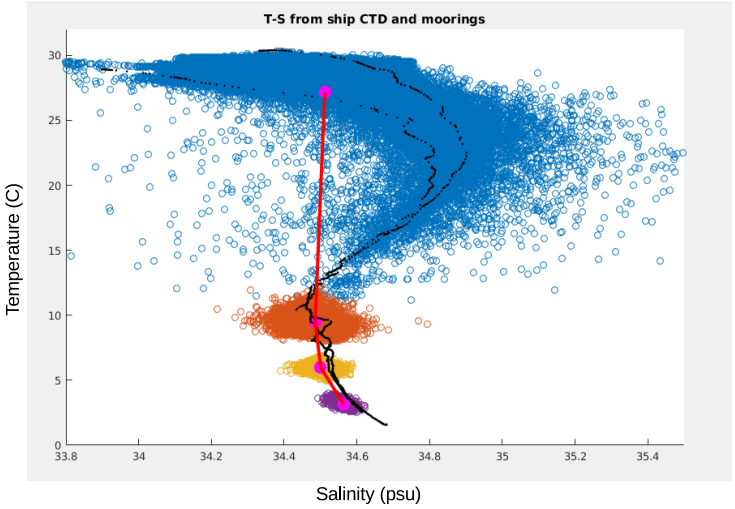

Figure 4.6: T-S relationship taken from the ship-based CTD casts (the black lines). The colored clouds show the T and S data from the moored CTDs smoothed over a 3-day window. The red line shows an example of issues arising from using interpolated moored CTD data to infer a T-S relation.

Work is ongoing to account for the slow time varying nature of the T-S curve used

to calculate salinities needed for the calculation of N^2. Because of the noisy nature of the data, I believe that a Kalman filter constraining the moored CTD-based time varying salinity to a "realistic" T-S curve may be a good avenue for combining both approaches in an optimal manner.

Figure 4.7 shows the extent of the seasonal variability of the T-S curve in the study region using glider-based CTDs (Fitzmorris and Rudnick (in prep)), and can be used to gain a feel for the deviation possible in T-S space. Initial calculations made by varying the T-S relationships within the bounds suggested by the curves shown in Figure 4.7 indicate that the effect of changes in the T-S curves on the final value ϵ is small, although more work is needed to quantitatively assess the precise effect.

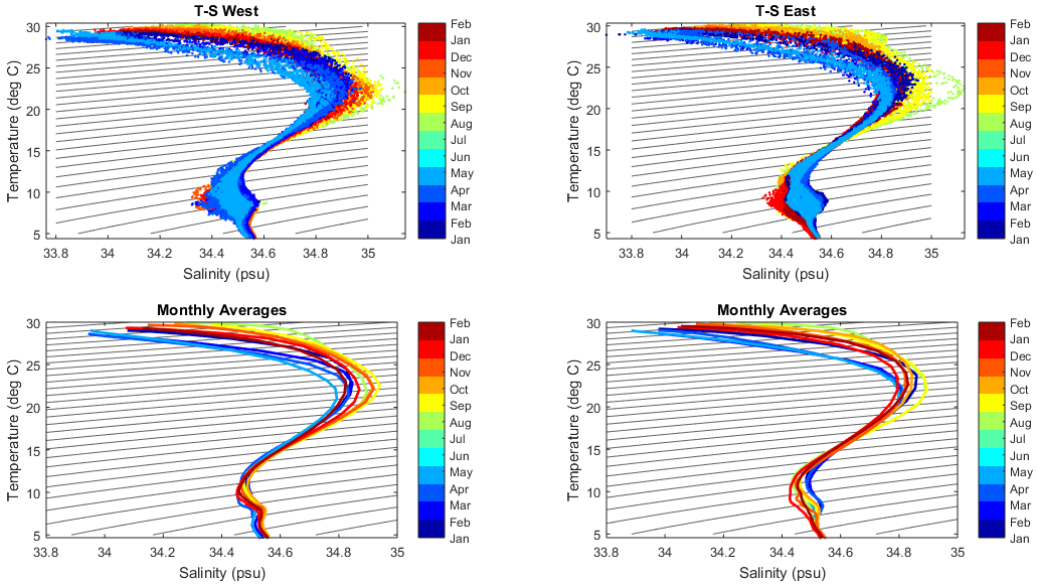

Figure 4.7: T-S relationships taken from glider lines West (left) and East (right) of Palau. The top two panels are un-averaged, while the bottom two panels show monthly averages. Color represents time of year.

Another check on the validity of calculating the T-S relation and subsequent values of N^2 can be seen in Figure 4.8, where the N^2 calculated from time-averaged CTD measurements contained on the mooring are compared with the N^2 values calculated from two seperate ship-based CTD casts and the inferred estimates used

in this chapter. It is notable that there is a large swing in the ship-based values at the 1600 meter depth, which may indicate one possible physical explanation of the variation in the time-averaged curve. More work is needed to investigate this phenomenon.

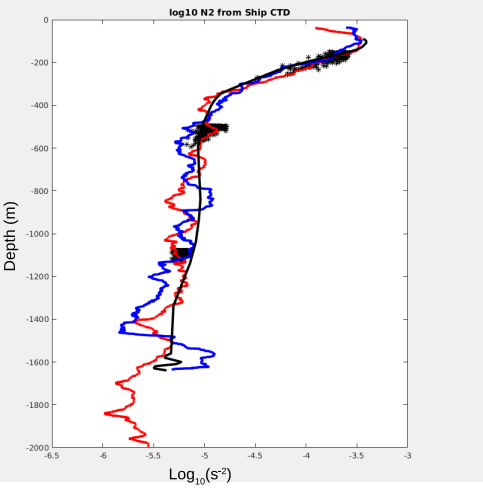

Figure 4.8: Depth-profiles of N^2. The solid black line is the time-average of the N^2 inferred from the thermistors on F3 used in the estimates in this chapter. N^2 calculated from the CTDs contained on the mooring are marked with black stars. The red and blue curves show N^2 calculated from 2 ship based CTD casts, at the mooring deployment and recovery respectively.

In summary, the mixing "blip" seen at 1000m in F3 appears on closer inspection to be an actual physical signal. The minor issues regarding the introduction of noise using the time-averaged T-S relationship in the derivative calculation do not seem to affect the overall computation of ϵ as it is presented in this chapter. Additional work will be done in these areas as the results in Chapter IV are prepared for publication.

4.3 Results

We first present to the reader a qualitative examination of the depth-time series of ϵ located at F2, with a focus on the multiple processes present in the signal, such as tidal cycles, spring-neap modulation, eddy activity, and near-inertial events. We then focus on the spatial horizontal variability of time- and depth-averaged ϵ at all five moorings to illustrate the decay of turbulent dissipation as a function of distance from local topography. Next, we display the temporally averaged profiles of ϵ at all five moorings. Lastly we revisit F2 to examine the specific frequency contributions to variance in the ϵ signal through spectral analysis and band-passing.

4.3.1 A Qualitative assessment of dissipation at F2

Focusing on one individual record allows the examination of the different physical processes that influence the temporal variability TKE dissipation. Figure 4.9 shows isolated individual events at the mooring F2. The upper left inset of Figure 4.9 highlights a low-frequency event lasting on the order of 10 days near 31/7/16, which is also associated with mooring blow down. This event is likely due to a mesocale feature impinging upon the mooring. This signal is associated with a weakening of the spring neap-signal, and another 'eddy' event at 30/10/16 appears to be associated with enhanced ϵ.

In the upper right inset of Figure 4.9, there are distinct areas of elevated ϵ that can be seen around 200m and shallower, corresponding to the 3.5 day inertial period at the mooring. These peaks in ϵ are associated with wind driven inertial wave mixing (*Alford et al.*, 2016). Consistent with expectations, these signals are isolated to the upper water column.

At F2, the TKE dissipation signal ϵ has both a strong diurnal, and semi-diurnal signal. This can be seen in the lower left inset in Figure 4.9. However at the time period shown, the predominant signal is the diurnal tide. Dissipation appears to

be elevated closest to the bottom, especially in the case of the diurnal signal. This is consistent with the generation and breaking of internal tides. One of the most apparent signals in ϵ (visible in F2 but especially apparent at the other mooring locations) is the spring-neap cycle. The spring-neap cycle modulates ϵ through several orders of magnitude.

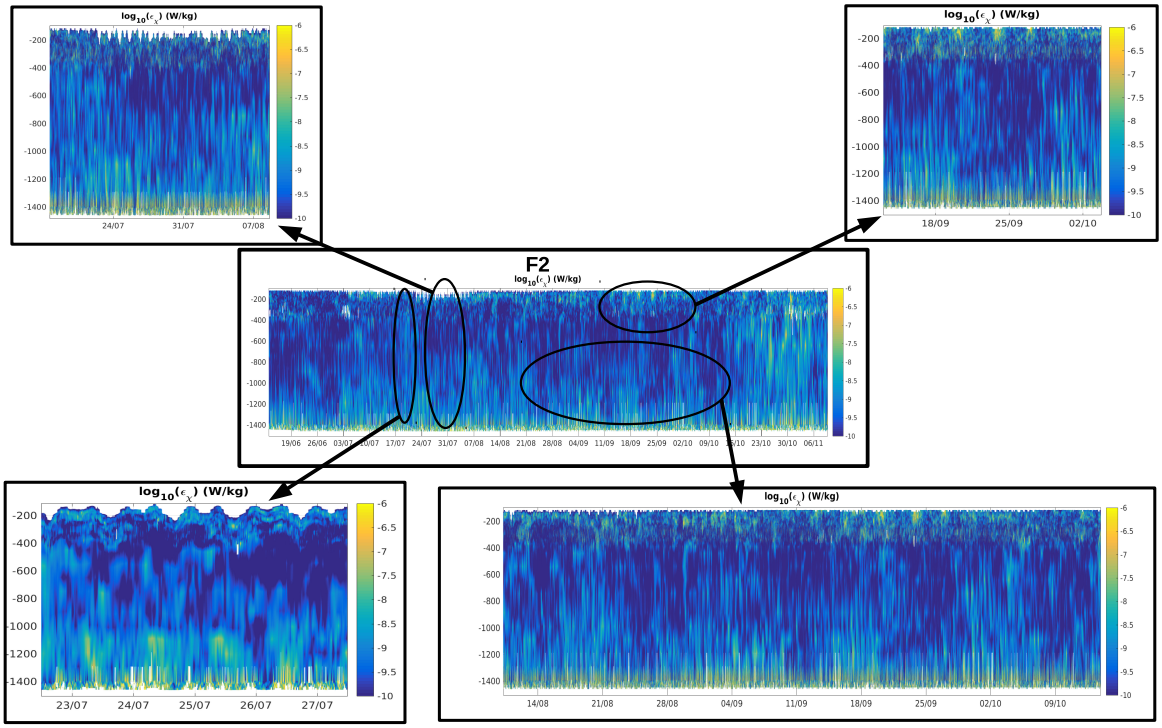

Figure 4.9: Depth-time series of ϵ at F2, with insets focusing on low-frequency (upper left), near-inertial (upper right), tidal (lower left) and spring neap (lower right) modulation.

4.3.2 Time-Depth TKE Dissipation

Estimates of the TKE dissipation rate show a large amount of temporal variability on a variety of time scales, as shown in the time-depth series of ϵ at all five moorings (Figure 4.10). All five moorings are shown with the same color bar for ϵ to highlight the dramatic difference in dissipation values between individual moorings.

As the moorings decrease in distance from topographic features of the near field,

(from top to bottom in Figure 4.10), ϵ increases through several orders of magnitude. The difference in the magnitude of ϵ can further be seen in Figure 4.1, where the vertically and temporally averaged ϵ shows a decay of approximately three orders of magnitude between F1 (far field) and F6 (near-field), a distance of 35km. Between F6 and F4, the mean dissipation rate of TKE ϵ drops by nearly a factor of 10. At F1, the predominant signal in ϵ appears to be low-frequency variability associated with eddy activity. At F2 a wide range of processes can be seen in the ϵ signal as discussed in the previous section.

At moorings F3 and F4, the increasing background levels of turbulent dissipation become evident, and the spring-neap cycle becomes the dominant feature. However the effects of the eddy event around 31/7/16 are still clearly visible. At F6, both the shallowest and closest mooring to Palau, ϵ variability appears uniform throught the water column, reaching from near the bottom to the upper extent of the moor-ing. The vertical structure will be discussed in more detail in the following sections. Additionally, the spring-neap cycle has become the dominant feature.

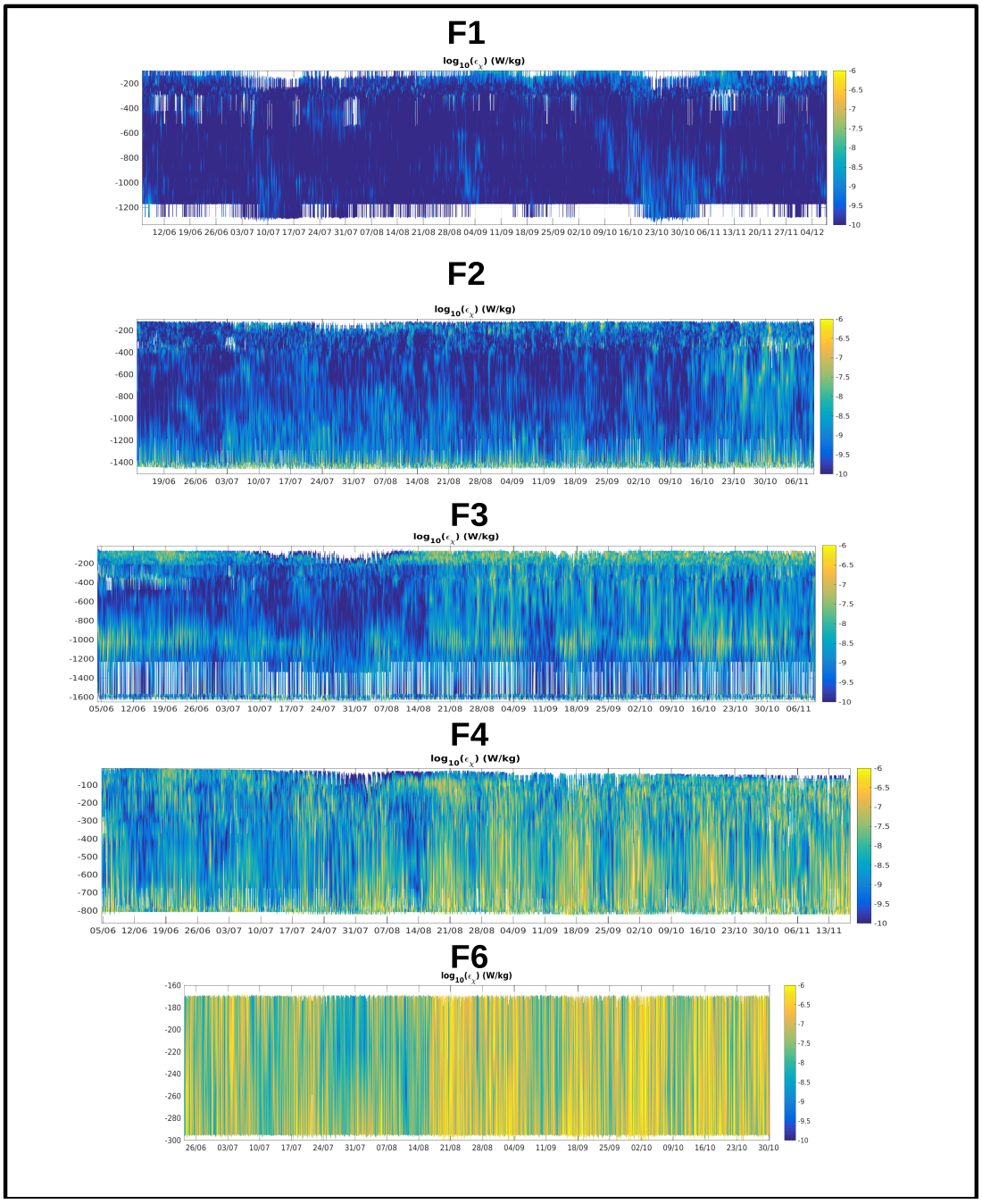

Figure 4.10: Time-depth series of ϵ at all five mooring locations.

4.3.3 Vertical Structure

Time-averaged profiles of both the thermal variance dissipation rate χ and the TKE dissipation rate ϵ show elevated dissipation in the upper water column, and

near the bottom at most locations as seen in Figure 4.11. At F6, the shallowest mooring, ϵ is relatively constant throughout the water column compared to the other moorings, consistent with observations made in the previous section. At F2, F3, and F4, moorings in which estimates of ϵ extend close to the bottom, a local maxima can be seen characteristic of locally topographically influenced mixing. It should be noted that these plots are preliminary; For example, the time-average profile of F3 is influenced by the regions of missing data below 1000 m that can be seen in figure 4.5. Further analysis is needed to assess the source of this missing data. The bottom right panel of Figure 4.11 shows profiles of velocity to illustrate the relative magnitude of velocity at all five moorings.

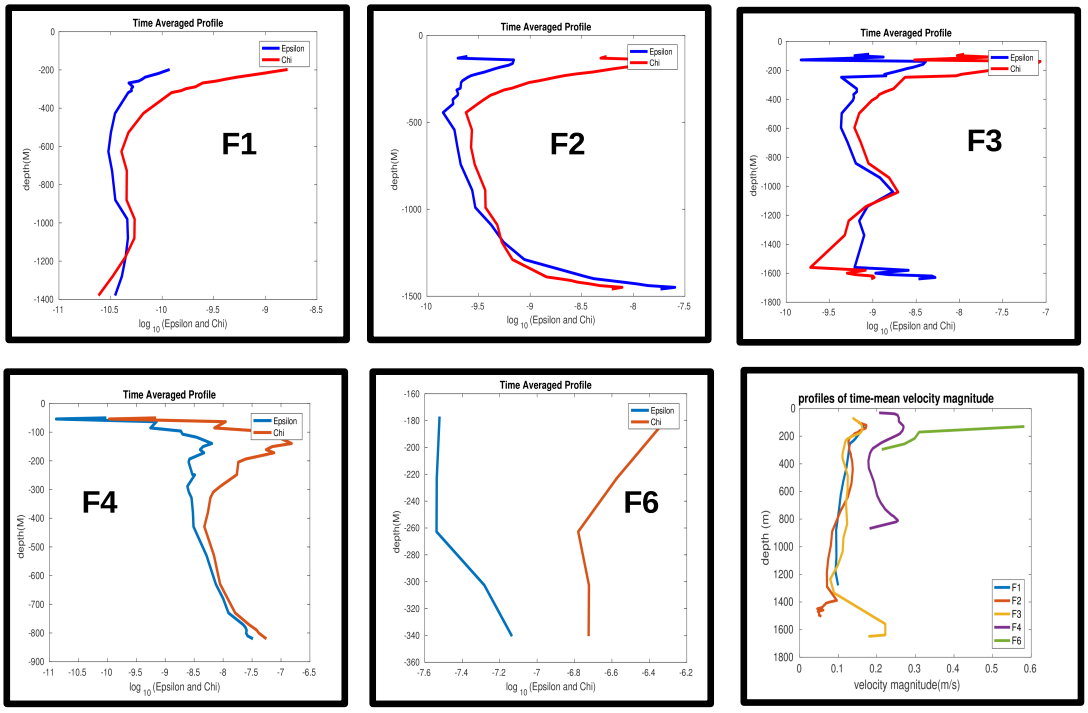

Figure 4.11: Time-averaged profiles of both the thermal variance dissipation rate χ and the TKE dissipation rate ϵ at F1-F6, and the Time-averaged velocity magnitude profile at all moorings (bottom right).

4.3.4 Frequency Content

To better illustrate the temporal variability of ϵ, we present band-passed depth-time series at F2. Figure 4.12 shows the band-passed signal of ϵ at F2 for selected frequency bands of interest. the top inset of Figure 4.12 shows the full ϵ signal, while the subsequent panels (moving from top to bottom) show the diurnal, semi-diurnal, near-inertial, super-tidal, sub-inertial, and spring-neap cycles respectively. Separating the dissipation signal by frequency content helps show the relative contributions to the overall signal, although it is important to note that the band-passing only shows the variance in the signal and not the relative magnitude of the mixing.

From inspection, areas of interest seem to include the bottom intensification of the semi-diurnal signal corresponding to spring-neap cycles, and the near-surface signal at near-inertial-periods.

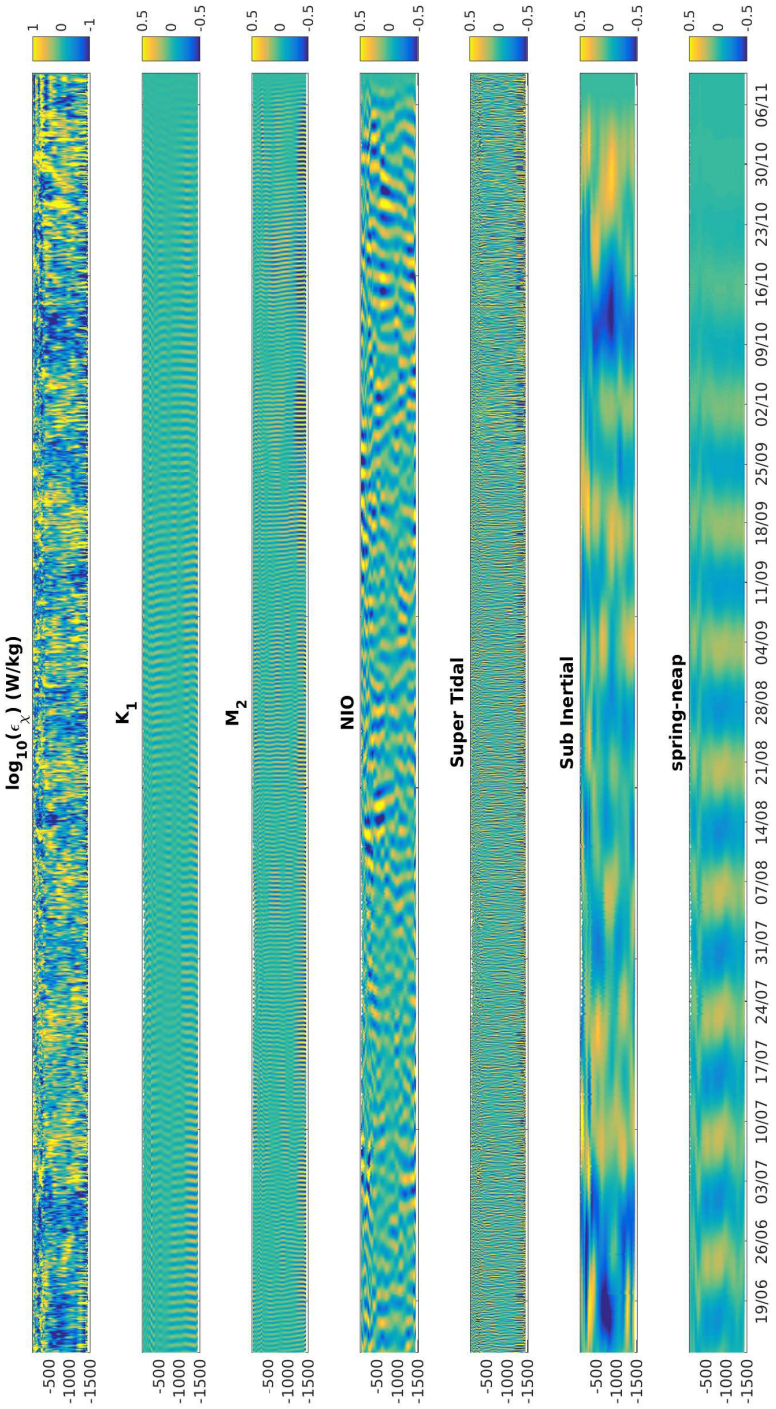

Figure 4.12: Band-passed ϵ at F2 for several frequency bands of interest. Frequency bands from top to bottom are: Full signal, K1 and M2 (the largest diurnal and semidiurnal tides), the near-inertial period, super-tidal, sub-inertial, and the spring-neap cycle.

In order to further highlight the importance of different processes modulating turbulent dissipation, we present frequency spectra of ϵ. The top panel of Figure 4.13 shows the frequency spectra of the log of ϵ near the surface, averaged between 100m and 300m (red curve), and at depth, averaged between 1000 and 1500m (blue curve). Both the shallow and deep spectra have tidal peaks. However the shallow spectrum shows a large peak at the inertial period. The bottom panel of Figure 4.13 shows the depth-spectra for all estimates of ϵ on F2. While variance at the spring neap and semi-diurnal tides appears to be fairly uniform through out the water column, variance at the near-inertial frequency decays rapidly away from the surface. Much of the variance in ϵ occurs at frequencies higher than the Coriolis frequency f, suggesting a large portion of the variance in ϵ could be a result of breaking internal gravity waves.

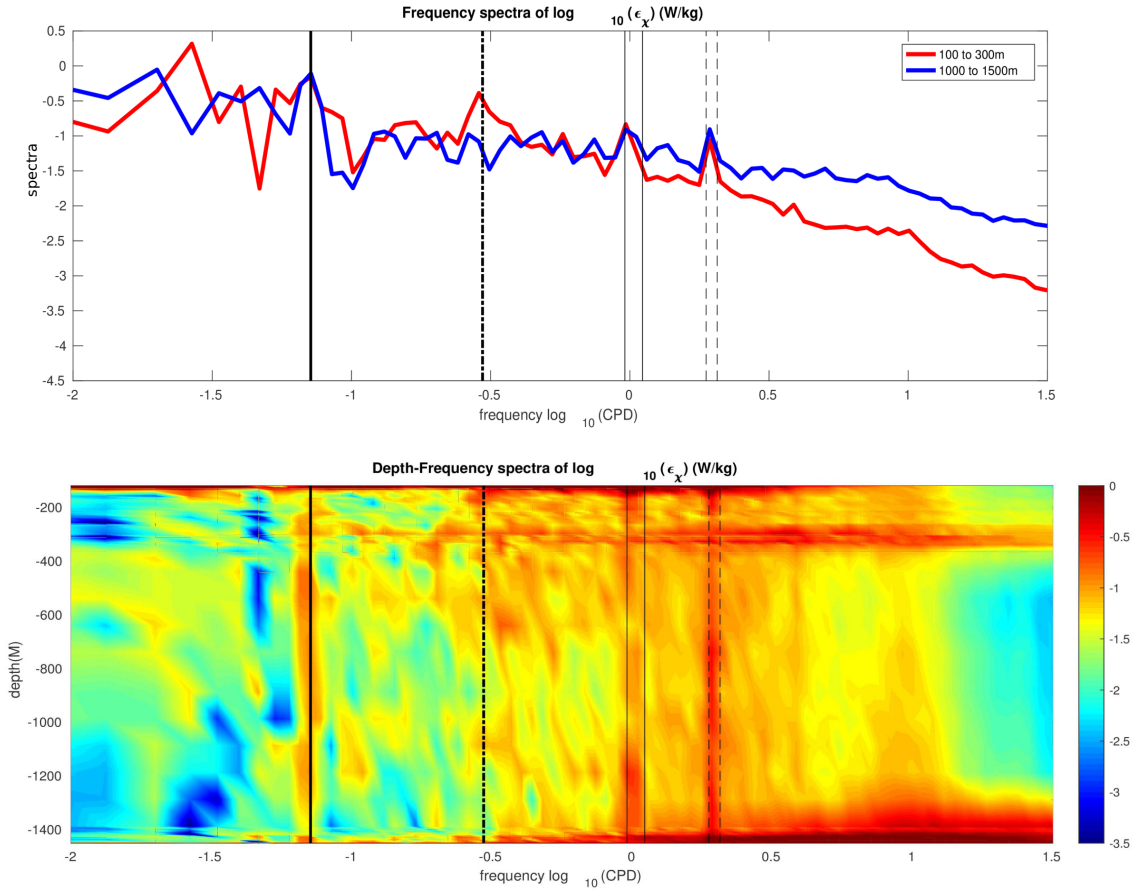

Figure 4.13: (Top) frequency spectra of ϵ near the surface averaged between 100m and 300m (red curve), and at depth, between 1000 and 1500m (blue curve). (Bottom) Variance-preserving depth-frequency spectra of ϵ at F2. Units are $(\text{Watts/Kg})^2\text{CPD}^{-1}$. Vertical lines from left to right are: Spring-neap, inertial period, diurnal, and semi-diurnal tides.

4.4 Conclusions

Depth-time series of the TKE dissipation ϵ have been estimated at five mooring locations. The location of this study provides ideal conditions to examine the impact of mesoscale and tidal flows impinging on abrupt topography. From the examination of the depth-time series of ϵ at a single mooring, we are able to diagnose the presence of

tidal, near-inertial, and mesoscale influenced dissipation. The presence of a dominant spring-neap cycle, especially at moorings F2, F3, F4 and F6 indicate that the strength of the tides is important in determining the local turbulent dissipation, especially in areas of close proximity to topographic features and islands.

The strong spring-neap cycles often seen in signals of ϵ suggest that the breaking and dissipation of internal tides play a significant role in mixing, particularly in the near-field around Palau. Additionally, we show that ϵ decays rapidly with horizontal distance from topography, highlighting the importance of flow dynamics interacting with topography for mixing in the ocean.

The far-field mooring, F1, indicates a dissipation signal that is predominantly dominated by low-frequency mesoscale timescales, while the closest mooring to topography, F6, shows signals that are dominated by the tides and spring-neap cycle. At F2, F3, and F4, the dissipation shows tidal, spring-neap, and mesoscale signals, as well as near-inertial influence on dissipation events. Average vertical profiles show enhanced near-bottom dissipation, as well as enhanced dissipation in the upper water column, which is confirmed by the presence of near-inertial peaks in the shallow spectrum of ϵ at F2. The results presented here suggest that turbulent dissipation is a multi-scale problem, being influenced by low-frequency, inertial, internal gravity wave, and tidal dynamics.

CHAPTER V

Discussion

In this work, we show that ocean general circulation model (OGCM) output can be useful for the study of physically energetic processes such as mesoscale eddies, tides, and internal gravity waves (IGWs). We then explore the local effects that these processes have on turbulent dissipation, an important next step in further improving parameterizations of momentum and energy damping used in OGCMs.

In Chapter II, we compare the eddy available potential energy (EAPE) from both a free-running and data-assimilative OGCM (HYCOM) to global estimates of EAPE derived from Argo floats. We find both the HYCOM simulation and reanalysis predict globally area averaged EAPE estimates that are within 10% of Argo global estimates. Furthermore, many large-scale spatial patterns seen in the Argo estimates, such as western boundary currents, are reproduced by both models reasonably well. We show that data assimilation improves the reproduction of these large-scale features. Interestingly, at the locations of moored historic estimates, both the highest EAPE estimate (MHO) and lowest estimate (Argo) which are made from both observational data sets used in this study differ by only about 50%, with both model runs falling in between the two observational data sets.

In Chapter III, we build on the results of Chapter II by comparing both EAPE, through the proxy of temperature variance, and kinetic energy (KE) in two dynam-

ically different OGCMs, MITgcm and HYCOM, to the values seen in observational data. In this chapter, we separate the EAPE and KE into different frequency bands delineating different dynamical processes such as mesoscale eddies, IGWs, etc. Within these two models, we compare runs of three different resolutions. (MITgcm 1/12, 1/24 and 1/48 degree, and HYCOM 1/12 and 1/25 degree). Both models are simultaneously forced by the astronomical tidal potential and rapidly changing atmospheric fields, key components for the generation of an IGW continuum. By separating energy content into multiple frequency bands of interest, we are able to explore the impact of model resolution on the different physical processes described in Chapter I.

In some frequency regimes, the horizontal resolution of the model has a large impact. In the super tidal band, the highest MITgcm resolutions contain more variance by a factor of about five than their lowest resolution counterparts. Even so, the highest resolution MITgcm runs still underestimate the super tidal KE by a factor of two or more compared to the moored historic data. The HYCOM simulations under estimate the super tidal variance by an even larger factor. This suggests that the IGW continuum in OGCMs is extremely dependent on the horizontal resolution of the models being sufficiently fine to allow for nonlinear wave-wave interactions. Future increases in resolution will continue to improve the realism of the modeled IGW continuum.

In the semidiurnal frequency band, we find that for KE, all three MITgcm runs appear to be biased high compared to the observational estimates, while HYCOM lies closer to the one-to-one line. It is likely that the topographic wave drag employed in HYCOM plays in important role in dissipating KE to realistic levels. It has been shown by *Ansong et al.* (2015) that extra damping, such as wave drag, is needed to make modeled internal tide SSH signatures agree with altimeter observations. Thus, the lack of wave drag in MITgcm is a likely explanation for its over energetic semi diurnal KE values. Likewise, semi diurnal temperature variance in HYCOM is weaker

on average than in MITgcm, and we suggest again that this may also be due to the wave drag employed in HYCOM.

One theme commonly seen across most frequency bands is the higher point to point correlations between models and data seen in HYCOM when compared to MITgcm. In several frequency bands such as the super tidal, semi diurnal, and diurnal, we observe many points that appear to be under energetic outliers with respect to KE in MITgcm, but which are more accurately represented in the HYCOM runs. One possible explanation for this phenomena is that HYCOM is the operational model for the United States Navy, and has undergone a more lengthy process of fine tuning the parameters to better fit observed data.

By presenting and analyzing the high resolutions OGCMs in Chapters II and III, we lay the foundation for further work in quantifying the global reservoirs of APE and KE across the frequency spectrum. This planned future work will include maps of surface KE, which will be of use for informing future satellite missions focused on observing surface velocities, as well as maps of internal KE and APE.

Although Chapters II and III show that in bulk, high resolution OGCMs are beginning to accurately resolve energetic phenomena in the ocean to smaller scales, we have also found that in some frequency regimes, factors such as topographic wave drag and damping will be increasingly important to accurate model solutions. As resolution continues to increase, and more of the IGW continuum begins to be resolved, it is likely that the implementation of damping and more refined dissipation schemes within the models will be a key role in continuing to improve the accuracy of OGCMs in the future. OGCMs lack sufficient resolution and employ hydrostatic approximations, and are unable to resolve the true physical damping mechanisms in the ocean such as turbulence which are fundamentally nonhydrostatic.

Chapter IV is motivated by the need to better understand the effects of turbulent dissipation of KE, and how it is related to physical processes that are resolved

in OGCMs. The estimates of the turbulent KE dissipation rates made in Chapter IV represent unprecedented spatial and temporal coverage, revealing basic insights into the three-dimensional structure of mixing, as well as the temporal modulations caused by the many physical processes interacting with the IGW field. We find that the turbulent KE dissipation rate decays rapidly with horizontal distance from topography, highlighting the importance of interactions of flow with topography for mixing in the ocean. The strong spring-neap cycles seen in the turbulent KE dissipation rate show that the breaking and dissipation of internal tides play a significant role in mixing around the island of Palau. Time-averaged vertical profiles show elevated near-bottom dissipation, as well as enhanced dissipation in the upper water column. The results presented in Chapter IV suggest that turbulent dissipation is strongly influenced by mesoscale activity, inertial and internal gravity waves, and tidal motions. The results presented in Chapter IV represent an extremely unique data set, and a relatively new technique, and as such future work has yet to be done in order to validate the estimates of thermal variance dissipation and turbulent kinetic energy dissipation to more direct measurements. Work is in progress to process several χ-Pods contained on the moorings, which will serve to validate the estimates presented in Chapter IV. Further work will investigate the dissipation of wake eddies through the correlation of near-field vorticity events and their role in enhanced turbulent kinetic energy dissipation.

In this work, we show that high-resolution OGCMs are useful in the study of global reservoirs of APE and KE, and physical processes such as mesoscale eddies, tides, and internal gravity waves. Our analysis helps quantify how improvements in resolution lead to improvements in the representation of these processes within models, particularly at higher frequencies, where smaller length scales are needed to accurately capture the relevant physical processes. Furthermore, we show how implementations of wave drag and dissipation are important to realistically model internal

tides. Finally we explore the turbulent dissipation of KE around topographic features with an approach that provides both a qualitative and quantitative view of processes governing turbulent dissipation. The study of output from high resolution OGCMs can provide invaluable knowledge regarding a wide range of physical processes in the ocean, and can aid in better understanding the implications of ocean mixing on the meridional overturning circulation, poleward heat transport, and ultimately, our global climate.

BIBLIOGRAPHY

BIBLIOGRAPHY

Alford, M., and R. Pinkel (2000), Patterns of turbulent and double-diffusive phenomena: Observations from a rapid-profiling microconductivity probe, *Journal of Physical Oceanography*, *30*(5), 833–854, doi:10.1175/1520-0485(2000)030⟨0833:POTADD⟩2.0.CO;2.

Alford, M. H., J. A. MacKinnon, H. L. Simmons, and J. D. Nash (2016), Near-inertial internal gravity waves in the ocean, *Annual Review of Marine Science*, *8*(1), 95–123, doi:10.1146/annurev-marine-010814-015746, pMID: 26331898.

Ansong, J. K., B. K. Arbic, M. C. Buijsman, J. G. Richman, J. F. Shriver, and A. J. Wallcraft (2015), Indirect evidence for substantial damping of low-mode internal tides in the open ocean, *Journal of Geophysical Research: Oceans*, *120*(9), 6057–6071, doi:10.1002/2015JC010998.

Ansong, J. K., B. K. Arbic, M. H. Alford, M. C. Buijsman, J. F. Shriver, Z. Zhao, J. G. Richman, H. L. Simmons, P. G. Timko, A. J. Wallcraft, and L. Zamudio (2017), Semidiurnal internal tide energy fluxes and their variability in a global ocean model and moored observations, *Journal of Geophysical Research: Oceans*, *122*(3), 1882–1900, doi:10.1002/2016JC012184.

Antonov, J. I., D. Seidov, T. P. Boyer, R. A. Locarnini, A. V. Mishonov, H. E. Garcia, O. K. Baranova, M. M. Zweng, and D. R. Johnson (2010), *World Ocean Atlas 2009, Volume 2: Salinity*, NOAA Atlas NESDIS 68, U.S. Government Printing Office, Washington, D.C.

Arbic, B., M. Alford, J. Ansong, M. Buijsman, R. Ciotti, J. Farrar, R. Hallberg, C. Henze, C. Hill, C. Luecke, D. Menemenlis, E. Metzger, M. Müller, A. Nelson, B. Nelson, H. Ngodock, R. Ponte, J. Richman, A. Savage, R. Scott, J. Shriver, H. Simmons, I. Souopgui, P. Timko, A. Wallcraft, L. Zamudio, and Z. Zhao (2018), *New Frontiers in Operational Oceanography*, chap. 13: A primer on global internal tide and internal gravity wave continuum modeling in HYCOM and MITgcm, pp. 307–392, GODAE OceanView, doi:doi:10.17125/gov2018.ch13.

Arbic, B. K., A. J. Wallcraft, and E. J. Metzger (2010), Concurrent simulation of the eddying general circulation and tides in a global ocean model, *Ocean Modelling*, *32*, 175–187.

Arbic, B. K., R. B. Scott, G. R. Flierl, A. J. Morten, J. G. Richman, and J. F. Shriver (2012a), Nonlinear cascades of surface oceanic geostrophic kinetic

energy in the frequency domain, *J. Phys. Oceanogr.*, *42*(9), 1577–1600, doi: 10.1175/JPO-D-11-0151.1.

Arbic, B. K., J. G. Richman, J. F. S. USA, P. G. Timko, E. J. Metzger, and A. J. Wallcraft (2012b), Global modeling of internal tides within an eddying ocean general circulation model, *Oceanography*, *25*.

Arbic, B. K., M. Müller, J. G. Richman, J. F. Shriver, A. J. Morten, R. B. Scott, G. Sérazin, and T. Penduff (2014), Geostrophic turbulence in the frequency-wavenumber domain: Eddy-driven low-frequency variability, *J. Phys. Oceanogr.*, *44*(8), 2050–2069, doi:10.1175/JPO-D-13-054.1.

Batchelor, G. K. (1959), Small-scale variation of convected quantities like temperature in turbulent fluid, *Journal of Fluid Mechanics*, *5*(1), 113–139, doi: 10.1017/S002211205900009X.

Bell, T. H. (1975), Lee waves in stratified flows with simple harmonic time dependence, *Journal of Fluid Mechanics*, *67*(4), 705–722, doi:10.1017/S0022112075000560.

Buijsman, M., B. Arbic, J. Green, R. Helber, J. Richman, J. Shriver, P. Timko, and A. Wallcraft (2015), Optimizing internal wave drag in a forward barotropic model with semidiurnal tides, *Ocean Modelling*, *85*, 42 – 55, doi:https://doi.org/10.1016/j.ocemod.2014.11.003.

Buijsman, M. C., J. K. Ansong, B. K. Arbic, J. G. Richman, J. F. Shriver, P. G. Timko, A. J. Wallcraft, C. B. Whalen, and Z. Zhao (2016), Impact of parameterized internal wave drag on the semidiurnal energy balance in a global ocean circulation model, *Journal of Physical Oceanography*, *46*(5), 1399–1419, doi: 10.1175/JPO-D-15-0074.1.

Capet, X., J. C. McWilliams, M. J. Molemaker, and A. F. Shchepetkin (2008), Mesoscale to submesoscale transition in the california current system. part iii: Energy balance and flux, *Journal of Physical Oceanography*, *38*(10), 2256–2269, doi:10.1175/2008JPO3810.1.

Cartwright, D. E. (1999), *Tides : a scientific history*, 210 pp., Cambridge University Press Cambridge ; New York.

Chassignet, E. P., and X. Xu (2017), Impact of horizontal resolution (1/12 to 1/50) on gulf stream separation, penetration, and variability, *Journal of Physical Oceanography*, *47*(8), 1999–2021, doi:10.1175/JPO-D-17-0031.1.

Chassignet, E. P., H. E. Hurlburt, E. J. Metzger, O. M. Smedstad, J. A. Cummings, G. R. Halliwell, R. Bleck, R. Baraille, A. J. Wallcraft, C. Lozano, H. L. Tolman, A. Srinivasan, S. Hankin, P. Cornillon, R. Weisberg, A. Barth, R. He, F. Werner, and J. Wilkin (2009), US GODAE: Global ocean prediction with the HYbrid Coordinate Ocean Model (HYCOM), *Oceanography.*, *22(2)*, 64–75, doi: dx.doi.org/10.5670/oceanog.2009.39.

Chelton, D. B., M. G. Schlax, R. M. Samelson, and R. A. de Szoeke (2007), Global observations of large oceanic eddies, *Geophysical Research Letters*, *34*(15), doi:10.1029/2007GL030812, l15606.

Cummings, J. A., and O. M. Smedstad (2013), Variational data assimilation for the global ocean, in *Data Assimilation for Atmospheric, Oceanic and Hydrologic Applications (Vol. II)*, edited by S. K. Park and L. Xu, pp. 303–343, Springer Berlin Heidelberg, doi:10.1007/978-3-642-35088-7_13.

Dantzler, H. K. (1977), Potential energy maxima in the tropical and subtropical north atlantic, *Journal of Physical Oceanography*, *7*(4), 512–519, doi:10.1175/1520-0485(1977)007⟨0512:PEMITT⟩2.0.CO;2.

D'Asaro, E. A. (1984), Wind forced internal waves in the north pacific and sargasso sea, *Journal of Physical Oceanography*, *14*(4), 781–794, doi:10.1175/1520-0485(1984)014⟨0781:WFIWIT⟩2.0.CO;2.

Dee, D. P., S. M. Uppala, A. J. Simmons, P. Berrisford, P. Poli, S. Kobayashi, U. Andrae, M. A. Balmaseda, G. Balsamo, P. Bauer, P. Bechtold, A. C. M. Beljaars, L. van de Berg, J. Bidlot, N. Bormann, C. Delsol, R. Dragani, M. Fuentes, A. J. Geer, L. Haimberger, S. B. Healy, H. Hersbach, E. V. Hólm, L. Isaksen, P. Kållberg, M. Köhler, M. Matricardi, A. P. McNally, B. M. Monge-Sanz, J.-J. Morcrette, B.-K. Park, C. Peubey, P. de Rosnay, C. Tavolato, J.-N. Thépaut, and F. Vitart (2011), The ERA-interim reanalysis: configuration and performance of the data assimilation system, *Quarterly Journal of the Royal Meteorological Society*, *137*(656), 553–597, doi:10.1002/qj.828.

Doherty, K. W., D. E. Frye, S. P. Liberatore, and J. M. Toole (1999), A moored profiling instrument, *Journal of Atmospheric and Oceanic Technology*, *16*, 1816–1829.

Ducet, N. P., Y. L. Traon, and G. Reverdin (2000), Global high-resolution mapping of ocean circulation from topex/poseidon and ers-1 and -2, *Journal of Geophysical Research: Oceans*, *105*(C8), 19,477–19,498, doi:10.1029/2000JC900063.

Egbert, G. D., and S. Y. Erofeeva (2002), Efficient inverse modeling of barotropic ocean tides, *Journal of Atmospheric and Oceanic Technology*, *19*(2), 183–204, doi:10.1175/1520-0426(2002)019⟨0183:EIMOBO⟩2.0.CO;2.

Egbert, G. D., A. F. Bennett, and M. G. G. Foreman (1994), TOPEX/POSEIDON tides estimated using a global inverse model, *Journal of Geophysical Research: Oceans*, *99*(C12), 24,821–24,852, doi:10.1029/94JC01894.

Ferrari, R., and C. Wunsch (2009), Ocean circulation kinetic energy: Reservoirs, sources, and sinks, *Annual Review of Fluid Mechanics*, *41*(1), 253–282, doi:10.1146/annurev.fluid.40.111406.102139.

Flierl, G. R., and J. C. McWilliams (1977), Sampling requirements for measuring moments of eddy variability, *Journal of Marine Research*, *35*, 797–820.

Garrett, C., and E. Kunze (2007), Internal tide generation in the deep ocean, *Annual Review of Fluid Mechanics*, *39*(1), 57–87, doi:10.1146/annurev.fluid.39.050905.110227.

Garrett, C., and W. Munk (1975), Space-time scales of internal waves: A progress report, *Journal of Geophysical Research*, *80*(3), 291–297, doi:10.1029/JC080i003p00291.

Gnanadesikan, A. (1999), A simple predictive model for the structure of the oceanic pycnocline, *Science*, *283*, 2077–2079.

Gregg, M. (1987), Diapycnal mixing in the thermocline: A review, *Journal of Geophysical Research: Oceans*, *92*(C5), 5249–5286, doi:10.1029/JC092iC05p05249.

Hecht, W. M., and H. Hasumi (2008), *Ocean Modeling in an Eddying Regime*, vol. Geophysical Monograph; 177, American Geophysical Union, 2000 Florida Avenue N. W., Washington, D.C.

Hendershott, M. C. (1972), The effects of solid earth deformation on global ocean tides, *Geophysical Journal of the Royal Astronomical Society*, *29*(4), 389–402, doi:10.1111/j.1365-246X.1972.tb06167.x.

Hogan, T. F., M. Liu, J. A. Ridout, M. S. Peng, T. R. Whitcomb, B. C. Ruston, C. A. Reynolds, S. D. Eckermann, J. R. MoskaitisO, N. L. Baker, P. McCormack, J, L. C. Viner, J. G. McLay, M. K. Flatau, L. Xu, C. C, and S. W. Chang (2014), The navy global environmental model, *Oceanography*, *27*(3), 116–125.

Huang, R. X. (1998), Mixing and available potential energy in a Boussinesq ocean, *J. Phys. Oceanog.*, *28*, 669–678.

Jacobs, G. A., C. N. Barron, and R. C. Rhodes (2001), Mesoscale characteristics, *Journal of Geophysical Research: Oceans*, *106*(C9), 19,581–19,595, doi:10.1029/2000JC000669.

Jakobsson, M., R. Macnab, L. Mayer, R. Anderson, M. Edwards, J. Hatzky, H. W. Schenke, and P. Johnson (2008), An improved bathymetric portrayal of the arctic ocean: Implications for ocean modeling and geological, geophysical and oceanographic analyses, *Geophysical Research Letters*, *35*(7), doi:10.1029/2008GL033520, l07602.

Jayne, S. R., and L. C. St. Laurent (2001), Parameterizing tidal dissipation over rough topography, *Geophysical Research Letters*, *28*(5), 811–814, doi:10.1029/2000GL012044.

Kang, D., and O. Fringer (2010), On the calculation of available potential energy in internal wave fields, *J. Phys. Oceanogr.*, *40*, 2539–2545.

Kunze, E. (2017), The internal-wave-driven meridional overturning circulation, *Journal of Physical Oceanography*, *47*(11), 2673–2689, doi:10.1175/JPO-D-16-0142.1.

Kuragano, T., and M. Kamachi (2000), Global statistical space-time scales of oceanic variability estimated from the topex/poseidon altimeter data, *Journal of Geophysical Research: Oceans*, *105*(C1), 955–974, doi:10.1029/1999JC900247.

Large, W., and S. Yeager (2004), *Diurnal to Decadal Global Forcing for Ocean and Sea-ice Models: The Data Sets and Flux Climatologies*, NCAR technical notes, National Center for Atmospheric Research.

Large, W. G., J. C. McWilliams, and S. C. Doney (1994), Oceanic vertical mixing: A review and a model with a nonlocal boundary layer parameterization, *Reviews of Geophysics*, *32*(4), 363–403, doi:10.1029/94RG01872.

Locarnini, R. A., A. V. Mishonov, J. I. Antonov, T. P. Boyer, H. E. Garcia, O. K. Baranova, M. M. Zweng, and D. R. Johnson (2010), *World Ocean Atlas 2009, Volume 1: Temperature*, NOAA Atlas NESDIS 68, U.S. Government Printing Office, Washington, D.C.

Losch, M., D. Menemenlis, J.-M. Campin, P. Heimbach, and C. Hill (2010), On the formulation of sea-ice models. Part 1: Effects of different solver implementations and parameterizations, *Ocean Modelling*, *33*(1), 129 – 144, doi:https://doi.org/10.1016/j.ocemod.2009.12.008.

Lueck, R. G., F. Wolk, and H. Yamazaki (2002), Oceanic velocity microstructure measurements in the 20th century, *Journal of Oceanography*, *58*(1), 153–174, doi:10.1023/A:1015837020019.

Luecke, C. A., B. K. Arbic, S. L. Bassette, J. G. Richman, J. F. Shriver, M. H. Alford, O. M. Smedstad, P. G. Timko, D. S. Trossman, and A. J. Wallcraft (2017), The global mesoscale eddy available potential energy field in models and observations, *Journal of Geophysical Research: Oceans*, *122*(11), 9126–9143, doi:10.1002/2017JC013136.

Lumpkin, R., and M. Pazos (2007), *Lagrangian Analysis and Prediction of Coastal and Ocean Dynamics:*, Cambridge University Press, Cambridge, doi:10.1017/CBO9780511535901.

Maltrud, M. E., and J. L. McClean (2005), An eddy resolving global 1/10 ocean simulation, *Ocean Modelling*, *8*(1–2), 31 – 54, doi:https://doi.org/10.1016/j.ocemod.2003.12.001.

Marshall, J., A. Adcroft, C. Hill, L. Perelman, and C. Heisey (1997), A finite-volume, incompressible navier stokes model for studies of the ocean on parallel computers, *Journal of Geophysical Research: Oceans*, *102*(C3), 5753–5766, doi:10.1029/96JC02775.

McClean, J. L., D. C. Bader, F. O. Bryan, M. E. Maltrud, J. M. Dennis, A. A. Mirin, P. W. Jones, Y. Y. Kim, D. P. Ivanova, M. Vertenstein, J. S. Boyle, R. L. Jacob, N. Norton, A. Craig, and P. H. Worley (2011), A prototype two-decade fully-coupled fine-resolution ccsm simulation, *Ocean Modelling*, *39*(1), 10 – 30, doi: https://doi.org/10.1016/j.ocemod.2011.02.011, modelling and Understanding the Ocean Mesoscale and Submesoscale.

McDougall, T. J., and P. M. Barker (2011), *Getting Started with TEOS-10 and the Gibbs Seawater (GSW) Oceanographic Toolbox*, SCOR/IAPSO WG127.

Menemenlis, D., J.-M. Campin, P. Heimbach, C. Hill, T. Lee, A. Nguyen, M. Schodlok, and H. Zhang (2008), Ecco2: High resolution global ocean and sea ice data synthesis, *Mercator Ocean Quarterly Newsletter*, *31*.

Metzger, E. J., O. M. Smedstad, P. G. Thoppil, H. E. Hurlburt, J. A. Cummings, A. J. Wallcraft, L. Zamudio, D. S. Franklin, P. G. Posey, M. W. Phelps, P. J. Hogan, F. L. Bub, and C. J. DeHaan. (2014), US Navy Operational Global Ocean and Arctic Ice Prediction Systems., *Oceanography*, *27*(3), 32–43, doi:http://dx.doi.org/10.5670/oceanog.2014.66.

Moum, J. N., and J. D. Nash (2009), Mixing measurements on an equatorial ocean mooring, *Journal of Atmospheric and Oceanic Technology*, *26*(2), 317–336, doi: 10.1175/2008JTECHO617.1.

Moum, J. N., A. Perlin, J. D. Nash, and M. J. McPhaden (2013), Seasonal sea surface cooling in the equatorial pacific cold tongue controlled by ocean mixing, *Nature*, *500*, 64 EP –.

Müller, M., B. K. Arbic, J. G. Richman, J. F. Shriver, E. L. Kunze, R. B. Scott, A. J. Wallcraft, and L. Zamudio (2015), Toward an internal gravity wave spectrum in global ocean models, *Geophysical Research Letters*, *42*(9), 3474–3481, doi:10.1002/2015GL063365, 2015GL063365.

Munk, W., and C. Wunsch (1998), Abyssal recipes ii: Energetics of tidal and wind mixing, *Deep-Sea Research I*, *45*.

Murphy, A. H. (1988), Skill scores based on the mean square error and their relationships to the correlation coefficient, *Monthly Weather Review*, *116*(12), 2417–2424, doi:10.1175/1520-0493(1988)116⟨2417:SSBOTM⟩2.0.CO;2.

Musgrave, R. C., J. A. MacKinnon, R. Pinkel, A. F. Waterhouse, and J. Nash (2016), Tidally driven processes leading to near-field turbulence in a channel at the crest of the mendocino escarpment, *Journal of Physical Oceanography*, *46*(4), 1137–1155, doi:10.1175/JPO-D-15-0021.1.

Ngodock, H. E., I. Souopgui, A. J. Wallcraft, J. G. Richman, J. F. Shriver, and B. K. Arbic (2016), On improving the accuracy of the m_2 barotropic tides embedded in a high-resolution global ocean circulation model, *Ocean Modelling*, *97*, 16 – 26, doi:https://doi.org/10.1016/j.ocemod.2015.10.011.

Osborn, T. R. (1980), Estimates of the local rate of vertical diffusion from dissipation measurements, *Journal of Physical Oceanography*, *10*(1), 83–89, doi: 10.1175/1520-0485(1980)010⟨0083:EOTLRO⟩2.0.CO;2.

Osborn, T. R., and C. S. Cox (1972), Oceanic fine structure, *Geophysical Fluid Dynamics*, *3*(1), 321–345, doi:10.1080/03091927208236085.

Penduff, T., B. Barnier, J.-M. Molines, and G. Madec (2006), On the use of current meter data to assess the realism of ocean model simulations, *Ocean Modelling*, *11*, 399–416.

Ponte, R. M., A. H. Chaudhuri, and S. V. Vinogradov (2015), Long-period tides in an atmospherically driven, stratified ocean, *Journal of Physical Oceanography*, *45*(7), 1917–1928, doi:10.1175/JPO-D-15-0006.1.

Qiu, B., S. Chen, P. Klein, J. Wang, H. Torres, L.-L. Fu, and D. Menemenlis (2018), Seasonality in transition scale from balanced to unbalanced motions in the world ocean, *Journal of Physical Oceanography*, *48*(3), 591–605, doi: 10.1175/JPO-D-17-0169.1.

Ray, R. D. (1999), *A Global Ocean Tide model from TOPEX/POSEIDON altimetry: GOT99.2*, 1 v. pp., National Aeronautics and Space Administration, Goddard Space Flight Center ; National Technical Information Service, distributor Greenbelt, M, Springfield, Va.

Richman, J. G., C. Wunsch, and N. G. Hogg (1977), Space and time scales of mesoscale motion in the western north atlantic, *Reviews of Geophysics*, *15*(4), 385–420, doi:10.1029/RG015i004p00385.

Rocha, C. B., T. K. Chereskin, S. T. Gille, and D. Menemenlis (2016a), Mesoscale to submesoscale wavenumber spectra in Drake Passage, *Journal of Physical Oceanography*, *46*(2), 601–620, doi:10.1175/JPO-D-15-0087.1.

Rocha, C. B., S. T. Gille, T. K. Chereskin, and D. Menemenlis (2016b), Seasonality of submesoscale dynamics in the kuroshio extension, *Geophysical Research Letters*, *43*(21), 11,304–11,311, doi:10.1002/2016GL071349.

Roemmich, D., and B. W. Owens (2000), The argo project: Global ocean observations for understanding and prediction of climate variability, *Oceanography*, *13*.

Roullet, G., X. Capet, and G. Maze (2014), Global interior eddy available potential energy diagnosed from argo floats, *Geophysical Research Letters*, *41*(5), 1651–1656, doi:10.1002/2013GL059004.

Rudnick, D. L., and R. Ferrari (1999), Compensation of horizontal temperature and salinity gradients in the ocean mixed layer, *Science*, *283*(5401), 526–529, doi:10.1126/science.283.5401.526.

Saenz, J. A., A. M. Hogg, G. O. Hughes, and R. W. Griffiths (2012), Mechanical power input from buoyancy and wind to the circulation in an ocean model, *Geophysical Research Letters*, *39*(13), doi:10.1029/2012GL052035, l13605.

Saha, S., S. Moorthi, H.-L. Pan, X. Wu, J. Wang, S. Nadiga, P. Tripp, R. Kistler, J. Woollen, D. Behringer, H. Liu, D. Stokes, R. Grumbine, G. Gayno, J. Wang, Y.-T. Hou, H.-Y. Chuang, H.-M. H. Juang, J. Sela, M. Iredell, R. Treadon, D. Kleist, P. Van Delst, D. Keyser, J. Derber, M. Ek, J. Meng, H. Wei, R. Yang, S. Lord, H. Van Den Dool, A. Kumar, W. Wang, C. Long, M. Chelliah, Y. Xue, B. Huang, J.-K. Schemm, W. Ebisuzaki, R. Lin, P. Xie, M. Chen, S. Zhou, W. Higgins, C.-Z. Zou, Q. Liu, Y. Chen, Y. Han, L. Cucurull, R. W. Reynolds, G. Rutledge, and M. Goldberg (2010), The NCEP climate forecast system reanalysis, *Bull. Amer. Meteor. Soc.*, *91*(8), 1015–1057, doi:10.1175/2010BAMS3001.1.

Saha, S., S. Moorthi, X. Wu, J. Wang, S. Nadiga, P. Tripp, D. Behringer, Y.-T. Hou, H.-y. Chuang, M. Iredell, M. Ek, J. Meng, R. Yang, M. P. Mendez, H. van den Dool, Q. Zhang, W. Wang, M. Chen, and E. Becker (2013), The ncep climate forecast system version 2, *J. Climate*, *27*(6), 2185–2208, doi:10.1175/JCLI-D-12-00823.1.

Savage, A. C., B. K. Arbic, J. G. Richman, J. F. Shriver, M. H. Alford, M. C. Buijsman, J. Thomas Farrar, H. Sharma, G. Voet, A. J. Wallcraft, and L. Zamudio (2017a), Frequency content of sea surface height variability from internal gravity waves to mesoscale eddies, *Journal of Geophysical Research: Oceans*, *122*(3), 2519–2538, doi:10.1002/2016JC012331.

Savage, A. C., B. K. Arbic, M. H. Alford, J. K. Ansong, J. T. Farrar, D. Menemenlis, A. K. O'Rourke, J. G. Richman, J. F. Shriver, G. Voet, A. J. Wallcraft, and L. Zamudio (2017b), Spectral decomposition of internal gravity wave sea surface height in global models, *Journal of Geophysical Research: Oceans*, *122*(10), 7803–7821, doi:10.1002/2017JC013009.

Schmitz, W. J. (1988), Exploration of the eddy field in the midlatitude North Pacific, *J. Phys. Oceanogr.*, *18*(3), 459–468, doi:10.1175/1520-0485.

Scott, R. B., B. K. Arbic, E. P. Chassignet, A. C. Coward, M. Maltrud, W. J. Merryfield, A. Srinivasan, and A. Varghese (2010), Total kinetic energy in four global eddying ocean circulation models and over 5000 current meter records, *Ocean Modelling*, *32*, 157–169.

Shriver, J. F., B. K. Arbic, J. G. Richman, R. D. Ray, E. J. Metzger, A. J. Wallcraft, and P. G. Timko (2012), An evaluation of the barotropic and internal tides in a high-resolution global ocean circulation model, *J. Geophys. Res.*, *117*(C10024), doi:10.1029/2012JC008170.

Silverthorne, K. E., and J. M. Toole (2009), Seasonal kinetic energy variability of near-inertial motions, *Journal of Physical Oceanography*, *39*(4), 1035–1049, doi:10.1175/2008JPO3920.1.

Simmons, H. L., and M. H. Alford (2012), Simulating the long-range swell of internal waves generated by ocean storms, *Oceanography*, *25*.

Skiba, A. W., L. Zeng, B. K. Arbic, M. Müller, and W. J. Godwin (2013), On the resonance and shelf/open-ocean coupling of the global diurnal tides, *Journal of Physical Oceanography*, *43*(7), 1301–1324, doi:10.1175/JPO-D-12-054.1.

Smith, W. H. F., and D. T. Sandwell (1997), Global sea floor topography from satellite altimetry and ship depth soundings, *Science*, *277*(5334), 1956–1962, doi:10.1126/science.277.5334.1956.

Stammer, D., R. D. Ray, O. B. Andersen, B. K. Arbic, W. Bosch, L. Carrére, Y. Cheng, D. S. Chinn, B. D. Dushaw, G. D. Egbert, S. Y. Erofeeva, H. S. Fok, J. A. M. Green, S. Griffiths, M. A. King, V. Lapin, F. G. Lemoine, S. B. Luthcke, F. Lyard, J. Morison, M. Müller, L. Padman, J. G. Richman, J. F. Shriver, C. K. Shum, E. Taguchi, and Y. Yi (2014), Accuracy assessment of global barotropic ocean tide models, *Reviews of Geophysics*, *52*(3), 243–282, doi:10.1002/2014RG000450.

Su, Z., J. Wang, P. Klein, A. F. Thompson, and D. Menemenlis (2018), Ocean submesoscales as a key component of the global heat budget, *Nature Communications*, *9*(1), 775, doi:10.1038/s41467-018-02983-w.

Tailleux, R. (2013), Available potential energy and exergy in stratified fluids, *Annual Review of Fluid Mechanics*, *45*(1), 35–58, doi:10.1146/annurev-fluid-011212-140620.

Thoppil, P. G., J. G. Richman, and P. J. Hogan (2011), Energetics of a global ocean circulation model compared to observations, *Geophysical Research Letters*, *38*(15), doi:10.1029/2011GL048347.

Timko, P. G., B. K. Arbic, J. G. Richman, R. B. Scott, E. J. Metzger, and A. J. Wallcraft (2012), Skill tests of three-dimensional tidal currents in a global ocean model: A look at the North Atlantic, *J. Geophys. Res: Oceans*, *117*(C8), doi:10.1029/2011JC007617.

Timko, P. G., B. K. Arbic, J. G. Richman, R. B. Scott, E. J. Metzger, and A. J. Wallcraft (2013), Skill testing a three-dimensional global tide model to historical current meter records, *J. Geophys. Res: Oceans*, *118*(12), 6914–6933, doi:10.1002/2013JC009071.

Trossman, D. S., B. K. Arbic, J. G. Richman, S. T. Garner, S. R. Jayne, and A. J. Wallcraft (2016), Impact of topographic internal lee wave drag on an eddying global ocean model, *Ocean Modelling*, *97*, 109 – 128, doi:https://doi.org/10.1016/j.ocemod.2015.10.013.

Weis, P., M. Thomas, and J. Sündermann (2008), Broad frequency tidal dynamics simulated by a high-resolution global ocean tide model forced by ephemerides, *Journal of Geophysical Research: Oceans*, *113*(C10), doi:10.1029/2007JC004556.

Winters, K. B., P. N. Lombard, J. J. Riley, and E. A. D'Asaro (1995), Available potential energy and mixing in density-stratified fluids, *J. Fluid Mech.*, *94*, 3187–3200.

Wright, C. J., R. B. Scott, P. Ailliot, and D. Furnival (2014), Lee wave generation rates in the deep ocean, *Geophysical Research Letters*, *41*(7), 2434–2440, doi:10.1002/2013GL059087.

Wunsch, C. (1999), A summary of north atlantic baroclinic variability, *Journal of Physical Oceanography*, *29*(12), 3161–3166, doi:10.1175/1520-0485(1999)029⟨3161:ASONAB⟩2.0.CO;2.

Zhang, Y., and J. N. Moum (2010), Inertial-convective subrange estimates of thermal variance dissipation rate from moored temperature measurements, *Journal of Atmospheric and Oceanic Technology*, *27*(11), 1950–1959, doi:10.1175/2010JTECHO746.1.